Detection of Volatile Organic Compounds in Plant Stress: A Study on Geraniol

Idil Cazimoglu

New College

University of Oxford

A thesis submitted for the degree of

Master of Science by Research

2016

I wish to dedicate this work and others to
world peace
for peace brings us knowledge
and knowledge brings us peace.

Acknowledgements

Firstly, I would like to thank my supervisors, Prof Claire Vallance and Prof Lee Sweetlove, for their time and guidance throughout this work. The knowledge they have shared generously with me is invaluable for this thesis and beyond.

My fellow lab member Dean James has been the best mentor I could ask for. He has always been there to help, give advice, and exchange insults. In the past two years, he has not only taught me a lot, but also made my working days enjoyable.

At the Department of Plant Sciences, Pedro Bota, Lottie Chapman and Aparajitha Srinivasan helped me (a physical chemist in training) adjust to the world of plants (live organisms with complex needs). Pedro trained me in GC-MS, Lottie showed me how to grow plants, and Aparajitha saved my plants' lives several times.

Within the Department of Chemistry, I would like to acknowledge:

- Dr. James Wickens for his help with the headspace GC-MS measurements. He eagerly tried these experiments over and over again with me, and provided prompt advice and shared his GC-MS expertise whenever I needed it.
- Dr. Grant Ritchie for allowing me to use the OF-CEAS setup, and Dr. Katherine Manfred and Katharine Hunter for their help with the experiments.
- Prof. Kylie Vincent for allowing me to use the FTIR spectrometer, and Dr. Philip Ash for his help with the experiments.
- Choon Boon Cheong for letting me borrow his fumehood and various equipment for multiple geraniol-drying attempts.
- Electronics and mechanical workshops for manufacturing numerous equipment used in this project with great care and speed.

I would like to thank all of the Vallance lab members who lit up the windowless CRL basement with their presence, in particular, Dr. Jason Lee for meaningful advice, Eleanor Morris for being my tea break companion, and Hansjochen Köckert for cheering me up when things didn't work at various stages of this project.

Special thanks to Simon Victor Jupp for graciously using his architectural skills to assist me with the schematic diagrams in this thesis. I hope he finds some use for the physical chemistry terms he has learned in the process.

In addition, I would like to thank my examiners Prof Lucy Carpenter and Prof James McCullagh for their helpful comments and suggestions for improvement.

Finally, I owe my deepest gratitude to my family for all of the sacrifices they have made to give me the opportunities I have. Their continual support and unwavering belief in me have made this thesis possible. Teşekkür ederim.

Abstract

Detection of plant volatile organic compounds as indicators of plant stress can improve crop yield and agricultural sustainability by enabling early-stage treatment of crop stress and by reducing the overall use of agricultural resources. In this work, the feasibility of detecting gaseous geraniol, a plant volatile, using cavity enhanced absorption spectroscopy (CEAS), a sensitive and non-destructive analytical technique, was assessed. For geraniol gas, a limit of detection of 147 ppb was achieved, and a limit of 25.5 ppb was calculated to be attainable with modifications to the experimental setup. For geraniol in solution, gas chromatography–mass spectrometry (GC-MS) measurements were performed, and a detection limit of 2.6 μM was established. Rose (*Rosa* 'English Princess') petals, pelargonium (*Pelargonium* 'Attar of Roses') leaves, and genetically modified tobacco (*Nicotiana benthamiana*) leaves were analysed for their geraniol content. 8.2 μM of geraniol was detected in liquid extracts of 0.5 g of pelargonium leaf and, employing two different assumptions, upper limits of 670 and 1930 ppb were estimated for the concentration of geraniol expected in the headspace of this tissue. For 0.5 g of tobacco leaf, an emission rate of 117 ppb h^{-1} was calculated for a 20 mL headspace using data from previous studies. It was concluded that CEAS is a promising technique for sensitive detection of plant volatiles. In addition to geraniol measurements, chemical composition of the rose petals and the pelargonium leaves were analysed by headspace and liquid extract GC-MS measurements. Detected compounds were compared with compounds reported for related species and cultivars. Many of these compounds play key roles in stress signalling in various plants, and their detection could be instrumental in monitoring the health of these plants.

Contents

List of Figures

List of Tables

List of Abbreviations

A/D	Analog-to-Digital
BS	Beam Splitter
CEAS	Cavity Enhanced Absorption Spectroscopy
CEF	Cavity Enhancement Factor
DC	Direct Current
DNA	Deoxyribonucleic acid
EI	Electron Ionisation
FCM	Flow Cytometry
FISH	Fluorescence *in-situ* Hybridization
FSR	Free Spectral Range
FTIR	Fourier Transform Infrared
GC	Gas Chromatography
GC-MS	Gas Chromatography–Mass Spectrometry
GLV	Green Leaf Volatile
GM	Genetically Modified
GTO	Gaussian Type Orbital
HF	Hartree–Fock
ICL	Interband Cascade Laser
ICOS	Integrated Cavity Output Spectroscopy
IF	Immunofluorescence
IPCC	Intergovernmental Panel on Climate Change
IR	Infrared
$K_{\mathbf{ow}}$	Octanol/water partition coefficient
m/z	Mass-to-charge ratio
min	minute(s)
MCP	Microchannel Plate
MS	Mass Spectrometry
MSD	Mass Selective Detector / Mass Spectrometry Detector

NIST	National Institute of Standards
OAPM	Off-Axis Parabolic Mirror
OF-CEAS	Optical Feedback Cavity Enhanced Absorption Spectroscopy
PEG	Polyethyleneglycol
PGPB	Plant Growth Promoting Bacteria
PMT	Photomultiplier Tube
PNNL	Pacific Northwest National Laboratory
ppm	parts per million (mole fraction)
ppb	parts per billion (mole fraction)
ppbv	parts per billion by volume
PTR-MS	Proton Transfer Reaction Mass Spectrometry
PVD	Photovoltaic Detector
PZT	Piezoelectric Transducer
Q-TOF	Quadrupole Time-of-Flight
RF	Radio Frequency
RMSD	Root Mean Square Deviation
ROHF	Restricted Open-shell Hartree–Fock
SCF	Self Consistent Field
SPME	Solid Phase Microextraction
STO	Slater Type Orbital
TOF	Time-of-Flight
UAV	Unmanned Aerial Vehicle
UHF	Unrestricted Hartree-Fock
VOC	Volatile Organic Compound
WT	Wild-Type

1

Introduction

Contents

Cavity Enhanced Absorption Spectroscopy has proven a sensitive analytical technique for the detection of atmospheric gases, but has not yet been applied to plant volatile organic compounds. The plant kingdom is estimated to produce at least 1,060,000 chemical compounds [1]. Over 100,000 of these compounds have been identified [2], [3] and over 1700 of the identified compounds are volatile [4]. Volatile organic compounds (VOCs) can be emitted from roots, leaves, flowers and fruits [5], [6].

Detection of VOCs released by plants is important for several reasons. VOCs react with nitrogen oxides in the presence of sunlight to produce photochemical smog at ground level [7]. Monitoring of atmospheric VOC levels can provide insight into these photochemical reactions. In addition, many VOCs serve as biological stimuli. Geraniol, the molecule of focus in this study, has biological functions in mediating interactions between plants and other organisms. For example, it is an effective repellent against the *Anopheles gambiae* mosquito [8], a Malaria vector, and the *Aedes aegypti* mosquito [9], a Zika vector. In contrast, it is an attractant for honey bees. It was identified as the active component in the Nassanoff pheromone secreted by honey bees to attract each other to the hive entrance and to indicate flowers with an abundant food supply [10]. Detection of VOCs such as geraniol may therefore be useful as part of a strategy for controlling disease or for monitoring pollinator activity. VOC detection can also provide a means of monitoring plant health, since many VOCs are released by plants as part of their defence mechanisms or in response to stress. Focusing on geraniol, this thesis explores a number of possible approaches to the detection of VOCs as a sign of plant stress in agriculture.

1.1 Agricultural Importance of Plant Stress Detection

Defining food security as "a situation that exists when all people, at all times, have physical, social and economic access to sufficient, safe and nutritious food that meets their dietary needs and food preferences for an active and healthy life" [11], the Food and Agriculture Organization of the United Nations projects that ensuring food security for the estimated global population of 9.1 billion people by 2050 would require a 70% rise in overall food production [12]. On the other hand, climate change is projected to negatively affect food security [13]. Significant declines in global yields for maize and wheat, two of the largest commodity crops, have already been linked to rising temperatures [14]. Higher temperatures will also expand the range and activity period of many agricultural pests [13], increasing the prevalence of plant diseases. In addition, the frequency and magnitude of extreme events such as heat waves, floods, and droughts are expected to continue increasing [15], further reducing crop yields.

Expansion of agricultural lands to meet the increasing demand for food will be challenging in countries that have reached the limits of suitable available land [12], and presents threats to biodiversity and ecosystem services [16]. Excessive use of fertilisers to boost crop yields poses a threat to human health as well as the environment. Even though natural levels of phosphorus in soil and addition of manure and human excrement were historically sufficient for crop production, increased food demand since the 19th century has led to mining of the richest deposits of phosphate rock in order to secure phosphorus for fertilisers [17]. Remaining global phosphorus reserves are estimated to last for about 80 years at the current rate of extraction [18]. The quality of the remaining reserves is also an increasing concern, as they are contaminated with heavy metals [19]. In addition, even small leakages of phosphorus from agricultural lands into waters can cause disproportionately high levels of eutrophication [17]. Extensive application of pesticides is now known to pose a hazard to humans as well as non-target plants and animals. For example, pesticides can disrupt the growth and activity of soil microorganisms that transform atmospheric nitrogen into nitrates that plants can absorb. They can be toxic to many animals including fish and birds [20]. Acute pesticide poisoning is a serious health problem in developing countries. Estimates in the 1990s predicted over 25 million cases of acute pesticide poisoning and 200,000 deaths annually [21]. Today, these figures may be much higher [22].

Another pressing global issue is water scarcity. Today, nearly a fifth of the world's population lives in areas of physical water scarcity [23], and 500 million people are approaching this situation [24]. Globally, agriculture is responsible for 69% of freshwater withdrawals [25]. The most optimistic estimates suggest that global agricultural water consumption will increase by 19% by 2050, and this increase could be much greater unless existing agricultural production efficiency and crop yields improve significantly [26].

Described above is only a small selection of the existing and upcoming agricultural challenges. Detection of crop stress can address these challenges in two ways. Firstly, monitoring variation of crop conditions within a field allows targeted use of agricultural resources such as fertilisers, pesticides and water on the areas that are actually in need of these resources. As a result, smaller volumes of these limited or hazardous substances are used, improving agricultural sustainability and reducing health and environmental hazards. Secondly, the detection of stressful conditions at an early stage enables more efficient treatment of plants, boosting crop yields. Therefore, monitoring of crop health can contribute to solutions to both food insecurity and environmental challenges.

1.2 Volatile Organic Compounds

A volatile organic compound (VOC) is an organic compound with a high vapour pressure at standard temperature and pressure. A high vapour pressure is a result of a large number of molecules transitioning from the liquid phase into the gas phase, which in turn is a result of a low boiling point. Under European Union regulations, a VOC is "any organic compound having an initial boiling point less than or equal to 250 °C measured at a standard pressure of 101.3 kPa" [27]. This translates into a wide range of vapour pressures for VOCs, covering several orders of magnitude. For example, while methanethiol has a vapour pressure of 1.51×10^3 mm Hg, bombykol has a vapour pressure of 5.69×10^{-6} mm Hg. Both of these compounds are classified as VOCs [28].

For a biogenic VOC, polarity is a highly important property, as it determines not only its distribution in the environment but also the ease of its evaporation from the organism producing it into the atmosphere. For example, a hydrophobic substance in an aqueous environment evaporates more easily, but is more likely to adsorb to organic surfaces such as soil, rather than mixing into the atmosphere. For this reason, a biogenic VOC is also characterised by its hydrophobicity/hydrophilicity, usually expressed as $\log K_{\text{ow}}$, where K_{ow} represents the octanol/water partition coefficient, the ratio of the substance's concentrations in the octanol and aqueous phases in an octanol/water system at equilibrium where octanol is saturated with water and water is saturated with octanol. Similar to the case for vapour pressures, VOCs span a wide range of K_{ow} values. For example, the $\log K_{\text{ow}}$ value of camphorene is 9.42, whereas that of methyl vinyl ketone is 0.41 [28].

1. Introduction

A significant proportion of VOCs in the atmosphere is released by plants [29]. Leaves, roots and flowers of a diverse range of plants emit VOCs constitutively, i.e. the emissions are not dependent on induction by external stress triggers [30], [31]. However, stress factors can change the levels of these VOCs in plants, or induce *de novo* synthesis of specific VOCs [32], [33], [34]. The VOC composition in the atmosphere around a plant may therefore be diagnostic of its stress state. The most abundant plant VOCs are methanol, ethylene [35], isoprene [5], [36], and 'green leaf volatiles' (GLVs), a group of six-carbon alcohols, aldehydes, ketones and esters often released after tissue damage [35].

Release of VOCs helps plants cope with stress both by acting as warning signals to healthy plants and by alleviating stress through various mechanisms. VOCs provide a means of signalling among different parts of a plant as well as among different plants. For instance, VOCs emitted from herbivore-damaged lima bean leaves cause the production in the undamaged leaves of the plant of chemicals that attract predators [37]. VOCs from lima bean plants infested by herbivores also result in the activation of a defence mechanism in neighbouring intact plants [38]. Plant–plant interactions are not limited to plants of the same species. Tobacco plants growing near damaged sagebrush plants show lower levels of damage by herbivores [39].

Emission of VOCs can alleviate the effects of abiotic stress factors, such as light intensity, temperature, moisture, physical damage, nutrient deficiency, salinity, drought and ozone exposure [40], in several different ways. Released terpenes can alleviate oxidative stress by reacting with O_3, OH and NO_3 radicals [41]. Upon ozone exposure, tobacco (*Nicotiana tabacum* cv. Bel W3) [42], [43] and Scots pine (*Pinus sylvestris* L.) [43] plants show elevated emissions of certain volatiles. VOC emissions can also increase the tolerance of plants to heat and light stresses [44], [45], [46], possibly by stabilising cellular membranes [45], [46], [47], [48]. They could also play a role in the attraction of plant growth promoting bacteria (PGPB) which produce hormones and enzymes that enhance root growth [49]. Larger root mass and length increase water uptake, alleviating drought stress [50], [51]. Total monoterpene emissions in Holm oak (*Quercus ilex* L.) increase with increasing light intensity [52] or decreasing water availability [53]. Changes in temperature and light intensity influence VOC emission rates in sunflower (*Helianthus annuus* L. cv. giganteus) [54], and in *Lilium* 'Siberia'. Temperature, humidity and water availability influence the levels of numerous VOCs in apple trees (*Malus domestica* Borkh.) [55].

VOCs also form an important part of plant defence against biotic stress factors, such as bacteria, viruses, fungi, invertebrates, and other plants [56]. Many VOCs released from plants repel herbivores [57], [58]. Often, emission of these VOCs are induced by the presence of the herbivore. For example, methyl salycilate, induced by aphid infestation, serves as a direct repellent against aphids [59]. Herbivore-induced VOCs can also act as an attractant for herbivore predators or parasitoid wasps. Lima bean plants (*Phaseolus lunatus*) infested with the spider mite (*Tetranychus urticae*) synthesise linalool, which healthy plants do not produce. This compound attracts females of *Phytoseiulus persimilis* and *Amblyseius potentillae*, which then prey on the spider mite [60]. Tobacco, cotton and maize plants each produce a distinct volatile mixture due to damage by the herbivore *Heliothis virescens*, and attract the specialist parasitic wasp for this herbivore, *Cardiochiles nigriceps* [61]. Plants do not have to be under heavy attack by mature herbivores in order to release specialised volatile blends. Oviposition by herbivores results in VOC emissions that attract egg parasitoids and predators [62].

VOCs reported in literature as having a role in plant stress response are in no way limited to what we have described above, and many VOCs and their roles are yet to be discovered. Whether they are emitted as signalling molecules or as biotic or abiotic stress alleviators, VOCs can be exploited in the monitoring of plant health status. In Chapter 4, we will discuss the role of several more plant defence compounds, volatile and non-volatile, within the context of the molecules we detected in various plant tissues by gas chromatography–mass spectrometry.

1.2.1 Geraniol

(2E)-3,7-Dimethyl-2,6-octadien-1-ol, more commonly known as geraniol, is a colourless liquid with a floral smell, and is frequently used in fragrance and flavour

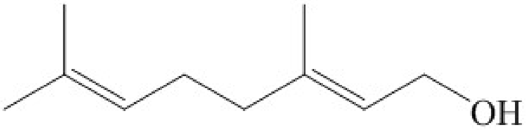

Figure 1.1: Two dimensional structure of geraniol.

substances. It is found in large quantities in palmarosa, geranium and rose oils [63]. A two-dimensional representation of the structure of geraniol, an acyclic monoterpene alcohol with the formula $C_{10}H_{18}O$, can be seen in Figure 1.1.

Geraniol was chosen as our test molecule for cavity enhanced absorption spectroscopy experiments for four reasons: its physical properties, natural role in plant defence, low abundance in plants, and the availability of genetically modified (GM) tobacco plants that have the potential to produce modest amounts of geraniol. Firstly, geraniol has an estimated vapour pressure of 3.0×10^{-2} mm Hg and log K_{ow} of 3.47 at 25 °C [64]. As a VOC with a middle-of-the-range vapour pressure and log K_{ow} value, geraniol serves as a suitable candidate for the study of VOCs. Secondly, naturally occuring geraniol has been shown to regulate the expression of defence-related genes in rough lemon (*Citrus jambhiri* Lush) [65] and chamomile plants (*Matricaria chamomilla*) [66], so changes in geraniol levels may be an indication of stress in some plants. Thirdly, unlike methanol, ethylene, isoprene or GLVs, geraniol is not an abundant VOC in the majority of plants. When monitoring plant health, it is possible that some of the less abundant VOCs are more diagnostic than the most common ones. Finally, tobacco (*Nicotiana benthamiana*) plants have been genetically modified to produce geraniol, which the wild-type (WT) plants do not produce [67], providing an excellent test system for geraniol detection. In principle, further genetic modification could be performed to tie the production of geraniol to specific stress triggers, enabling the tobacco plants to be used as 'sentinel' plants that provide information on the physiological status of the surrounding plants.

1.3 Current Methods for Plant Stress Detection

1.3.1 Molecular Techniques

A number of molecular techniques exist for the detection of plant stress, particularly disease. The most commonly used of these techniques are based on the enzyme-linked immunosorbent assay (ELISA) and the polymerase chain reaction (PCR). ELISA relies on binding of the target compound by a specific antibody, followed by a colorimetric detection [68]. PCR is based on the amplification and detection of specific deoxyribose nucleic acid (DNA) sequences of the pathogen [69], and the copied DNA products are detected most commonly by agarose gel electrophoresis, which separates them based on their size and charge [70]. Other methods include Fluorescence *in-situ* Hybridisation (FISH), Immunofluorescence (IF), and Flow Cytometry (FCM).

Even though molecular methods can sensitively detect plant stress, they are time-consuming, labour intensive, destructive, and they require consumables such as PCR primers unique to the pathogens [71]. Therefore, the applicability of molecular methods for field-based analyses is limited.

1.3.2 Imaging Techniques

Imaging techniques employ optical sensors, and provide non-destructive, rapid and robust means of monitoring plant health in a field setting. The most highly evolved of these techniques are thermography, fluorescence imaging, and spectral reflectance imaging [72].

1.3.2.1 Thermography

Thermography detects the infrared radiation from plant leaf surfaces and canopies, and images the variation of temperature. Infection by pathogens affects water uptake and transport in plants, decreasing the rate of transpiration [73]. Similarly, plants lacking sufficient water supplies close their stomata and reduce transpiration [74]. Lower rates of transpiration, the cooling mechanism of plants, lead to increases in leaf temperature which can be detected by thermography.

While thermography allows for remote and non-destructive sensing of the existence of certain diseases in plants, it cannot identify the disease. Furthermore, diseases with no or little influence on the rate of transpiration cannot be detected [73]. This technique is also prone to errors resulting from variations in environmental conditions, such as the inevitable inclusion of soil, sky, and non-transpiring tissues such as branches in the image. Variation in leaf angles, sunlit and shaded areas, and the distance between the camera and imaged plants can also reduce the quality of the data [75].

1.3.2.2 Fluorescence Imaging

In plants, stress may lead to the synthesis, accumulation or degradation of certain pigments or other molecules [76]. For example, nitrogen deficiency can reduce the amount of chlorophyll in plant tissues [77]. Fungal mycelium can shield the leaf mesophyll and reduce its ability to absorb fluorescence-exciting radiation [78]. These changes influence the fluorescence signature of the tissues. In fluorescence imaging, the crop area is illuminated by a visible or ultraviolet light source [73] and fluorescence signals are used to determine stress levels.

Fluorescence signals are low in intensity and can be concealed by background ambient light. Differential approaches, such as the acquisition of a background image with the excitation source off, are necessary for each fluorescence image [73]. Homogeneous illumination of plant tissue is essential for reliable detection of fluorescence, which calls for a dedicated light source [79]. The excitation light source has high power consumption, particularly for large measurement areas. Fluorescence imaging involves especially complex equipment for operation in daylight. Detection of small differences in fluorescence calls for high detector precision, increasing the cost of equipment [73]. For these reasons, field-based application of fluorescence imaging is limited. In addition, two of the most abundant molecules in the leaf, chlorophyll and lignin, are strongly fluorescent [80], and can mask signals from other fluorescent molecules, which is problematic if levels of these other molecules are being monitored.

1.3.2.3 Spectral Reflectance Imaging

As well as promoting synthesis, accumulation or degradation of certain pigments or other molecules, plant stress can cause morphological changes in leaves, such as curling, wilting or chlorosis [74]. These transformations can alter the reflection of light from plant leaves and canopies [72]. Spectral reflectance imaging records reflectance from plant tissues within specific wavelength bands across a wide range of the electromagnetic spectrum for each pixel in the image. Spectral imaging techniques are classified based on the number and width of the spectral bands they record. Multispectral imaging records images within discrete bands. Hyperspectral imaging records images within narrower bands, over a continuous range, providing higher wavelength resolution than multispectral imaging. A more recent technology, ultraspectral imaging, employs an interferometer to record images with even higher wavelength resolution, and provides the highest resolution of all three techniques [81]. Ultraspectral imaging has not yet been applied in agriculture.

The main advantage of spectral reflectance imaging techniques is that aerial photographs are readily recorded on a large scale using remote sensing platforms such as satellites, aeroplanes, balloons and helicopters [82]. Yet, the use of satellites and high altitude airborne sensors is limited by their spatial resolution and the availability of acquisition times [83]. More recently, unmanned aerial vehicles (UAVs) have gained popularity due to their low cost of operation, high spatial and temporal resolution, and flexibility in image acquisition times [82]. However, these systems suffer from their reliance on miniaturised sensors, short flight times, inconsistent flight altitudes, and instability in winds [84].

Acquisition of high resolution spectra over a wide spectral range presents considerable challenges for data handling [85]. To develop a practical sensing system, identification of a stress-specific spectral band or bands is necessary, which can be a challenge, especially when monitoring disease [86].

1.3.3 Detection of Plant Volatile Organic Compounds

As discussed in Section 1.2, analysis of plant VOCs can provide information on the health status of plants. Since stress can induce specific changes in the VOC composition of a plant, techniques for monitoring plant health based on VOC analysis have the potential to be more diagnostic than image-based techniques which mostly detect generic symptoms manifested in the leaf. Electronic nose devices, gas chromatography–mass spectrometry instruments, and proton transfer reaction mass spectrometry instruments are the most common approaches used for these analyses. Cavity enhanced absorption spectroscopy is an optical technique evaluated in this thesis to determine its suitability for plant VOC detection and analysis, and could have advantages over the other VOC detection methods in a field setting.

1.3.3.1 Electronic Nose

Detection of plant volatiles is a relatively new application for electronic noses [86]. So far, electronic noses have been used on plants to discriminate VOC mixtures released by healthy, mechanically damaged, and diseased or pest-infested cucumber (*Cucumis sativus* L. cv. Telegraph Improved) and tomato (*Lycopersicon esculentum* cv. Carousel) leaves [87], to detect early stage fire blight in pear plants (*Pyrus communis* L. cv. Abbé Fétel) [88], and to detect basal stem rot disease in oil palm (*Elaeis guineensis* Jacquin) plantations [89].

The classic and most common electronic nose consists of an array of gas sensors arranged to mimic the biological receptors in the mammalian olfactory system [90]. The sensors have different coating materials that determine electrical currents within the sensor, which is then detected and converted into an electronic signal by a transducer [91]. As each sensor has specific sensitivities, the recorded data can be combined with a pattern processing algorithm to recognise a gaseous mixture [90].

In general, high specificity requires an irreversible interaction between the sensor and the target compound [90]. For example, olfactory sensory neurons in mammals have an average lifetime of about 70 days after which they are replaced [92]. Since the lifetimes of the sensors in electronic noses need to be much longer, these sensors are not fully selective [90]. Typically, electronic noses recognise gaseous mixtures as a whole, but cannot identify the individual components forming the mixture [93]. Electronic sensors that are sensitive and selective to more than a limited number of simple gases operate at very high temperatures (300 – 550 °C), which results in high power consumption [94], [95]. In addition, they are sensitive to changes in temperature and humidity [94]. Therefore, field applicability of electronic noses is limited.

1.3.3.2 Gas Chromatography–Mass Spectrometry

Although it is not yet an established technique for the detection of crop stress in the field, gas chromatography–mass spectrometry (GC-MS) is often used to analyse plant volatiles, due to its high sensitivity and selectivity [5], [96]. The working mechanism of GC-MS is provided in detail in Section 2.4. The main disadvantage of GC-MS is that it is not a real-time analytical method [5]. Even though open-probe fast GC-MS technologies have been developed for real-time analysis, these methods still employ a laboratory sized GC-MS instrument [97], [98]. Portable GC-MS instruments are becoming increasingly available, but they still have a cycle time of 5-20 minutes per measurement [99], [100], [101], and are therefore not suited for real-time analysis. With the exception of a portable GC-MS instrument that uses ambient air as carrier gas [100], these instruments require regular renewal of a carrier gas cartridge, making unattended and uninterrupted long-term measurements impossible. Power demands of an analytical technique can also be problematic for field analyses where available power supply is usually limited. The power consumptions of currently available portable GC-MS instruments are rather high, ranging between 200 W and 600 W.

1.3.3.3 Proton Transfer Reaction–Mass Spectrometry

Proton Transfer Reaction Mass Spectrometry (PTR-MS) is widely used for fast and sensitive detection of trace levels of VOCs in the atmosphere [96], [102]. PTR-MS employs a soft ionisation technique where each analyte molecule gains one proton via collisions with gaseous hydronium ions (H_3O^+), leading to little or no fragmentation. Ions detected are mainly the protonated parent ions [102], so it is not possible to distinguish isobaric compounds [96]. Differentiation between isobaric compounds is essential in plant stress detection since many volatile compounds are emitted by plants as isomers that can indicate different stress factors. For example, in tobacco (*Nicotiana attenuata*) plants, mostly (Z)-GLVs are released due to mechanical damage, but a roughly equal mixture of (Z)-GLVs and (E)-GLVs are released as a result of attack by the specialist herbivore *Manduca sexta* [103]. In addition, PTR-MS is sensitive to humidity in the environment. The primary hydronium ions can combine with water molecules in the air sample to form water cluster ions ($H_3O^+{\cdot}(H_2O)_n$) [104], producing peaks in the mass spectrum that may overlap with the analyte peaks. The clusters can also ionise VOCs via ligand switching reactions and further complicate the mass spectrum [105].

1.3.3.4 Cavity Enhanced Absorption Spectroscopy

Cavity enhanced absorption spectroscopy (CEAS) is a spectroscopic detection technique that employs an optical cavity to amplify the detection sensitivity. The principles of CEAS are discussed in detail in Section 2.2.2.2. CEAS can detect gases with high sensitivity. For example, at ambient temperature and 2.2 mbar, detection limits of 12 ppb and 46 ppb were achieved for N_2O and CH_4, respectively. At atmospheric pressures of approximately 1000 mbar, sub-ppb levels should easily be detected [106]. In fact, detection limits of 6 ppb for CH_4 at 15 mbar [107] and 225 ppt for N_2O at atmospheric pressure [108] were obtained. For NO, a detection limit of 8 ppt was achieved in a laboratory setting [108], and a detection limit of 3.6 ppbv ($\approx$ 3.6 ppb) was achieved in exhaled human breath [109], which contains as many as 500 different compounds [110]. Also in human breath, detection limits of 0.9 ppb and 0.3 ppb were reported for carbonyl sulphide and ethane, respectively [111]. Even though CEAS is considered a mature technique for the sensitive detection of gases, it has not yet been applied to the detection of plant VOCs.

In order to be a useful technique for the detection of plant VOCs, CEAS would need to show sufficient sensitivity and selectivity for these VOCs at the concentrations and in the matrices they may be found. Selectivity could be achieved for a molecule that has a unique absorption feature distinguishing it from the other gases that may be present in the mixture. Alternatively, a broadband spectrum could be recorded, and the various spectral features corresponding to pre-characterised species could be fitted. If GM sentinel plants are being used, the compound could be produced at significantly higher concentrations than other compounds when the corresponding gene is switched on. This disparity should allow the 'on' and 'off' states to be identified readily even if the baseline absorption contains signal from other compounds.

In this work, the sensitivity and selectivity of CEAS for the detection of gaseous geraniol will be determined to explore the suitability of this technique for the detection of plant VOCs. If CEAS proves suitable for plant VOC detection, a number of factors would make it a more favourable approach to field measurements than the existing molecular techiques of electronic nose and GC-MS detection. Unlike GC-MS, CEAS instruments do not require any consumables such as carrier gas, and therefore can operate for long periods of time without operator intervention. CEAS also does not involve sample preparation or chromatographic separation steps, so can take fast measurements for real-time monitoring of plant VOCs. Unlike both electronic nose and GC-MS instruments, CEAS sensors can operate at ambient temperatures and have reasonable power consumptions. The exact power demand of a cavity-based spectrometer would depend on a number of requirements such as the light source wavelength, the light source intensity, and the detector type. For methane, cavity-based portable detection systems with power consumption of 70 W [112] and 25 W [113] are commercially available.

1.4 Thesis Outline

In this chapter, the importance of detecting plant stress has been discussed and some of the most common techniques currently used for this purpose reviewed. The role of VOC emissions in plant defence and the potential of CEAS to exploit these emissions in order to monitor plant health have been summarised. In

Chapter 2, the theoretical and experimental methods employed in this work will be outlined, and the key equations used throughout the thesis will be presented. In Chapter 3, optical feedback cavity enhanced absorption spectroscopy, a form of CEAS, will be used to detect geraniol samples in the gas phase and determine the relevant limits of detection. In Chapter 4, geraniol content of genetically modified tobacco (*Nicotiana benthamiana*) leaves, rose (*Rosa* 'English Princess') petals, and pelargonium (*Pelargonium* 'Attar of Roses') leaves will be analysed and the chemical composition of these tissues will be explored. Concentrations of geraniol expected in the headspace of tobacco and pelargonium leaf tissues will also be estimated. Finally, conclusions from this work will be presented and future directions will be discussed in Chapter 5.

2

Theoretical and Experimental Methods

Contents

Two experimental techniques were used to pursue the detection of geraniol. Optical feedback cavity enhanced absorption spectroscopy was used for the detection of gaseous samples of pure, commercially available geraniol in order to determine the achievable limits of detection for a future field-based CEAS sensor. To investigate the availability of geraniol and other VOCs in plant material headspace and extracts, gas chromatography—mass spectrometry was used, due to the availability of well-established and sensitive protocols for plant VOC quantification.

In this chapter, we describe the theoretical background for the experimental and computational methods employed. Rather than providing an exhaustive list of all the available technologies and associated theoretical frameworks, we focus on the methods used in the experiments and calculations in this work, the reasons for their use, and the underlying physical principles.

2.1 Ideal Gas Law

Ideal gas theory assumes zero volume occupied by gas molecules and no intermolecular forces between them. At moderately high pressures (hundreds of atmospheres), molecules are relatively close to each other and the long-range attractive forces between them become significant. The intermolecular attraction decreases the volume occupied by the gas, so the molar volume of a real gas is smaller than that predicted by the ideal gas law at moderately high pressures. At very high pressures, the volume occupied by molecules becomes significant in relation to the space between them, and molecular size can no longer be ignored. With increasing pressure, repulsion between molecules at short range increases the total volume occupied, so the molar volume of a real gas is larger than that of an ideal gas at very high pressures. At low temperatures, molecules have less kinetic energy, so they undergo collisions with lower energies, and intermolecular forces become more significant.

Deviations from ideal gas behaviour occur at low temperatures and high pressures, and these deviations are usually small. The ideal gas equation is therefore considered a useful approximation to the behavior of gases under normal conditions [114], and has been adopted in the present work. For an ideal gas:

$$PV = nRT \tag{2.1}$$

where P is the partial pressure of the gas, V is the volume occupied by the gas, n is the number of moles of gas, T is the temperature in units of Kelvin, and $R = 8.3144598$ J K^{-1} mol^{-1} is the gas constant.

The molar number density of the gas can be obtained by rearranging 2.1 into:

$$\frac{n}{V} = \frac{P}{RT} \tag{2.2}$$

Multiplying the molar density by Avogadro's number, $N_A = 6.0221208 \times 10^{23}$ mol^{-1} gives molecular number density, N:

$$N = \frac{PN_A}{RT} \tag{2.3}$$

Equation 2.3 will be used to convert between the minimum detectable number of molecules of gaseous geraniol and the minimum detectable partial pressure of geraniol.

2.2 Absorption Spectroscopy

Cavity enhanced absorption spectroscopy, as suggested by the name, is a form of absorption spectroscopy. Absorption spectroscopy is a widely used analytical technique that relies on the absorption of electromagnetic radiation by analyte molecules in the sample. It is a technique suitable for the detection of plant volatiles such as geraniol because it is universal, as all atoms and molecules absorb some wavelengths of electromagnetic radiation, and it is non-destructive, as it does not change the chemical composition of samples. When the energy of electromagnetic radiation matches the energy required for a molecular transition, the molecule absorbs the radiation and is excited to a higher energy level. The transition frequency and molecular energy levels are related via Planck's Law [115]:

$$\nu = \frac{E_1 - E_0}{h} \tag{2.4}$$

where ν is the frequency for the transition from a lower to a higher energy level, E_1 is the energy of the higher level, E_0 is the energy of the lower level, and $h = 6.626 \times 10^{-34}$ J s is Planck constant.

Microwave radiation excites only rotational transitions. Infrared radiation excites transitions between vibrational and rotational energy levels, i.e. rovibrational transitions. Ultraviolet and visible radiation excite transitions between electronic, vibrational, and rotational states, i.e. vibronic transitions [116]. A schematic diagram of these transitions can be seen in Figure 2.1.

Analyte molecules in a sample absorb electromagnetic radiation at certain wavelengths, resulting in the attenuation of the intensity of the radiation passing through the sample. The attenuation of the radiation and the properties of the sample are related through the Beer-Lambert Law [117]:

$$I = I_0 e^{-\alpha C l} \tag{2.5}$$

where I_0 and I are the radiation intensities incident on and transmitted through the sample, C is the concentration of the analyte, l is the absorption path length, and α is the molar absorption coefficient of the sample. The absorption cross-section of each molecule, σ is given by:

$$\sigma = \frac{\alpha}{N_A} \tag{2.6}$$

Rearranging Equation 2.5 gives:

$$\frac{I}{I_0} = e^{-\alpha C l} \tag{2.7}$$

which can be expressed in a base 10 logarithm as:

$$\frac{I}{I_0} = 10^{-\varepsilon C l} \tag{2.8}$$

where $\varepsilon = \frac{\alpha}{\ln 10}$ is the molar extinction coefficient.

Dimensionless values of absorbance, A, are defined in two ways:

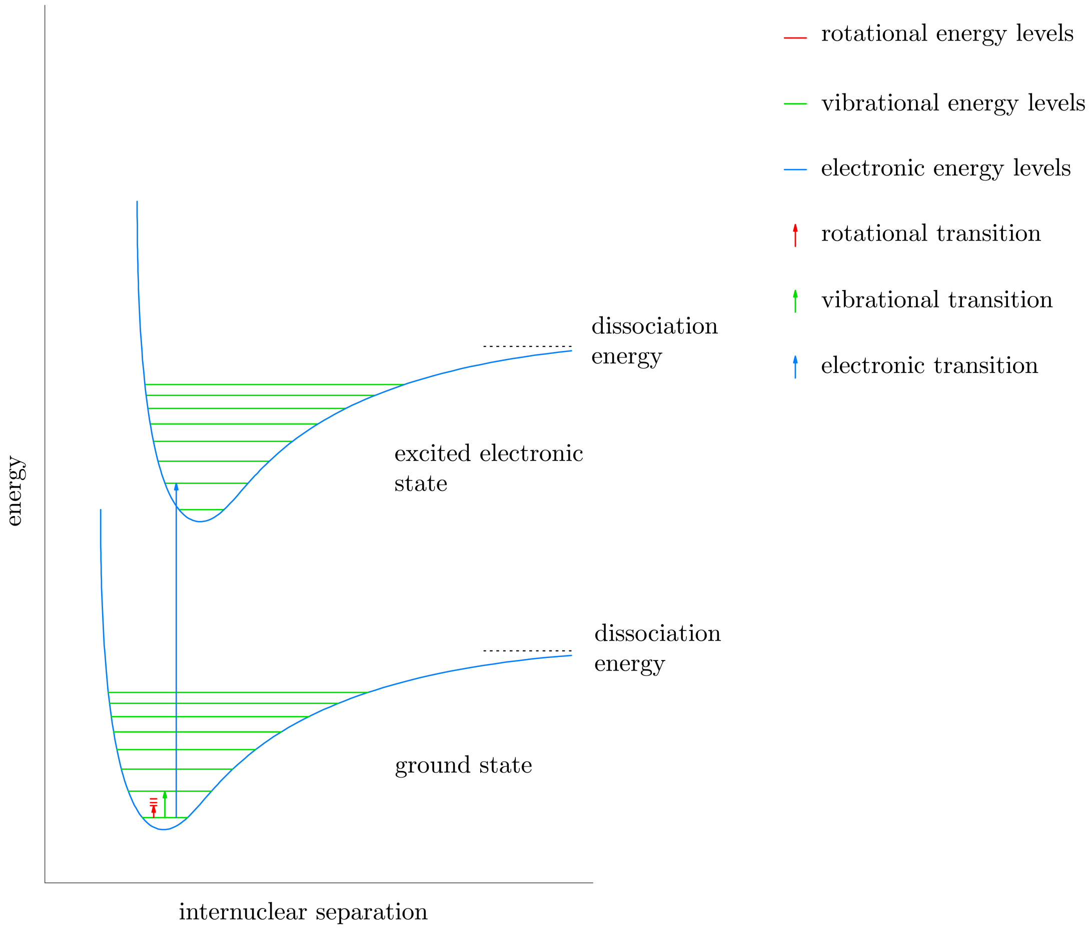

Figure 2.1: Schematic diagram of rotational, rovibrational and rovibronic transitions.

$$A = -\log \frac{I}{I_0} = \varepsilon C l \tag{2.9}$$

and

$$A = -\ln \frac{I}{I_0} = \alpha C l \tag{2.10}$$

The absorption for unit path length, κ, can therefore be expressed as:

$$\kappa = \frac{A}{l} = \alpha C \tag{2.11}$$

Absorption losses are very small close to the limit of detection such that

$-\ln \frac{I}{I_0} \approx 1 - \frac{I}{I_0} = \frac{I_0 - I}{I_0}$. Therefore, the minimum detectable absorption per unit path length is defined as:

$$\kappa_{\text{min}} = \frac{1}{l}\frac{(I_0 - I)_{\text{min}}}{I_0} = \frac{1}{l}\frac{\Delta I_{\text{min}}}{I_0} \tag{2.12}$$

where ΔI_{min} is the minimum detectable change in intensity and is defined as 3σ, three times the standard deviation in I_0.

2.2.1 Infrared Absorption Spectroscopy

CEAS of geraniol was performed with an infrared light source. The infrared (IR) region of the electromagnetic spectrum lies between wavelengths of 1 and 1000 μm. A bond between two atoms can absorb infrared radiation to oscillate with a higher amplitude, provided that the dipole moment of the molecule changes during the vibration. Molecules with a permanent dipole always absorb in the infrared, but molecules without a permanent dipole can also absorb in this region due to asymmetric stretches and bends. The number of unique vibrations, vibrational modes, of a molecule depends on the number of atoms in the molecule. Linear molecules have $3N - 5$, and nonlinear molecules have $3N - 6$ vibrational modes where N is the number of atoms in the molecule [118].

Each vibrational mode has its own characteristic vibration frequency. As discussed in Section 2.2, the energy of the electromagnetic radiation to which the molecule is exposed must match the spacing between vibrational levels in order to excite a transition. The transition frequencies (or wavelengths) can be used to identify the chemical bonds present in a sample. The infrared region below 1500 cm^{-1} provides especially useful information on the structure of organic compounds, as every compound has a unique absorption pattern in this region. This region is called the fingerprint region and contains many absorption bands due to bending vibrations as well as C–C, C–O and C–N stretching vibrations [118].

It is important to note that a ‘vibrational’ transition is actually a ‘rovibrational’ transition, since each vibrational transition is accompanied by a rotational transition with a selection rule $\Delta J = 0, \pm 1$, where J is the quantum number for total rotational angular momentum. The rotational energies of a molecule depend on its rotational constants A, B and C, each of which is related to the moment of inertia for the corresponding rotational axis:

$$A = \frac{h}{8\pi^2 c I_x}, \quad B = \frac{h}{8\pi^2 c I_y}, \quad C = \frac{h}{8\pi^2 c I_z} \tag{2.13}$$

where $c = 2.9979 \times 10^8$ m s^{-1} is the speed of light, and I_x, I_y and I_z are the moments of inertia about the x, y and z axes respectively.

For each rotational axis, the moment of inertia is given by [119]:

$$I = \sum_{i=1}^{N} m_i r_i^2 \tag{2.14}$$

where N is the number of atoms in the molecule, m_i is the mass of each atom, and r_i is the distance of each of the masses from the axis of rotation.

A rovibrational spectrum of geraniol will be simulated in Section 3.1.2, employing the principles for rotational transitions. Further details on the simulation are provided in Section 2.6.6.

2.2.1.1 Fourier Transform Infrared Spectroscopy

A vibrational spectrum of gas-phase geraniol was measured using Fourier transform infrared (FTIR) spectroscopy. A typical FTIR spectrometer uses a Michelson interferometer located between the radiation source and the sample to take measurements at all wavelengths of the covered electromagnetic region simultaneously. The interferometer contains a beam splitter, a fixed flat mirror, and a moving flat mirror. A schematic diagram of this setup can be seen in Figure 2.2. The beam splitter divides the incoming beam into two beams. One of the beams reflects off the fixed mirror and back to the beam splitter, always travelling the same fixed distance. The other beam reflects off the moving mirror, with the distance travelled varying depending on the position of the moving mirror. When the two beams recombine at the beam splitter, they have different phases and interfere with each other [120]. The produced signal is the intensity (interference pattern) plotted as a function of the position of the moving mirror, i.e. a function of distance. This signal, called

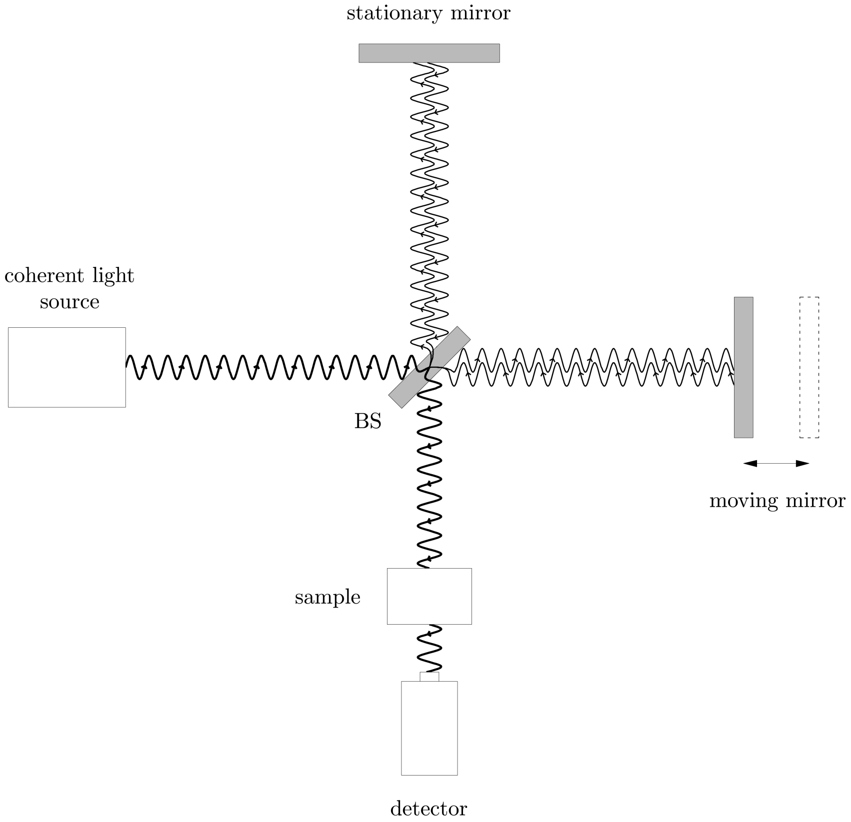

Figure 2.2: Schematic diagram of a Michelson interferometer typically found in an FTIR spectrometer. BS: beam splitter.

the interferogram, is Fourier-transformed to give the spectrum in wavenumbers. The interferogram, containing information about every wavelength produced by the radiation source, has a multiplexing advantage that enables fast measurements.

2.2.2 Cavity Enhanced Absorption Spectroscopy

When the concentration of the analyte is low, which is the case for many VOCs in the plant headspace, the attenuation of radiation passing through the sample can be extremely small and difficult to detect. In direct absorption spectroscopy, this would require an increased path length, and therefore a large volume of sample. However, cavity enhanced absorption spectroscopy (CEAS), also known as integrated cavity output spectroscopy (ICOS) [121], can circumvent this requirement. In this approach, the sample is contained within an optical cavity formed between a pair of highly reflective mirrors. The beam of radiation entering the cavity reflects back and forth between the mirrors, passing through and interacting with the sample hundreds or thousands of times. In this way, the optical path length is increased without increasing the sample volume [122]. The principles of CEAS are described in more detail in Section 2.2.2.2.

2.2.2.1 Optical Cavities

An optical cavity is an arrangement of optical components forming a resonator in which electromagnetic radiation forms standing waves and propagates in a closed path. The simplest example of an optical cavity is the Fabry-Pérot cavity, in which radiation undergoes repeated reflection between two coplanar mirrors [123]. For a cavity to behave as an optical resonator and allow the intensity of a beam of radiation to build up, the radiation must match one of the select frequencies supported by the cavity, known as cavity modes. In linear cavities, the beam of radiation must match one of the longitudinal modes of the cavity, by forming a standing wave inside the cavity. In order to fulfill this requirement, a half integer number of wavelengths must match the cavity length, as also seen in Figure 2.3. The wavelength of the radiation must satisfy:

$$q\frac{\lambda}{2} = d \tag{2.15}$$

where q is an integer, d is the cavity length, and λ is the wavelength within the cavity medium, i.e. $\lambda = \frac{\lambda_0}{n}$, with λ_0 the wavelength in vacuum and n the refractive index inside the cavity. The frequency of radiation must therefore satisfy:

$$\nu = q\frac{c}{2d} \tag{2.16}$$

Note that ν and λ, the frequency and wavelength of electromagnetic radiation respectively, are related to c, its speed, via:

$$c = \lambda\nu \tag{2.17}$$

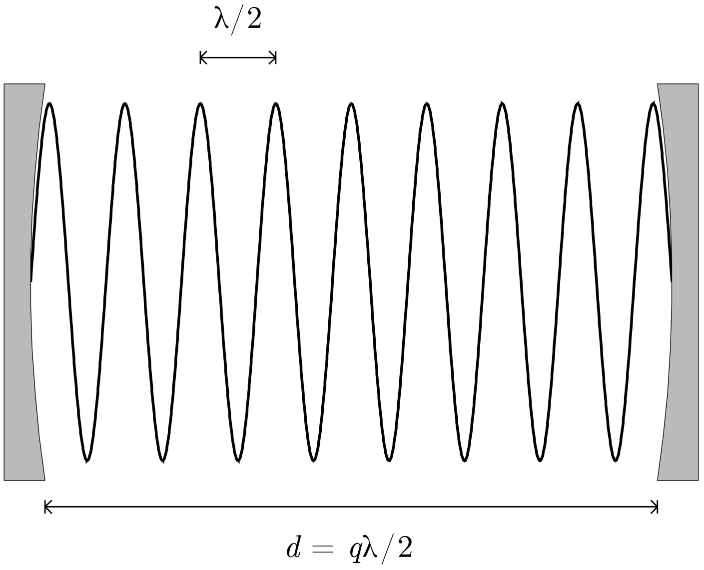

Figure 2.3: Schematic diagram of a longitudinal cavity mode fulfilling the requirement to form a standing-wave inside the cavity. The sine wave represents the amplitude of radiation along the cavity length.

Cavity resonance occurs for radiation with wavelengths such that exactly q half waves fit in the cavity. From Equation 2.16, it is seen that equal spectral spacing exists between the longitudinal modes of a cavity. This spacing, $\Delta\nu$, is defined as the free spectral range (FSR):

$$\Delta\nu = \frac{c}{2d} \tag{2.18}$$

Due to the finite size and radius of curvature of the mirrors used in a CEAS setup, these planar waves, known as longitudinal modes, are not sufficient to fully describe the modes of a real cavity [124]. Each longitudinal mode has an associated set of transverse modes corresponding to radiation propagating off axis. Cavity modes are solutions of Maxwell's equations for the electromagnetic radiation inside a cavity [125]. The allowed frequencies are quantised but with closer spacing than the longitudinal modes. Transverse modes form characteristic spatial patterns on the mirrors. For example, a cavity with cylindrical symmetry has transverse modes as shown in Figure 2.4. Each transverse mode is denoted TEM_{mn}, where m and n represent transverse mode indices [126]. For transverse modes associated with a cylindrical cavity, m represents the number of angular and n represents the number of radial nodes [127].

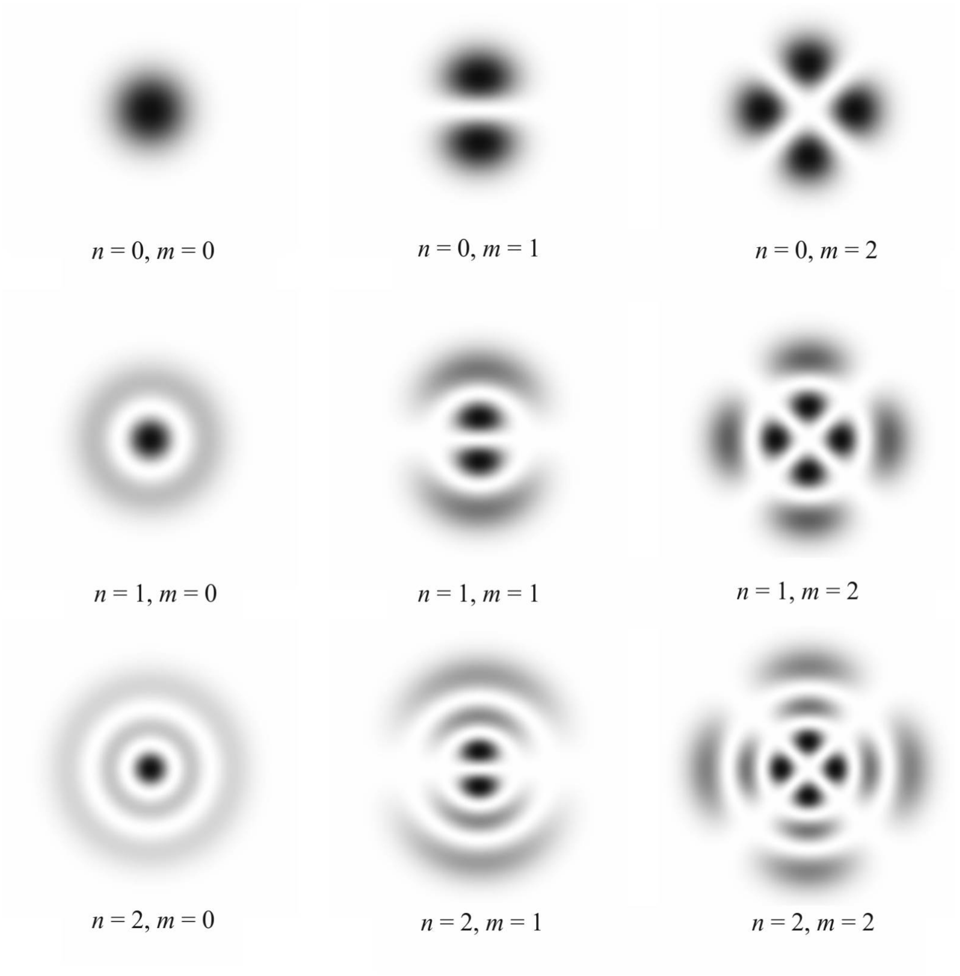

Figure 2.4: A selection of transverse modes for a cylindrical cavity.

For a longitudinal mode, $n = m = 0$, so a longitudinal mode can also be described as TEM_{00} [124]. In most CEAS experiments, the cavity mirrors are aligned such that the waist position and size of a Gaussian shaped beam matches the waist position and size of the cavity's TEM_{00} mode. The waist of a beam is defined as the size of the beam at the point of its focus. This approach, known as 'mode-matching', prevents the excitation of higher transverse modes which would otherwise introduce noise and other artifacts into the experiments [125], complicating data analysis.

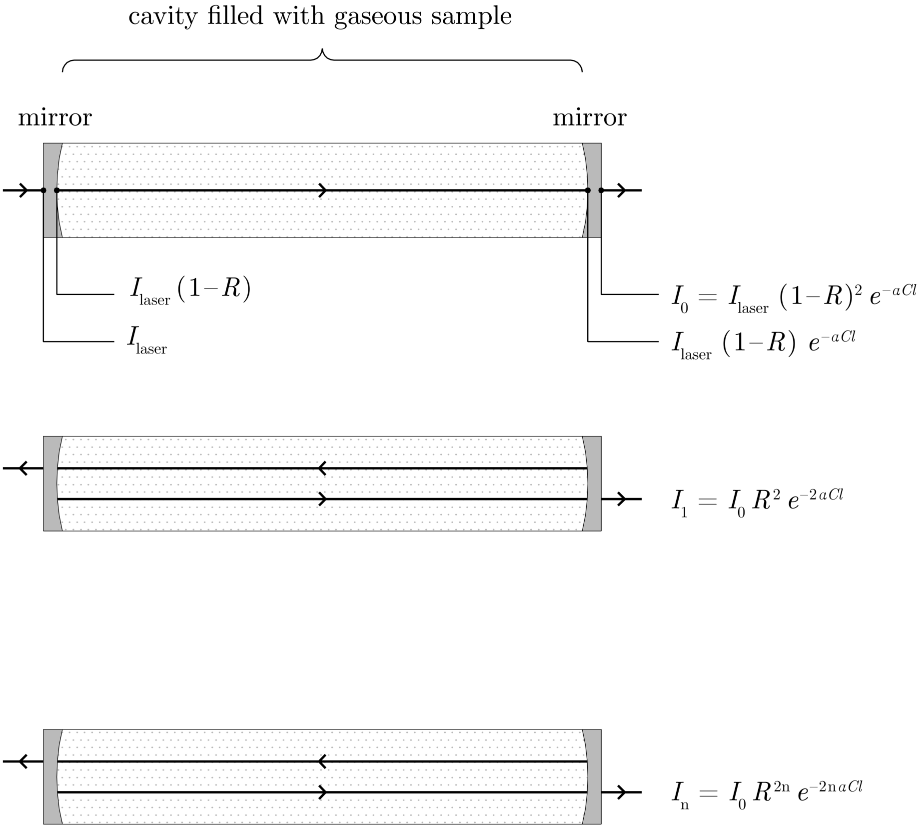

Figure 2.5: Schematic diagram of a CEAS setup showing the decrease in intensity as the number of round trips inside the cavity increases.

2.2.2.2 Principles of Cavity Enhanced Absorption Spectroscopy

A schematic diagram of a typical cavity enhanced absorption spectroscopy experiment is shown in Figure 2.5. Electromagnetic radiation is admitted to the cavity through the first mirror. The small amount of light coupled into the cavity undergoes multiple reflections, as well as absorption by the sample, and the small amount of light coupling out through the second mirror is detected. The detected signal is the total, time-integrated radiation output from the cavity, i.e. transmitted through the mirror further from the radiation source [122], [128], [129].

For an optical cavity with mirrors of reflectivity R, the transmission through the mirrors on each reflection is $T = 1 - R$. Radiation intensity is attenuated by a factor $1 - R$ on each reflection from a mirror, R on each transmission through a mirror, and $e^{-\alpha Cl}$ on each pass through the sample, with α the sample molar absorption coefficient, C the sample concentration, and l the absorption path length. Therefore, after excitation of the cavity with intensity I_{laser}, the output intensity I_0 after a single pass through the cavity is [130]:

$$I_0 = I_{\text{laser}}(1-R)^2 e^{-\alpha C l} \tag{2.19}$$

The second pass (first round trip) through the cavity results in further attenuation of radiation intensity due to reflection at each mirror and absorption by the sample:

$$I_1 = I_0 R^2 e^{-2\alpha C l} \tag{2.20}$$

Therefore, after n round trips, the intensity of output radiation is:

$$I_n = I_0 R^{2n} e^{-2n\alpha C l} \tag{2.21}$$

The fundamental principle governing CEAS is illustrated in Figure 2.5. The time-integrated intensity is a superposition of all intensities transmitted through the cavity after an odd number of passes [131]. This total intensity is an exact sum of the geometric series [129]:

$$I_{\text{out}} = I_{\text{laser}}(1-R)^2 e^{-\alpha C l} \sum_{n=0}^{\infty} R^{2n} e^{-2n\alpha C l} \tag{2.22}$$

The summation can also be expressed as $\sum \, (R^2 \; e^{-2\alpha C l})^n$ and converges to $\frac{1}{1-R^2 e^{-2\alpha C l}}$ because $R^2 e^{-2\alpha C l} < 1$. Therefore, the output intensity is given by:

$$I_{\text{out}} = I_{\text{laser}} \frac{(1-R)^2 e^{-\alpha C l}}{(1-R^2 e^{-2\alpha C l})} \tag{2.23}$$

The output intensity in the absence of an absorbing sample is given by:

$$I_{\text{out}}^0 = I_{\text{laser}} \frac{(1-R)^2}{(1-R^2)} \tag{2.24}$$

which is equal to:

$$I_{\text{out}}^0 = I_{\text{laser}} \frac{(1-R)}{(1+R)} \tag{2.25}$$

The ratio of intensities measured without and with an absorbing sample gives:

$$\frac{I_{\text{out}}^0}{I_{\text{out}}} = \frac{I_{\text{laser}}(1-R)(1-R^2e^{-2\alpha Cl})}{I_{\text{laser}}(1+R)(1-R)^2e^{-\alpha Cl}} = \frac{(1-R^2e^{-2\alpha Cl})}{(1-R^2)e^{-\alpha Cl}} \tag{2.26}$$

which can be rearranged to:

$$R^2(e^{-\alpha Cl})^2 + (1-R^2)\frac{I_{\text{out}}^0}{I_{\text{out}}}e^{-\alpha Cl} - 1 = 0 \tag{2.27}$$

Solving for $e^{-\alpha Cl}$ leads to:

$$e^{-\alpha Cl} = \frac{1}{2R^2}\left(\frac{I_{\text{out}}^0}{I_{\text{out}}}(R^2-1) + \sqrt{\left(\frac{I_{\text{out}}^0}{I_{\text{out}}}(R^2-1)\right)^2 + 4R^2}\right) \tag{2.28}$$

From Equation 2.11, $\kappa = \alpha C$, so rearranging Equation 2.28 gives:

$$\kappa = \frac{-1}{l}\ln\left[\frac{1}{2R^2}\left(\frac{I_{\text{out}}^0}{I_{\text{out}}}(R^2-1) + \sqrt{\left(\frac{I_{\text{out}}^0}{I_{\text{out}}}(R^2-1)\right)^2 + 4R^2}\right)\right] \tag{2.29}$$

For small absorption losses, $e^{-\alpha Cl} \rightarrow 1$ and for highly reflective mirrors, R→1. Hence, κ can be approximated as [131]:

$$\kappa = \frac{1}{l}\left(\frac{I_{\text{out}}^0}{I_{\text{out}}} - 1\right)(1-R) \tag{2.30}$$

which leads to:

$$\kappa_{\text{min}} = \frac{1}{l}\left(\frac{I_{\text{out}}^0}{I_{\text{min}}} - 1\right)(1-R) \tag{2.31}$$

Since $\frac{I_{\text{out}}^0 - I_{\text{min}}}{I_{\text{min}}} \approx \frac{I_{\text{out}}^0 - I_{\text{min}}}{I_{\text{out}}^0}$:

$$\kappa_{\text{min}} = \frac{1}{l}\left(\frac{\Delta I_{\text{min}}}{I_{\text{out}}^0}\right)(1-R) \tag{2.32}$$

A comparison of equations 2.12 and 2.32 shows that the ratio of minimum absorbance per unit path length with CEAS to that with single-pass absorption spectroscopy is $(1-R)$. This ratio indicates that CEAS is $(1-R)^{-1}$ times more sensitive than single-pass absorption spectroscopy, and it is therefore known as the cavity enhancement factor (CEF).

As per Equation 2.6, $\alpha C = \sigma N_A C$. C is related to molecular density N by:

$$C = \frac{N}{N_A} \tag{2.33}$$

Hence,

$$\alpha C = \sigma N_A \frac{N}{N_A} = \sigma N \tag{2.34}$$

Equation 2.30 can be written as:

$$\sigma N = \frac{1}{l}\left(\frac{I_{\text{out}}^0}{I_{\text{out}}} - 1\right)(1-R) \tag{2.35}$$

The minimum detectable number of molecules, N_{min} is given by:

$$\sigma N_{\text{min}} = \frac{1}{l}\left(\frac{\Delta I_{\text{min}}}{I_{\text{out}}^0}\right)(1-R) \tag{2.36}$$

Equation 2.35 can be expanded to give:

$$\sigma N = \frac{1-R}{l}\left(\frac{I_{\text{out}}^0}{I_{\text{out}}}\right) - \left(\frac{1-R}{l}\right) \tag{2.37}$$

Therefore, for small absorption losses and highly reflective mirrors, a plot of σN versus I_0/I gives a line with a gradient of $\frac{1-R}{l}$ and a y intercept of $\frac{-1+R}{l}$. In a standard CEAS experiment, the values of σ, R and l are known, and I_{out}^0 and I_{out} are measured. N for a sample can be calculated using Equation 2.37 and the measured signal from the cavity.

2.2.2.3 Optical Feedback Cavity Enhanced Absorption Spectroscopy

In this work, optical feedback cavity enhanced absorption spectroscopy (OF-CEAS) was employed for the detection of pure geraniol samples in the gas phase. Figure 3.4 in Section 3.2.1 shows a schematic diagram of the specific setup used for the experiments. OF-CEAS is a modified version of CEAS that employs feedback from the cavity to the laser in order to improve sensitivity. As the laser frequency is scanned, radiation at the cavity's resonant wavelengths builds up in the cavity and leaks back to the laser, which then 'locks' its emission frequency to this feedback frequency. In optical feedback locking, the laser frequency is not completely stationary but the tuning speed of the laser, i.e. the speed at which the laser frequency is scanned, is extremely slow [125], [132].

There are a number of advantages associated with the optical feedback modification to CEAS. The optical feedback locking mechanism increases the residence time of the laser at resonance, allowing for a complete intracavity build up [125]. The high power achieved at cavity resonance wavelengths enables the use of cavity mirrors with relatively higher reflectivities to increase the optical path length and achieve high sensitivities [133]. In addition, during optical feedback, the emission linewidth of the laser narrows down to below the cavity resonance width, which greatly increases the power of radiation within the resonance and improves the signal to noise ratio of the radiation signal [125]. Another advantage of OF-CEAS is the ability to adjust the locking range, the spectral width of the frequency range over which the laser stays locked to the resonance [125], [134], to be close to the cavity free spectral range, such that the laser virtually jumps from one longitudinal cavity mode to the next without scanning continuously. In this way, higher order transverse modes do not get injected into the cavity, so TEM_{00} modes are obtained without the need for mode-matching [125]. The automatic mode-matching of OF-CEAS also brings the practical advantage of allowing mirrors with small diameters to be used for a cavity with large base length, resulting in small intracavity sample volumes [135].

Cavity injection efficiency is the maximum cavity output at resonance [125]. The tuning speed should be slow enough for reproducible optical feedback interactions as the laser goes through resonance with consecutive cavity modes. It has been reported that, when compared with CEAS, OF-CEAS could achieve cavity injection gains over two orders of magnitude higher, even with tuning speeds three orders of magnitude higher [135].

Several schemes for OF-CEAS exist. Unlike simple, linear, two-mirror cavities, OF-CEAS cavities ensure that there is no direct feedback to the laser from the input cavity mirror. One common scheme is the V-shaped cavity with three concave mirrors that are usually identical [125]. For such a setup, an expression relating the absorption coefficient to the measured intensity signals can be obtained from the ratio of output intensities with and without an absorbing species, in a way similar to described in Section 2.2.2.2. At a resonant frequency, the ratio of the signal transmitted by the V-shaped cavity to the input laser intensity is given by [135], [136]:

$$\frac{I_{\text{out}}}{I_{\text{laser}}} = \frac{T^2 e^{-\alpha C \frac{L}{2}}}{(1 - R^2 e^{-\alpha C L})^2} \tag{2.38}$$

where $\frac{L}{2}$ is the length of one arm of a V-shaped cavity with two arms of equal length, and therefore of total length L.

In the absence of an absorbing species, the Equation 2.38 simplifies to:

$$\frac{I^0_{\text{out}}}{I_{\text{laser}}} = \frac{T^2}{(1 - R^2)^2} \tag{2.39}$$

The ratio of expressions in Equation 2.38 and Equation 2.39 gives:

$$\frac{I^0_{\text{out}}}{I_{\text{out}}} = \frac{(1 - R^2 e^{-\alpha C L})^2}{e^{-\alpha C \frac{L}{2}}(1 - R^2)^2} \tag{2.40}$$

Employing the approximations $\ln(1 - x) \approx -x - \frac{x^2}{2}$ ... and $1 - x^2 \approx 2(1 - x)$, and assuming small absorption such that $e^{-\alpha \frac{L}{2}} \approx 1$, Equation 2.40 leads to:

$$\alpha C = \frac{(1 - R^2)}{L}\left(\sqrt{\frac{I^0_{\text{out}}}{I_{\text{out}}}} - 1\right) = \frac{2(1 - R)}{L}\left(\sqrt{\frac{I^0_{\text{out}}}{I_{\text{out}}}} - 1\right) \tag{2.41}$$

Absorbance A can be defined as the expression in parentheses [132]:

$$A = \sqrt{\frac{I^0_{\text{out}}}{I_{\text{out}}}} - 1 \tag{2.42}$$

A can also be written as:

$$A = \frac{\alpha C L}{2(1 - R)} \tag{2.43}$$

A plot of A versus C gives a straight line with a gradient of $\frac{\alpha L}{2(1-R)}$.

By analogy to the derivation of Equation 2.32, the minimum detectable absorption per unit path length is given by:

$$\kappa_{\min} = \frac{2(1 - R)}{L}\left(\frac{\sqrt{I^0_{\text{out}}} - \sqrt{I_{\min}}}{\sqrt{I^0_{\text{out}}}}\right) \tag{2.44}$$

2.3 Langmuir Adsorption Model

Ideally, the CEAS measurements in this work would detect only gas phase geraniol from the pure samples injected into the cavity. However, our experimental data provided evidence that geraniol was adsorbing onto the cavity mirrors. The data was therefore analysed by assuming contributions to the cavity losses both from gas-phase geraniol and adsorbed geraniol. The adsorption process of geraniol onto the cavity mirrors was modelled using the Langmuir isotherm. The Langmuir isotherm treats the adsorbent gas as an ideal gas under isothermal conditions, i.e. constant temperature. It also assumes identical surface sites, mono-layer adsorption where each site on the surface can hold a single adsorbed molecule, and negligible interactions among adsorbed molecules [137].

An equilibrium reaction for adsorption of gas molecules onto a solid surface can be represented as:

$$[A] + [S] \rightleftharpoons [AS] \tag{2.45}$$

where [A] is the concentration of the unadsorbed gas molecules, [S] is the concentration of the unoccupied sites per area on the surface, and [AS] is the concentration of the occupied sites per area on the surface.

Let k_1 and k_{-1} be the rate constants for adsorption and desorption respectively. For elementary adsorption and desorption processes, the rate of adsorption is:

$$R_{\text{ads}} = k_1[A][S] \tag{2.46}$$

and the rate of desorption is:

$$R_{\text{des}} = k_{-1}[AS] \tag{2.47}$$

At equilibrium,

$$R_{\text{ads}} = R_{\text{des}} \tag{2.48}$$

which leads to:

$$k_1[A][S] = k_{-1}[AS] \tag{2.49}$$

Rearranging this equation gives:

$$\frac{k_1[A]}{k_{-1}} = \frac{[AS]}{[S]} \tag{2.50}$$

θ is defined as the fraction of occupied sites on the surface. Hence,

$$\frac{[AS]}{[S]} = \frac{\theta}{1-\theta} \tag{2.51}$$

Substituting Equation 2.51 into Equation 2.50 leads to:

$$\frac{k_1[A]}{k_{-1}} = \frac{\theta}{1-\theta} \tag{2.52}$$

Concentration $[A]$ is the number of moles of gas per volume:

$$[A] = \frac{n}{V} \tag{2.53}$$

For an ideal gas, $[A]$ is directly proportional to pressure through Equation 2.2. Rewriting Equation 2.52 with $[A]$ in terms of P gives:

$$P\frac{k_1}{k_{-1}RT} = \frac{\theta}{1-\theta} \tag{2.54}$$

A constant, K is defined such that

$$K = \frac{k_1}{k_{-1}RT} \tag{2.55}$$

Substituting Equation 2.55 into Equation 2.54 and rearranging leads to:

$$\theta = \frac{KP}{1+KP} \tag{2.56}$$

Figure 2.6 illustrates the dependence of θ on the pressure of the adsorbent gas in a system that follows the Langmuir isotherm. At low pressures, the fraction of occupied sites increases as the pressure of the available gas molecules increases. At high pressures, the sites on the surface approach saturation, so increases in pressure result in relatively smaller increases in the number of occupied sites.

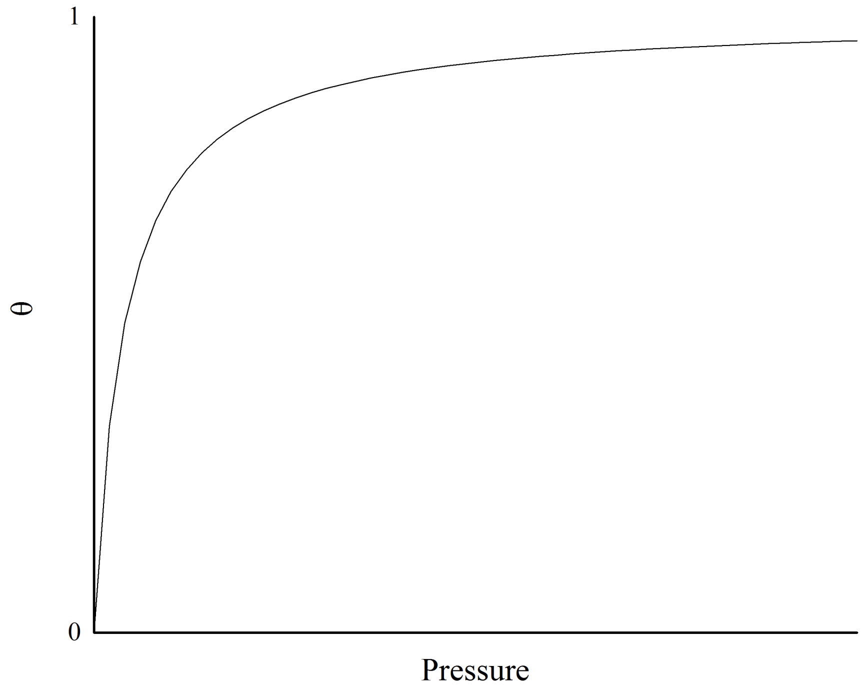

Figure 2.6: Fractional surface coverage, θ, as a function of pressure, predicted by the Langmuir isotherm.

2.4 Gas Chromatography–Mass Spectrometry

Due to its high sensitivity and well-established protocols within plant metabolomics, gas chromatography–mass spectrometry (GC-MS) was used to analyse the composition of plant material in this work. GC-MS is an analytical technique that combines gas chromatography and mass spectrometry to enable reliable identification and quantification of material. In this work, a time-of-flight (TOF) and a quadrupole time-of-flight (Q-TOF) GC-MS instrument were used for the plant liquid extract and headspace analyses, respectively. This section outlines the theories and working mechanisms of these instruments, which have similar operating principles with Q-TOF involving additional components. A schematic diagram of a Q-TOF GC-MS instrument is provided in Figure 2.7, and the outlined components are described in order in the remainder of this section.

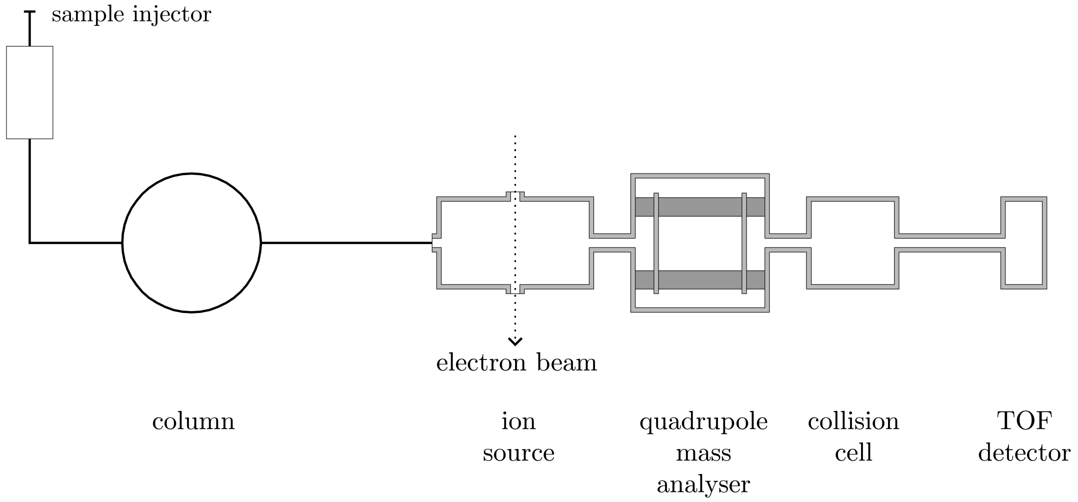

Figure 2.7: Schematic diagram of a Q-TOF GC-MS instrument.

2.4.1 Gas Chromatography

Gas chromatography is a technique used to separate a gaseous mixture into individual chemical components. A gas chromatograph consists of an injector, a column, a detector, and an oven that can heat the column [120]. A small amount of sample is fed into the injector that contains a vaporisation chamber lined by an insert which provides an inert space for samples to vaporise uniformly prior to being passed on to the column. For all GC-MS measurements in this work, a glass liner was used (SGE 4.0mm ID Split/Splitless FocusLiner 092002 [138] for headspace and Thermo Scientific 4.0mm Injection Port Liner 453A1925 [139] for plant extract measurements). The injector both vaporises the sample and mixes it into a flow of an inert carrier gas at the beginning of the column. The carrier gas is the 'mobile phase' that transports the analytes through the column.

The most commonly used column type in modern instruments is capillary (open tubular) column. Capillary columns are made of highest purity fused silica [120] which is chemically inert [140] but vulnerable to cracking [141]. They are protected [142] and made flexible by an outer coating of polyimide or aluminum [120]. Both of the GC-MS instruments used in this project are equipped with capillary columns. A thin layer of 'stationary phase' is either deposited on or chemically bound to the inner surface of the column [120]. As the analytes travel through the column, they interact differently with the stationary phase, and separate depending on their volatility and polarity. Volatile analytes travel faster through the column. In general, ‘like dissolves like’, so the stationary phase to separate a compound of a given polarity should be of a similar polarity [143]. Polar analytes interact more strongly with a polar stationary phase than non-polar analytes, and travel more slowly through the column [144].

The most common class of stationary phases is polysiloxanes [143]. The column used for GC-MS analysis of plant extracts in this work is slightly polar with a 5% phenylmethyl stationary phase, and the one used for headspace measurements on tobacco leaves is nonpolar with a (5%-phenyl)-methylpolysiloxane stationary phase [145]. Wax-type columns contain polyethyleneglycols (PEG), a polar class of stationary phases [143]. The GC-MS column used for the headspace analyses of rose petals and pelargonium leaves has a SolGel-WAX™ stationary phase which consists of PEG dissolved in a sol-gel matrix and coated onto the inner surface of the column [146], [147], [148]. This type of column is more inert and more thermally stable than a regular PEG stationary phase column [146].

At the end of the column, the analytes are quantified by the detector. Each analyte has a specific retention time, the time it takes for the analyte to reach the detector. In the case of a GC-MS instrument, the detector is replaced by a mass spectrometer, also known as a mass spectrometry detector or a mass selective detector (MSD).

2.4.2 Mass Spectrometry

In a GC-MS instrument, the effluent containing separated analytes from the gas chromatogram is fed into the mass spectrometer, where a mass spectrum is recorded separately for each analyte peak in the chromatogram. Mass spectrometry characterises sample material based on the mass-to-charge ratio (m/z) of individual components in the sample. A typical mass spectrometer consists of an ion source, a mass analyser and a detector.

2.4.2.1 Ion Source

In the ion source, a small amount of sample is ionised. A common vacuum ionisation technique is electron ionisation (EI) which is employed by both of the GC-MS instruments used in this work. In EI, analyte molecules are bombarded with electrons ejected from a filament. As a result, a small proportion of the analyte molecules lose their most weakly held electron and become positively charged. Negative ions are formed in small quantities and are not usually considered. The resulting positively charged ions have excess internal energy and dissociate through different pathways, producing various ion fragments [120].

2.4.2.2 Time-of-Flight Mass Analyser

In the mass analyser, ions are separated based on their m/z. The GC-MS instrument used to analyse liquids extracts of plant material in this work consists of a time-of-flight (TOF) mass analyser. TOF mass analysers measure the time it takes for ions accelerated through an electrostatic potential to travel a known distance to reach the detector. The charge q of an ion can be represented as $q = ze$ where z is the charge number and $e = 1.6021766209 \times 10^{-19}$ coulomb is the elementary charge. The kinetic energy E acquired by an ion of charge q accelerated through a potential difference U is given by:

$$E = zeU \tag{2.57}$$

The kinetic energy of a particle is also related to its mass, m and velocity, v:

$$E = \frac{1}{2}mv^2 \tag{2.58}$$

Under high vacuum conditions where collisions between ions are minimised, it can be assumed that all ions carrying the same charge acquire the same kinetic energy as a result of the same applied potential difference. Therefore, for all ions:

$$E = zeU = \frac{1}{2}mv^2 \tag{2.59}$$

Rearranging Equation 2.59 gives:

$$\frac{m}{z} = \frac{2eU}{v^2} \tag{2.60}$$

If it takes time t for the ion to fly the distance d from the ion source to the detector, then $v = \frac{d}{t}$, and substituting into Equation gives:

$$\frac{m}{z} = \frac{2eUt^2}{d^2} \tag{2.61}$$

TOF GC-MS instruments use the time it takes each ion to reach the detector, to determine its m/z through the relationship described by Equation 2.61 [120]. Light ions (low m/z) take less time to reach the detector than heavy ions (high m/z).

2.4.2.3 Quadrupole Time-of-Flight Mass Analyser

Another type of mass analyser is the quadrupole mass analyser. It is formed of four metallic rods that are electrodes coupled in pairs [120]. Ions of a selected m/z may be selectively transmitted through the quadrupole by the application of appropriate direct current (DC) and radio frequency (RF) potentials to the quadrupole rods. The RF and DC potentials or the RF frequency can be scanned to bring ions of successive m/z into resonance in order to record a mass spectrum.

The GC-MS instrument used for the headspace analyses in this work contains a quadrupole time-of-flight (Q-TOF) mass analyser that consists of a quadrupole analyser, a collision cell and a time of flight analyser. The 'precursor' ion is selected in the quadrupole based on its mass, accelerated, and injected into a collision cell containing an inert gas. As the ion travels through the inert gas, multiple collisions increase its internal energy until it fragments into smaller species. The resulting product ions are then mass analysed in the TOF mass analyser. The detection of the product ions for a specific precursor ion enables more accurate mass measurements than possible with regular TOF measurements [149]. The increased specificity of the precursor ion can also present a signal to noise ratio advantage [150].

2.4.2.4 Detection Systems

Several detection systems exist. The detection system inside the GC-MS instrument used for the plant extracts in this project couples a conversion dynode with an electron multiplier channel. The dynode emits electrons proportional to the number of positive ions hitting its surface [151]. These electrons are sent through an electron multiplier in the form of a horn-shaped channel, where they collide with the inner walls and cause the ejection of more electrons. The electrical signal amplified in this manner is then recorded [152].

The GC-MS instrument used for the headspace analyses of plant material contains a microchannel plate (MCP) detector. The MCP consists of a large array of microscopic channels in a honeycomb arrangement within a resistively coated glass substrate [151]. An ion hitting the front surface of the MCP causes the ejection of an electron. Each channel acts as a continuous dynode [120] and multiplies the number of electrons, which are then focused onto a scintillator that converts the signal into light. The light signal is amplified and converted into an electrical signal by a photomultiplier tube (PMT) [149].

2.5 Henry's Law

After determining the concentration of geraniol in plant tissue by GC-MS, Henry's Law was used to estimate the amount of gaseous geraniol that might be found around the tissue. Henry's Law states that the amount of a given gas dissolved in a given volume of a solvent is directly proportional to the partial pressure of the gas in equilibrium with the solvent, which can be expressed as [153], [154]:

$$P = kx \tag{2.62}$$

where P is the partial pressure of the gas, x is the mole fraction of the dissolved substance in solution, and k, the Henry's law constant, is a function of temperature and the physical properties of the gas and the solvent.

2.6 Computations

Since molecular absorption in the infrared region is a result of rovibrational transitions, the vibrational spectrum of geraniol was simulated to assist in the identification of sensitive and selective frequencies for measurement. The simulation of a molecule's vibrational spectrum relies on a detailed knowledge of its geometry, which can be computed via a number of electronic structure methods.

2.6.1 Schrödinger Equation

In classical mechanics, the dynamics of a system are predicted by Newton's second law of motion [155]:

$$\boldsymbol{F} = m\boldsymbol{a} \tag{2.63}$$

where $\boldsymbol{F}$ is the net force acting on the system of mass m, and $\boldsymbol{a}$ is the resulting acceleration of the system.

However, Newtonian laws are not successful in describing the behaviour of light and fast-moving particles at the subatomic scale [156]. The energy and motion of subatomic particles are described by quantum mechanics, and to account for the wave behaviour of such particles, the Schrödinger equation [157] must be solved. The electrons in molecular orbitals can be described by the simple, time-independent Schrödinger equation:

$$E\Psi = \hat{H}\Psi \tag{2.64}$$

where E is energy of the system, Ψ is the wavefunction that describes the system, and $\hat{H}$ is the Hamiltonian operator, which includes the kinetic energy operator $\hat{T}$ and the potential energy operator $\hat{V}$ for each particle in the system:

$$\hat{H} = \hat{T} + \hat{V} \tag{2.65}$$

and

$$\hat{T} = -\frac{\hbar^2}{2m}\nabla^2 \tag{2.66}$$

where $\hbar$ is $h/2\pi$ and $\nabla^2 = \frac{\partial^2}{\partial x^2} + \frac{\partial^2}{\partial y^2} + \frac{\partial^2}{\partial z^2}$.

2.6.2 Born–Oppenheimer Approximation

The Born–Oppenheimer approximation [158] was employed in our computations. This approximation simplifies the computation of the wavefunction and energy of a molecule. Since electrons are much lighter than atomic nuclei, but experience similar forces, they move with velocities much higher than those of the nuclei. Electrons can rearrange quickly in response to the movement of nuclei, so the Born–Oppenheimer approximation assumes that the nuclei can be approximated as stationary on the timescale of electronic motion, thereby decoupling electronic and nuclear motions. The overall wavefunction of the system can be written as:

$$\Psi_{\text{total}} = \psi_{\text{electronic}} \times \psi_{\text{nuclear}} \tag{2.67}$$

Therefore, the electronic part of the Schrödinger equation can be solved for a given set of nuclear positions, i.e. a fixed molecular geometry.

2.6.3 Hartree–Fock Approximation

In a molecule, $\hat{T}$ is the sum of kinetic energies of all nuclei and electrons:

$$\hat{T} = -\sum_{j=1}^{N} \frac{\hbar^2}{2m_i}\nabla^2 \tag{2.68}$$

where N is the number of particles and m_i is the mass of each particle.

$\hat{V}$ is the sum of electrostatic interactions within pairs of charged particles:

$$\hat{V} = \sum_{j=1}^{N}\sum_{i\neq j} \frac{1}{8\pi\varepsilon_0}\frac{q_i q_j}{|\mathbf{r}_i - \mathbf{r}_j|} \tag{2.69}$$

where $|\mathbf{r}_i - \mathbf{r}_j|$ is the distance between charges q_i and q_j and $\varepsilon_0 = 8.85418782 \times 10^{-12}$ F m^{-1}.

For systems with more than two particles, the electron-electron repulsion terms within $\hat{V}$ make the Schrödinger equation a many body problem and impossible to solve analytically.

Since it is not possible to find an exact solution to a many-body Schrödinger equation, various theoretical methods for approximating the solution exist. In this work, the Hartree–Fock (HF) approximation was used. The HF approximation ignores the individual and instantaneous electron-electron interactions, and instead considers the average repulsion between electrons. The method uses a set of approximate orbitals for each electron in the molecule, calculates the potential for the first electron, taking into account the forces exerted by the average distribution of all other electrons, and solves the Schrödinger equation using this potential, which gives a new orbital for the first electron. The process is repeated for each of the remaining electrons and eventually produces a new set of orbitals. The calculations are repeated iteratively until they reach a final set of orbitals consistent with the original set [159]. For this reason, the HF method is also known as the Self Consistent Field (SCF) method.

In reality, as an electron moves, other electrons will relocate to minimise electron-electron repulsion, so the correlation of electrons decreases the repulsion energy [156]. Methods that do not take into account electron correlation effects, such as the HF method, overestimate the electron-electron repulsion, and so the ionic character of the covalent bond, i.e. polarity [160]. Therefore, these methods underestimate the bond length and overestimate the vibrational frequencies. A scaling factor of 0.8929 is commonly used on calculated frequencies to obtain values similar to experimental frequencies [161], [162], [163], [164], [165].

Restricted Hartree–Fock (RHF) is used for systems in which all electrons are paired whereas Restricted Open-shell Hartree–Fock (ROHF) and Unrestricted Hartree–Fock (UHF) are used for systems with unpaired electrons [156].

2.6.4 6-31G* Basis Set

Each approximation method such as HF operates with a basis set to compute the approximate solution, i.e. the molecular wavefunction, to the Schrödinger equation. A basis set consists of basis functions for each atomic orbital within a molecule, and uses linear combinations of these basis functions to produce a mathematical approximation to the molecular orbitals. Two types of basis functions are common in electronic structure calculations: Slater Type Orbital (STO) and Gaussian Type Orbital (GTO) [156]. Slater orbitals are not often used, as they are computationally expensive. While minimal basis sets contain the minimum number of basis functions required for each atom, split valence basis sets represent the valence orbitals by multiple basis functions, since the valence orbitals are the orbitals that are involved in bonding [159].

The 6-31G* basis set was used in our calculations. In this basis set, each core orbital is represented by an optimised linear combination of six GTOs. Each valence orbital is described by two basis functions. The first basis function is a linear combination of three GTOs and the second wavefunction is represented by one GTO [156]. The * indicates a polarised basis set, where each valence orbital on atoms that are not hydrogen has an additional set of polarisation basis functions, so s orbitals have a set of p-type GTOs in their basis set, p orbitals have a set of d-type GTOs, and so on. This addition allows some asymmetry in molecular orbitals and helps represent a more accurate description of bonding, since the proximity of another atom polarises the orbitals and distorts the symmetry by changing the forces on the electrons.

As the size of a basis set increases, the calculation generates more accurate results but takes longer to complete. Therefore, the choice of a basis set is often a compromise between accuracy and computational expense. The 6-31 G* basis set is a medium-sized basis set that carries out the calculation in a reasonable length of time.

2.6.5 Root-Mean-Square Deviation of Atomic Positions

Once a geometry is computed for a molecule, it is often compared to alternative or literature geometries using the root-mean-square deviation (RMSD) of atomic positions, which provides a quantitative measure of similarity between superimposed structures [166]. RMSD for three-dimensional structures A and B is given by:

$$\mathrm{RMSD}(A, B) = \sqrt{\frac{1}{n}\sum_{i=1}^{n}\left((\mathrm{A}_{ix} - \mathrm{B}_{ix})^2 + (\mathrm{A}_{iy} - \mathrm{B}_{iy})^2 + (\mathrm{A}_{iz} - \mathrm{B}_{iz})^2\right)} \tag{2.70}$$

where n is the number of atoms in each molecule, A_{ix}, A_{iy}, A_{iz} are the x, y and z coordinates of the ith atom in A, and B_{ix}, B_{iy}, B_{iz} are the x, y and z coordinates of the ith atom in B, respectively.

2.6.6 Vibrational Simulation

In this work, a vibrational spectrum of geraniol was simulated using Gaussian 09 [167] and PGOPHER [168]. For a complete spectrum, line positions, line intensities, and line widths were calculated.

2.6.6.1 Line Positions

Molecular bonds can be modelled as springs acting as harmonic oscillators. The force **F** acting on a harmonic oscillator is [119]:

$$\mathbf{F} = -k\mathbf{x} \tag{2.71}$$

where k is the spring constant and **x** is the displacement from the equilibrium. Integrating **F** with respect to **x** gives the energy stored in a harmonic oscillator, which is also the potential energy term in the Hamiltonian operator for a harmonic oscillator:

$$V = \frac{1}{2}kx^2 \tag{2.72}$$

The energy levels corresponding to the eigenvalues of $E\Psi = \hat{H}\Psi$ for a harmonic oscillator are:

$$E_v = \omega_e \left(v + \frac{1}{2}\right) \qquad v = 0, 1, 2, 3, \ldots \tag{2.73}$$

where E_v is energy in units of cm^{-1}, v is the vibrational quantum number, and $\omega_e = \frac{\omega}{c}$, with ω the frequency of oscillation in Hertz.

The vibrational levels in a harmonic oscillator increase in energy by ω_e. Even though the harmonic approximation is valid for a molecule close to its geometric equilibrium, anharmonic potentials can have a significant effect. To include anharmonicity, the vibrational energy can be expressed as a series expansion with correction terms:

$$E_v = \left(v + \frac{1}{2}\right)\omega_e - \left(v + \frac{1}{2}\right)^2 \omega_e x_e + \left(v + \frac{1}{2}\right)^3 \omega_e y_e + \ldots \tag{2.74}$$

As indicated by this expression, in an anharmonic oscillator, which is a more accurate representation of real molecules, the vibrational level spacing reduces as v increases.

The vibrational spectrum of geraniol was simulated from computations of the vibrational energy levels using Gaussian 09. The energy differences between vibrational levels indicate the position of vibrational spectral lines in the spectrum.

2.6.6.2 Line Intensities

The line intensities in a vibrational spectrum are determined by the intensity of incident light, difference in population of the lower and upper states, and degree of overlap between the initial and final vibrational wave functions. The latter two factors were calculated by PGOPHER to simulate the intensities of lines in the spectrum of geraniol. The overlap between two wavefunctions Ψ' and Ψ'' is the square of the transition moment which is defined by:

$$R = \int \Psi'^{*} \mu \Psi'' d\tau \tag{2.75}$$

where dτ is an infinitesimal volume element and μ is the electric dipole moment operator given by:

$$\mu = \sum_i q_i \mathbf{r}_i \tag{2.76}$$

where q_i is the charge and $\mathbf{r}_i$ is the position vector of the ith particle (electron or nucleus) [119].

At ambient temperatures, the most populated states are often the lowest energy states. These populations are described by the Boltzmann distribution:

$$\frac{N_i}{N_0} = g_i e^{\frac{E_0 - E_i}{kT}} \tag{2.77}$$

where N_i and N_0 are the populations of state i and the ground state respectively, g_i is the degeneracy and E_i is the energy of state i, E_0 is the energy of the ground state, $k = 1.38064852 \times 10^{-23}$ J K^{-1} is the Boltzmann constant, and T is the temperature in Kelvin [119], considered 300 K in our PGOPHER simulations.

2.6.6.3 Line Widths

Three main factors contribute to the width of vibrational lines in the absence of an electric field [169]. Natural line broadening is a result of the uncertainty in the energy of the excited state. Population of an excited state will decay to the lower state until the original Boltzmann distribution is reached. The lifetime of the excited state is denoted τ. As described by Heisenberg's uncertainty principle:

$$\tau \Delta E \geq h \tag{2.78}$$

where ΔE is the uncertainty in energy of the excited state. Since τ is always finite, the excited state will not have an exactly defined energy. Therefore, all energy levels have natural broadening [119]. However, natural broadening is the smallest contributor to line width, and is often neglected in spectral simulations [169].

Pressure broadening, also known as collisional broadening, emerges from collisions between gas-phase molecules. These collisions reduce the lifetime of the upper state, and so increase the line width according to Heisenberg's uncertainty principle [119]. Pressure broadening becomes a major contributor to line width at high pressures and low temperatures [169].

Doppler broadening is a consequence of the Doppler effect arising from the distribution of molecular velocities. Gas molecules move randomly in all directions and with varying speeds. Depending on its velocity relative to the light source, a molecule will absorb incident radiation at a slightly different frequency. For instance, if a molecule is moving towards the light source, the transition will be observed at a slightly higher frequency. Doppler broadening becomes important at low pressures and high temperatures [169] because under these conditions, molecules move with long free paths before colliding with another molecule [170]. Doppler broadening was accounted for in our PGPOPHER simulations at 300 K with the broadening given by

$$\Delta\nu = \frac{\nu}{c}\sqrt{\frac{2kT\ln 2}{m}} \tag{2.79}$$

where m is molecular mass.

3

Optical Feedback Cavity Enhanced Absorption Spectroscopy Experiments

Contents

In this chapter, we acquire vibrational spectra of geraniol through experimental and computational methods, in order to identify suitable wavelengths for sensitive and selective detection of geraniol. Then, we apply OF-CEAS to the detection of gas-phase geraniol, and determine the likely limits of detection.

3.1 Infrared Spectroscopy of Geraniol Gas

Ideally, spectroscopic absorption measurements should be taken at a wavelength where geraniol absorbs strongly and where other compounds that may be present in the plant headspace (water, carbon dioxide, other VOCs) do not. This ensures both sensitivity and selectivity of the measurements. To identify suitable spectroscopic absorption peaks to be explored in CEAS measurements, a gas-phase infrared spectrum of geraniol was recorded using a commercial FTIR spectrometer and simulated using computational methods.

3.1.1 Sample Preparation

Liquid geraniol was purchased from Sigma-Aldrich (product number: 163333). The liquid sample was placed in an L-shaped Swagelok tube which, through a valve, was connected to a fixed 10 cm path length Storm 10H heated gas transmission cell by Specac, with calcium fluoride windows. With the valve closed, the gas cell was brought to a low pressure of approximately 2 mbar in order to favour gaseous geraniol over liquid geraniol and increase the amount of geraniol flowing from the sample tube into the gas cell when the valve was opened. The Swagelok tube was heated to 110 °C using an electric rope heater connected to a variable transformer. The temperature of the tube was monitored with a Type K thermocouple and regulated by adjusting the variable transformer. The valve was opened to allow gaseous geraniol to travel from the tube into the gas cell before an FTIR spectrum was measured.

During the initial FTIR measurements, it was discovered that the geraniol sample contained a large amount of water, which condensed onto the gas cell windows. The condensation rendered any meaningful measurements impossible because of large water absorption signals overlapping with sample absorption peaks. Drying glassware with a Bunsen Burner and under vacuum, keeping geraniol over activated molecular sieves (Acros Organics, 3Å, 8 to 12 mesh) and under a positive pressure of argon gas, and degassing the geraniol by freeze-pump-thaw cycles prior to measurement resulted in a clearer infrared spectrum with water peaks of lower intensity. No condensation was observed on the gas cell windows when these measurements were taken.

3.1.2 Computations

In order to find a rovibrational line unique to geraniol, vibrational frequencies and rotational constants were computed following a geometry optimisation on geraniol. The geometry optimisation was carried out using the Gaussian 09 electronic structure package. Calculations were performed at RHF/6-31G* level, employing strict convergence criteria. The resulting structure, visualised with Chem3D [171] in Figure 3.1, matched closely with the structure published in the PubChem database [172], with the RMSD of atomic positions of the two superimposed structures equal to 0.387 Å.

The anharmonic vibrational frequencies in units of wavenumbers were also computed at RHF/6-31G*. The computed vibrational wavenumbers were consistently higher than the literature values reported in the Vapor Phase Infrared Spectral Library hosted by Pacific Northwest National Laboratory (PNNL) [173], despite the inclusion of anharmonicity in the calculations. This discrepancy is most likely due to the fact that electron correlation effects are not included properly in the low level RHF theory employed in the electronic structure calculations. A correction factor of 0.888 was therefore introduced to ensure better agreement with the published values. This factor is similar to the scaling factor of 0.8929 commonly used on calculated frequencies as discussed in Section 2.6.3, and was determined from the ratio of the wavenumbers at which the highest energy transition occurred in the literature and simulated spectra. The resulting fit can be seen in the simulation depicted by Figure 3.2. In this simulation, PGOPHER was used to calculate the line intensities from the Boltzmann distribution and line widths from Doppler broadening at 300 K and as described in Section 2.6.6.

3.1.3 Fourier Transform Infrared Spectrum

The infrared spectrum was recorded using a Bruker VERTEX 80 FTIR spectrometer in a nitrogen-filled glovebox. Despite the relatively high spectrometer resolution of 0.5 cm^{-1}, the absorption features in this spectrum were fairly broad, with no fine structure observed. It was concluded that geraniol, with numerous freely rotating bonds, is too flexible to exhibit sharp rovibrational lines in the infrared spectrum. Computations to find a unique rovibrational line for geraniol were therefore terminated, and attention turned to an empirical determination of characteristic absorbing regions in the spectrum.

The experimentally measured spectrum of geraniol was found to be consistent with that reported in the PNNL database. PGOPHER was used to overlay the experimental and the PNNL spectra of geraniol with the spectra of possible

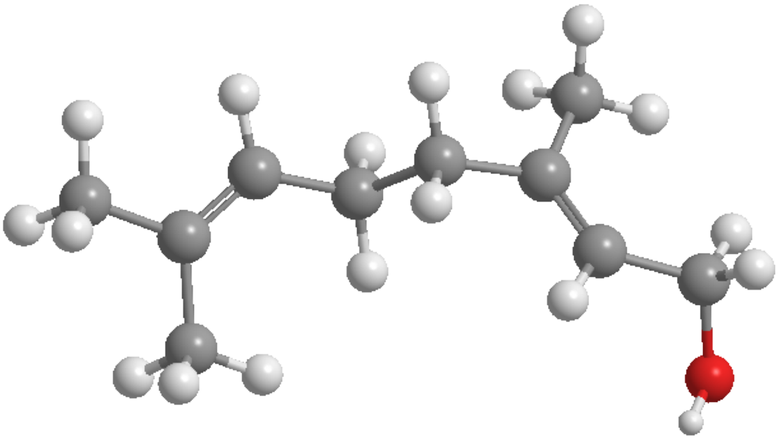

Figure 3.1: Three dimensional structure of geraniol computed using Gaussian 09 and HF/6-31G*.

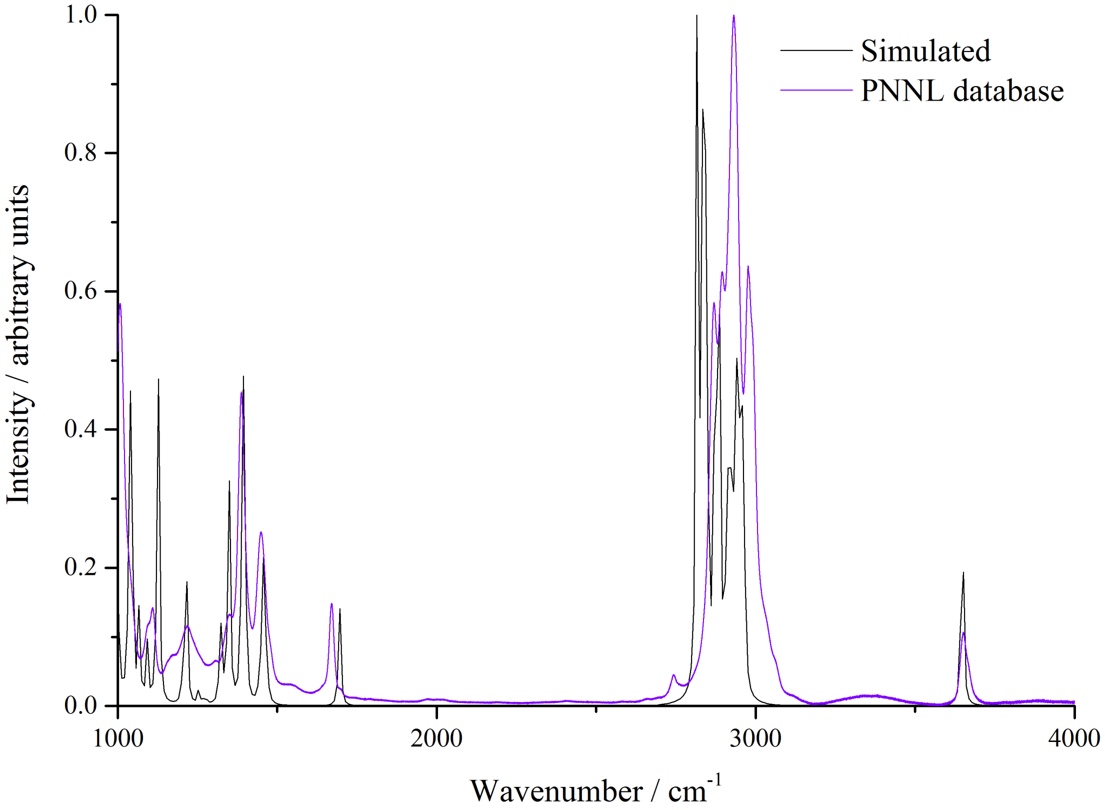

Figure 3.2: Scaled vibrational spectrum of geraniol simulated by Gaussian and PGOPHER, overlaid by vibrational spectrum of geraniol published by the PNNL database.

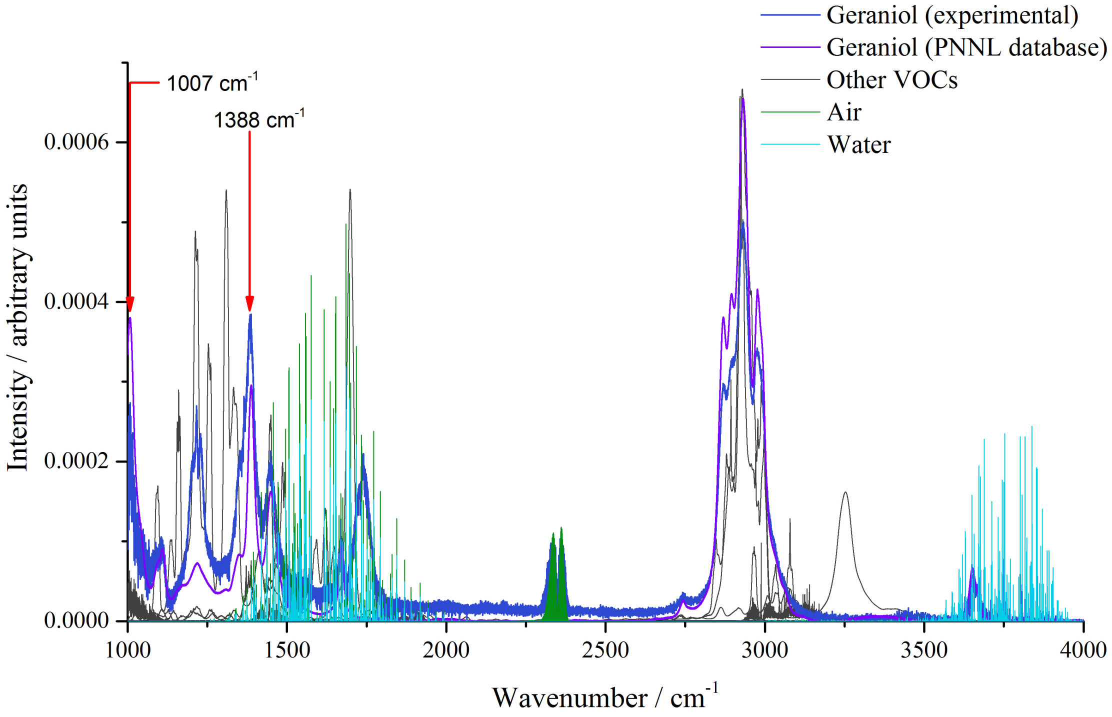

Figure 3.3: Experimental and literature spectra of geraniol overlaid with a selection of other VOCs, water and air. Other VOCs: α-pinene, β-pinene, methyl salicylate, ethane.

contaminants obtained from the PNNL database (α-pinene, β-pinene, methyl salicylate, ethane), and with a spectrum of atmospheric air obtained from the HITRAN database [174] This overlay can be seen in Figure 3.3 and allowed the identification of spectral features of interest in regions where the geraniol signal has little or no overlap with possible interferent peaks. Features in the spectrum of geraniol that overlap with the absorption region of water must especially be avoided, since a high concentration of water vapour is expected in the plant headspace. Peaks at 1007 cm^{-1} and 1388 cm^{-1} were identified as being suitable for further investigation as they have significant intensities, without too much overlap from other potential interferents.

3.2 Optical Feedback Cavity Enhanced Absorption Spectroscopy on Geraniol Gas

3.2.1 Experimental Setup

A V-shaped cavity of length 86 cm (two 43 cm arms) was used to measure gaseous geraniol at varying partial pressures. These measurements were performed in collaboration with Dr. Katherine Manfred and Katharine Hunter from Grant Ritchie's research group, using the equipment in the Ritchie laboratory, so the existing experimental configuration and excitation wavelength could not be modified.

A schematic diagram of the OF-CEAS setup used in this experiment is provided in Figure 3.4. In this setup, a beam splitter (BS) splits off a small fraction of the beam so that it can be monitored. The remainder of the beam is used for the experiment. A steering mirror is mounted on a piezoelectric transducer (PZT) and reflects the radiation towards the cavity. Mirrors M0, M1 and M2 are spherical zinc selenide (ZnSe) mirrors. The cavity output signal is collected by an off-axis parabolic mirror (OAPM) and detected by a photovoltaic detector (PVD). The output signal is processed by the analog-to-digital (A/D) converter and computer software, and used to regulate the optical feedback phase through minor adjustments to the PZT.

For measurements of gaseous geraniol, the cavity was evacuated until a minimum stable pressure of 0.4 mbar was reached. Liquid geraniol was heated in an L-shaped Swagelok tube as described in Section 3.1.1. A small amount of evaporated geraniol was allowed to move into the cavity by briefly opening a valve between the heated tube and the cavity. The temperature of the heated tube fluctuated between 122 and 125 °C throughout the experiment. Gaseous geraniol was topped up to atmospheric pressure with nitrogen gas. An interband cascade laser (ICL) was used as the light source and was scanned over 3040.90 – 3041.67 cm^{-1}.

The cavity modes over the scanned frequency range can be observed in the signal transmitted through the cavity. Figure 3.5 illustrates the intensity of the signal transmitted through the cavity without geraniol over the scanned range of frequencies.

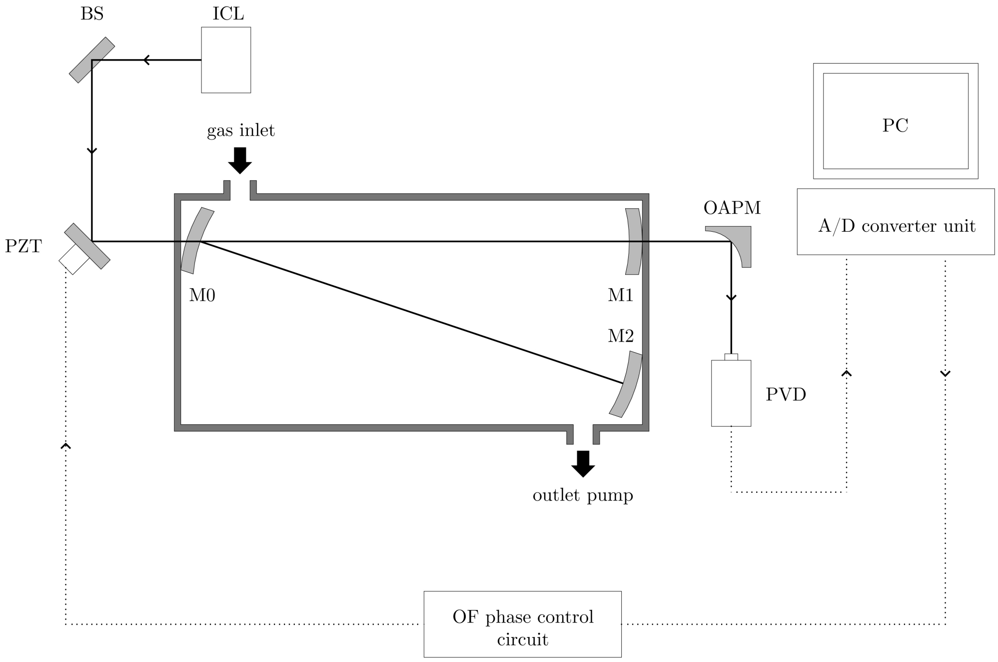

Figure 3.4: Schematic diagram of the OF-CEAS setup used. ICL: interband cascade laser, BS: beam splitter, PZT: piezoelectric transducer, M0-2: spherical mirrors, OAPM: off-axis parabolic mirror, PVD: photovoltaic detector, A/D: analog-to-digital.

Spectra of geraniol were recorded at a number of partial pressures in the range from 0.0002 to 0.1 mbar. The spectra were analysed using the OriginPro software package [175]. Spectral peaks were identified using the software's local maximum method, a peak finding algorithm based on local extrema. For every point on the input curve, the algorithm checks whether it is a local extremum and whether it satisfies a minimum threshold for peak height. The points that meet both the local extremum and the threshold value criteria are marked as peaks [176]. A range of 25 local points to determine the local extrema and a threshold height of 50% of the global maximum were used to select the peaks in the signal. Together, these peaks form the intensity of the signal transmitted through the cavity over time, for each partial pressure of geraniol (Figure 3.6).

It was discovered that geraniol condensed and formed a film on the cavity mirrors, possibly affecting the level of the transmitted signal both by increasing the total absorption and by changing the mirror reflectivity, R. In Figure 3.6, this effect can be observed by the shift in the baseline signal from the evacuated cavity at the beginning

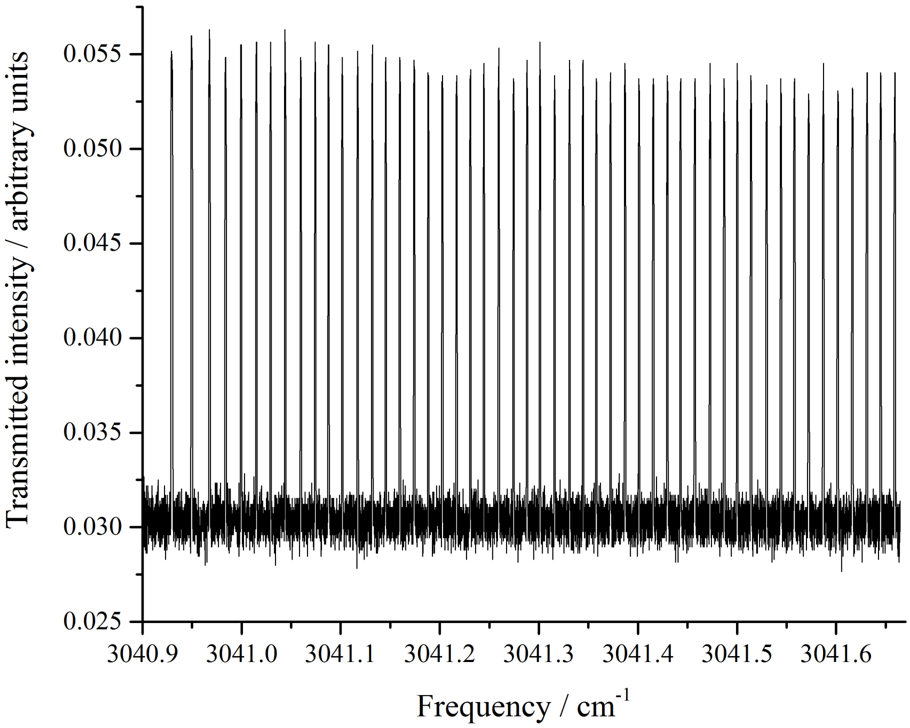

Figure 3.5: Signal transmitted through the cavity with no geraniol over the scanned range of frequencies.

and at the end of the experiment. In general, the transmitted signal was weaker for higher partial pressures of geraniol, as expected. This relationship can be seen more clearly with the average peak amplitudes in Figure 3.7. Absorbance, A, was obtained through the relationship in Equation 2.42: $A = \sqrt{\frac{I_{\mathrm{out}}^0}{I_{\mathrm{out}}}} - 1$ where I_{out}^0 is the cavity transmission without geraniol and I_{out} with geraniol. Measurements with a wide range of concentrations were taken as it was not clear at the time of the experiment what level of concentration should be expected in the headspace of a plant. With the OF-CEAS setup, the relationship between absorbance and partial pressure starts linear at low concentrations, but loses linearity at higher concentrations, unlike that expected from Equation 2.43. The reason behind the observed non-linear behaviour is speculated to be the condensation of geraniol on cavity mirrors, and further discussed in Section 3.2.2.1. As later discovered by the work described in Chapter 4, 670 and 1930 ppb of geraniol could be reasonable estimations of

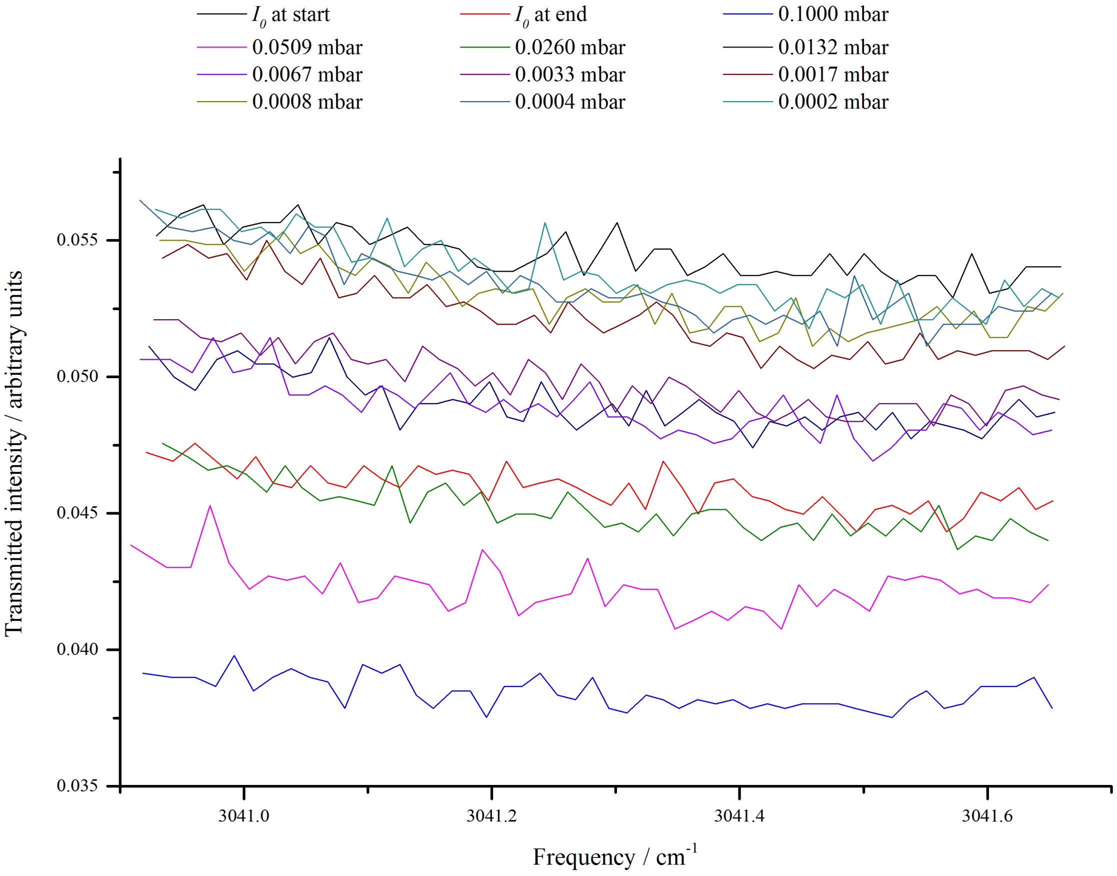

Figure 3.6: Transmitted signal corresponding to various partial pressures of geraniol present in the cavity. The x-axis represents the frequencies with maximum transmission through the cavity.

geraniol found around a plant. At atmospheric pressure, these two concentration values correspond to partial pressures of 0.0019 mbar and 0.0007 mbar respectively, and would fall around the third and fourth lowest concentrations data points in the performed OF-CEAS measurements. Therefore, the OF-CEAS measurements relevant to the expected concentrations of geraniol in a plant headspace lie in the linear region in Figure 3.8.

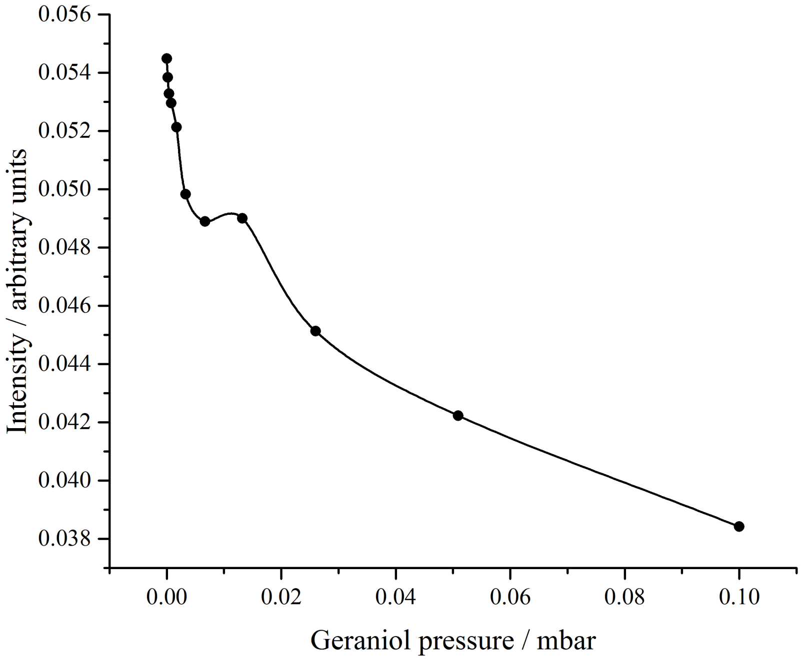

Figure 3.7: Average peak amplitude for various partial pressures of geraniol.

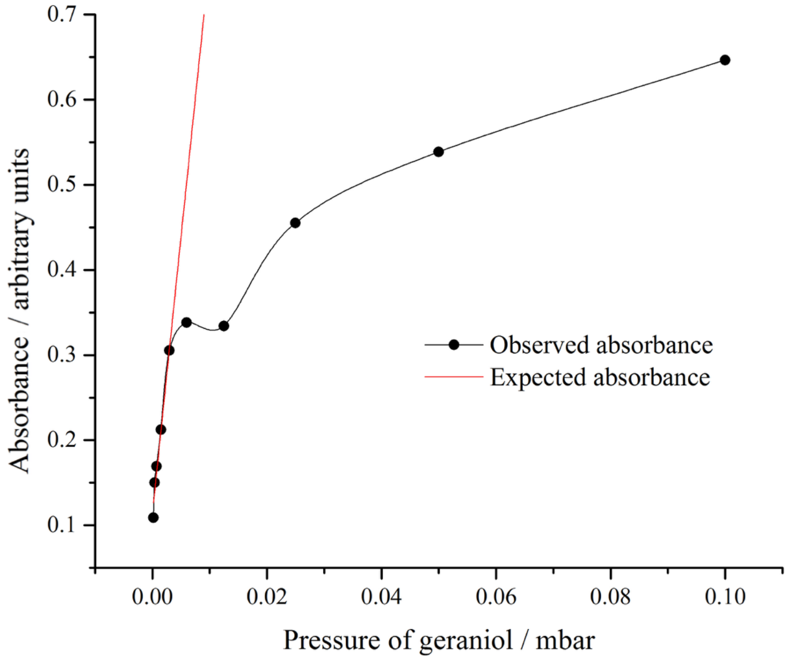

Figure 3.8: Expected and observed total absorbance for varying partial pressures of geraniol.

3.2.2 Analysis

3.2.2.1 Adsorption of Geraniol on Mirrors

In Figure 3.8, a phenomenon caused by the condensation of geraniol on the cavity mirrors can be observed. At low partial pressures of geraniol, the absorbance increases linearly with increasing pressure of geraniol. As the partial pressure increases further, geraniol begins sticking to the surface of the mirrors, changing the observed concentration dependence. Then, beyond a certain partial pressure, the effect of geraniol adsorption on absorbance starts levelling off. In this section, we model and discuss this behaviour.

To calculate the molar extinction coefficient values for geraniol over the wavelength range of interest via Equation 2.9, the equivalent concentration × path length values from the PNNL spectrum [173] were used along with the recorded absorbance values. The values from PNNL were converted into absorption cross section values. The average σ was found to be 6.1147×10^{-20} cm^2. R was measured to range between 0.9995 and 0.9997, so the value of R was taken as 0.9996. Therefore, this cavity has a CEF of $(1 - 0.9996)^{-1} = 2500$. The number density of geraniol at each pressure was calculated using Equation 2.2 and Equation 2.3 and $(1 - R)$ was calculated from Equation 2.35.

For constant mirror reflectivity, the value of $1 - R$ should stay at $1 - 0.9996 = 0.0004$. A change in this value would indicate a change in mirror reflectivity. At such a small range of scanned wavelengths, it can be assumed that any change in mirror reflectivity would come solely from the adsorption of liquid geraniol onto the mirrors. Therefore, the deviation from 0.0004 in the value of $1 - R$ at each pressure represents the additional loss in detected radiation intensity due the adsorption of geraniol at each pressure.

The additional losses were fit to the Langmuir isotherm model such that $L_{\text{additional}} = A\frac{KP}{1+KP}$, where A is a proportionality constant. The resulting fit had $A = 0.0373$ and $K = 0.3270$. The additional losses predicted by this fit match closely with the experimental losses, with $\chi^2 = 3.3397 \times 10^{-5}$. The additional

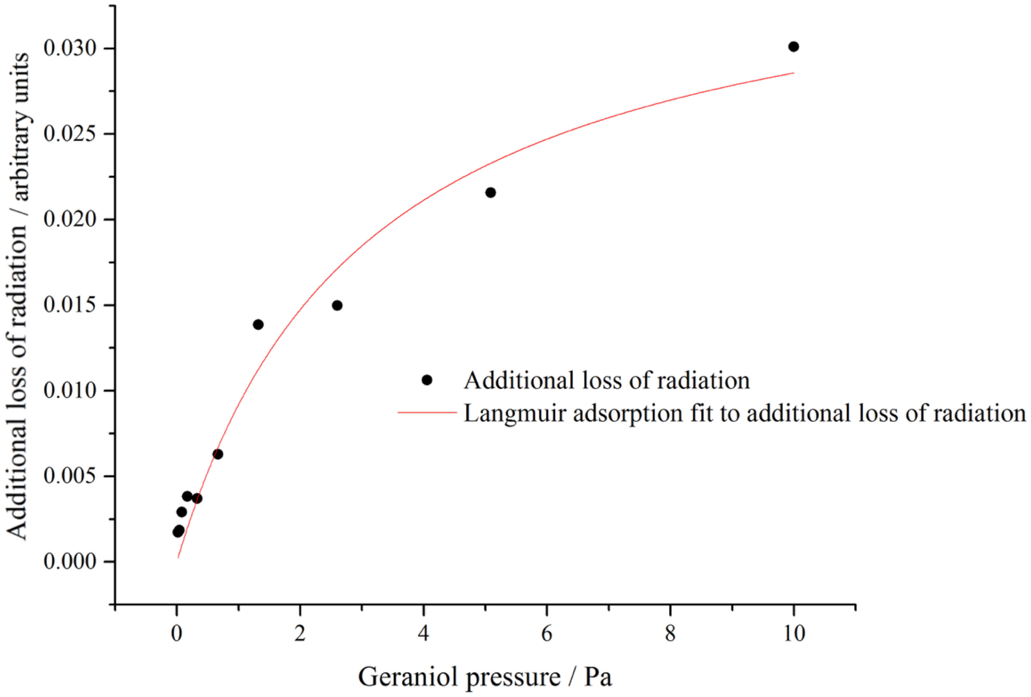

Figure 3.9: Additional loss in detected intensity due to adsorption of liquid geraniol on cavity mirrors, observed in our experiments and predicted by the Langmuir isotherm.

loss recorded for each pressure of geraniol and the corresponding additional loss predicted by the Langmuir isotherm model can be seen in Figure 3.9.

The data appear to be well-modelled by the single-layer Langmuir isotherm, even though there is not a physical reason to prevent multiple layers of geraniol from adsorbing onto the mirrors. It is, however, likely that the first layer of adsorption will cause the most significant change in mirror reflectivity, given that the reflectivity depends on the difference in refractive indices of the two media, i.e. air and mirror versus geraniol and mirror. Once all the available sites on the mirror have been filled with geraniol molecules, additional layers could start to form, but these layers would have smaller effects on mirror reflectivity compared to the initial layer.

3.2.2.2 Limit of Detection

The estimated concentrations of geraniol expected in the headspace of a plant in Chapter 4 lie in the region of OF-CEAS measurements that were virtually unaffected by the adsorption of geraniol on the mirrors. Even in a case with higher concentrations in the headspace, adsorption of geraniol onto the mirror surfaces could be eliminated by the heating of the mirrors in an alterable experimental setup. In such a setup, R would stay constant at 0.0004 and the detection limit could be calculated from Equation 2.44. This limit of detection would be $N_{\mathrm{min}} = 3.5715 \times 10^{12}$ molecules cm^{-3}. Following from Equation 2.3, this N_{min} value is equivalent to 147 ppb at atmospheric pressure.

Due to the limitations of the experimental configuration, the measurements were taken at a range of wavelengths that coincided with the tail end of an absorption feature of geraniol. Assuming that the achievable signal-to-noise ratio is similar at other wavelengths, the detection limit can be calculated at wavelengths for which the absorption coefficient is much larger. As demonstrated in Section 3.2, two wavelengths that are both sensitive and selective to geraniol are 1388 cm^{-1} and 1007 cm^{-1}. The limit of detection was calculated as 32.8 ppb at 1388 cm^{-1} and 25.5 ppb at 1007 cm^{-1}.

The significance of the CEAS limit of detection depends on the expected gas-phase concentration of geraniol in the headspace of a plant. The next chapter is devoted to establishing an approximate concentration for this purpose.

4

Gas Chromatography–Mass Spectrometry Experiments

Contents

In this chapter, we explore the levels of geraniol that may be present in plant tissues, employing GC-MS due to its sensitivity and available protocols for VOC detection. We determine a likely limit of detection for standard geraniol solutions, construct a calibration curve for quantification of geraniol in dichloromethane, and analyse headspace and liquid extracts of plant samples for their geraniol content, using GC-MS. Finally, we estimate the concentration of gaseous geraniol that may be present around plant tissues.

For these experiments, plant samples were chosen based on expected VOC composition and availability. The tobacco (*Nicotiana benthamiana*) plants were genetically engineered by Dong et al. to contain a geraniol synthase gene from *Valeriana officinalis*, and detached leaves of these plants were shown to emit between

5 and 55 nanograms of geraniol per gram of leaf per hour (ng g^{-1} h^{-1}) [67]. The typical rose scent is known to be due to beta-phenylethanol, geraniol, nerol, and citronellol [177]. *Pelargonium* 'Attar of Roses', a pelargonium cultivar, is known for its high geraniol content and rosy scent during flowering [178]. Therefore, petals and leaves from readily available plants of *Rosa* 'English Princess' and *Pelargonium* 'Attar of Roses' respectively were also selected as samples.

Geraniol was identified by comparison of retention index and fragment ions against a pure geraniol standard. Other compounds were tentatively identified by comparison of the major ion fragments against the National Institute of Standards (NIST) mass spectral library [179]. Compounds detected in *Rosa* 'English Princess' petal extracts were compared to compounds reported in *Rosa damascena* Mill. *Rosa damascena* Mill. is regarded as one of the most important species of rose plants [180], especially because it produces the majority of the world's rose oil, and has a significant role in traditional medicine [180], [181]. It was selected for the comparison simply due to the availability of literature data on the VOC composition of petals from this species. Compounds detected in *Pelargonium* 'Attar of Roses' leaves were compared to compounds reported in *Pelargonium graveolens*, *Pelargonium* cv. 'Bourbon', *Pelargonium crispum*, *Pelargonium filicifolium*, *Pelargonium capitatum*, *Pelargonium cv. 'Rose'*, and *Pelargonium tomentosum.*

4.1 Headspace Analyses

GC-MS headspace measurements were performed on plant samples to investigate their geraniol content. Mature leaves or petals were picked and immediately enclosed in 20 mL borosilicate glass vials. Samples of the headspace gas were injected into an Agilent 7200 Q-TOF GC-MS spectrometer between 30 and 90 minutes after collection. For tobacco, sample volumes of 36 µL and a non-polar column, Agilent J&W HP-5, were used. The oven temperature was initially held for 3 min at 50 °C, then increased to 300 °C at a 50 °C min^{-1} rate, and then held at 300 °C for 2 min. For rose petals and pelargonium leaves, sample volumes of 2.5 mL and a SolGel-WAX column were used. The oven temperature was initially held for 3 min at 80 °C, then increased to 300 °C at a rate of 25 °C min^{-1}, and held at 300 °C for 2 min. 'Baseline-corrected' total ion chromatograms were obtained by subtracting the corresponding blank vial chromatogram from each sample chromatogram.

4.1.1 Genetically modified *Nicotiana benthamiana* Leaves

No geraniol or any other VOCs were detected in the headspace of tobacco leaves, as shown in Figure 4.1. The level of geraniol in the headspace could be too low to detect without a pre-concentration step, considering Dong et al., who previously detected geraniol emissions from these plants, had employed a trapping method [67]. Subsequently, we decided to move on to plant species that naturally contain geraniol.

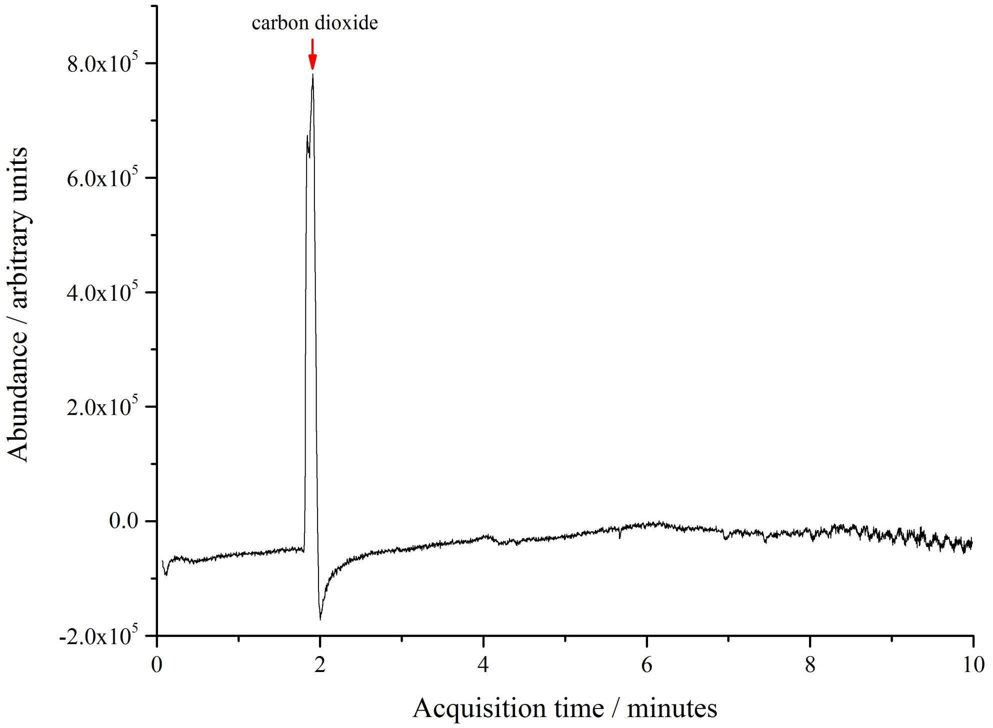

Figure 4.1: Base-line corrected total ion chromatogram of genetically modified *Nicotiana benthamiana* headspace. No VOCs were detected.

4.1.2 *Rosa* 'English Princess' Petals

The headspace measurements on *Rosa* 'English Princess' petals did not result in the detection of geraniol or any other volatiles, as seen in Figure 4.2. Geraniol,

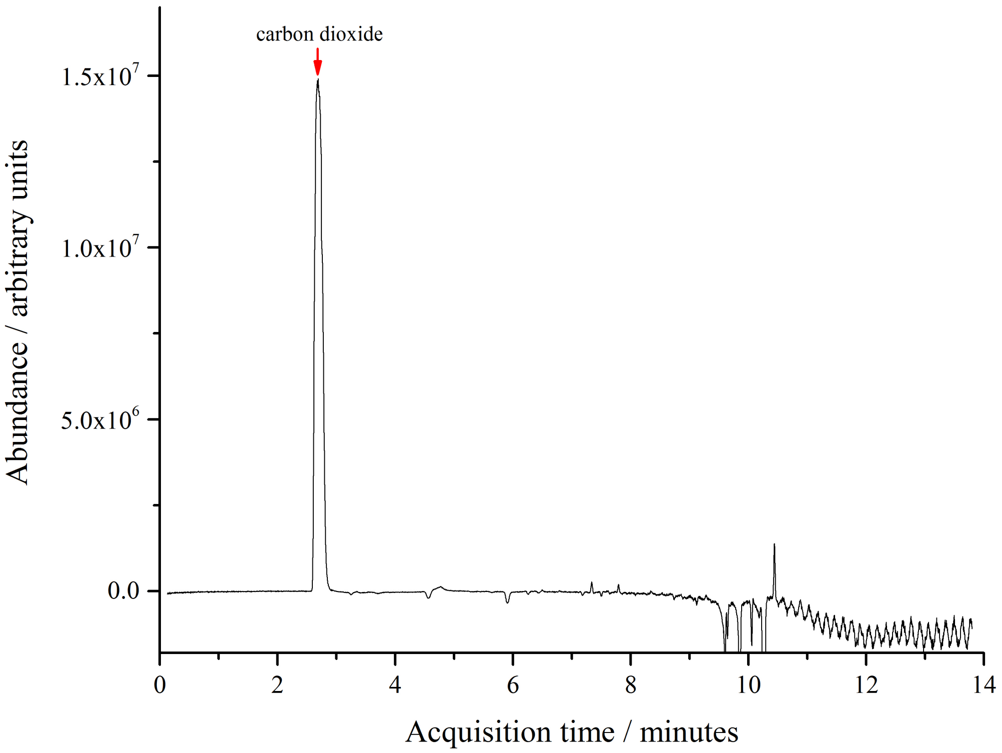

Figure 4.2: Baseline-corrected total ion chromatogram of *Rosa* ‘English Princess’ headspace. No VOCs were detected.

citronellol and nerol have been reported in the literature as among the main components in the headspace of *Rosa damascena Mill.* flowers [182]. However, these measurements involved either a 24-hour trapping of the headspace or the use of a Solid Phase Microextraction (SPME) fibre, a silica fibre coated with a thin layer of suitable polymeric sorbent or immobilised liquid that concentrates the analyte by means of adsorption [183]. It can therefore be concluded that direct headspace measurements are not sufficiently sensitive for the detection of VOCs in the headspace of these petals. Headspace trapping or concentration may be necessary for the detection of these compounds.

4.1.3 *Pelargonium* ‘Attar of Roses’ Leaves

Geraniol was not detected in the headspace of *Pelargonium* ‘Attar of Roses’ leaves, but unlike those on tobacco leaves and rose petals, these measurements did yield signals indicative of VOCs: for rose oxide at 7.569 min and l-menthone at 8.650 min,

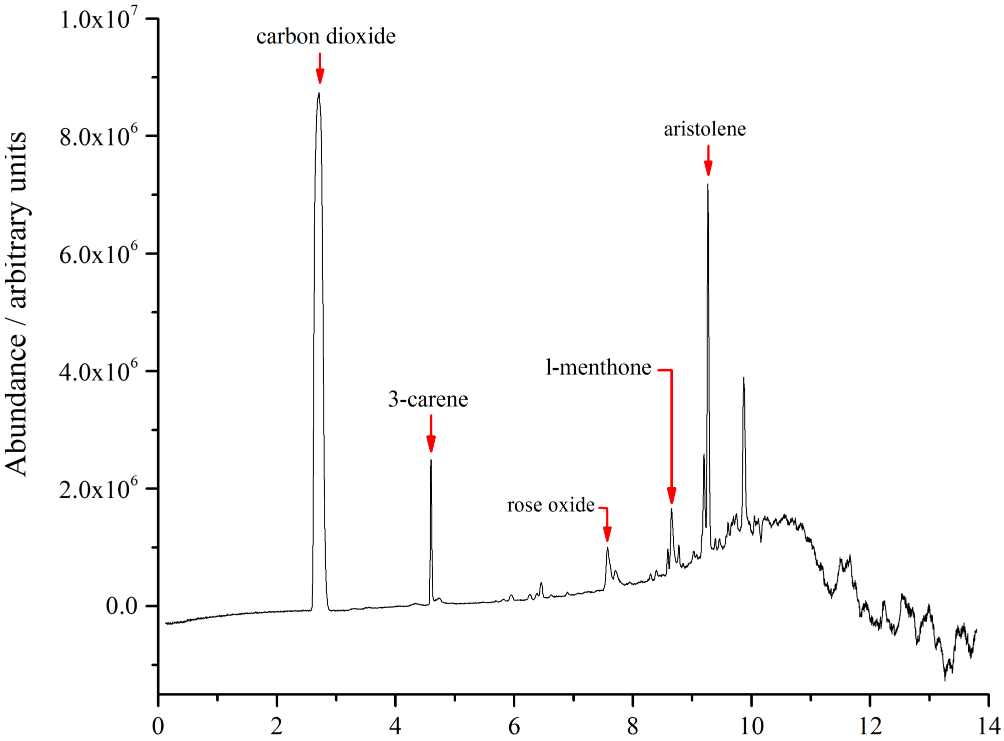

Figure 4.3: Baseline-corrected total ion chromatogram of *Pelargonium* 'Attar of Roses' headspace. Compounds that have previously been reported in *Pelargonium* 'Attar of Roses' or *Pelargonium graveolens* are labelled.

both of which are known to be present in *Pelargonium* 'Attar of Roses' [178]. 3-carene and aristolene were also detected, at 4.596 min and 9.264 min respectively. While these compounds were not reported in the literature, it must be noted that the published chemical composition is not complete and omits many unidentified sesquiterpenes [178], of which aristolene may be one. 3-carene and aristolene have been reported previously in *Pelargonium graveolens* leaves [184], [185]. These compounds are shown in the total ion chromatogram in Figure 4.3.

4.2 Discussion of Headspace Analyses

Considering the sensitivity of GC-MS techniques, one would expect to observe geraniol in the headspace of *Pelargonium* 'Attar of Roses' leaves which will later be shown in Section 4.4.3 to contain geraniol. Samples taken from the headspace in vials containing geraniol and containing pelargonium leaves spiked with geraniol showed a geraniol peak between 10.2 and 10.4 min. However, the headspace measurements involve a rising baseline which may have obscured the smaller geraniol peaks from plant tissues. The rising baseline could be due to delayed movement of some of the analyte from the liner into the column which, in turn, could be caused by analyte molecules sticking to the liner. Hydrogens of carboxylic, amino and alcohol functional groups are known to interact with a glass insert [186]. Interactions with the liner would be particularly strong if the liner is contaminated with molecules that have an affinity for the analyte molecules. The delay could also be due to the sample being injected too quickly or with excess volume such that analyte molecules get into the carrier gas line. For complex samples, these delayed peaks could merge together to result in a rising baseline. As to the limit of detection, with the current baseline and instrument settings, the concentration of geraniol in the pelargonium headspace would need to produce an abundance signal of 4.60×10^5 above the baseline to be detectable. This limit was calculated as three times the standard deviation of the baseline signal between 10.2 and 10.4 min.

4.3 Analyses on Geraniol Solutions

In order to quantify geraniol in plant tissue extracts, geraniol solutions of known concentrations were prepared in dichloromethane, and GC-MS measurements on these liquid samples were used to generate calibration curves. The data presented here will be used in the following section to quantify geraniol in *Pelargonium* 'Attar of Roses' leaf extracts. The measurements on the standard solutions also allowed the limit of detection of geraniol in dichloromethane with the current GC-MS instrument to be determined. The concentrations used and the abundance of geraniol detected can be seen in Table 4.1 and Figure 4.4. The abundance values represent the area under the relevant GC peak and were determined manually based on retention times and fragmentation patterns, and using the RTE integrator from the Agilent ChemStation software [187]. As seen in Figure 4.5, the seven data points with the lowest concentrations of geraniol were fit to a straight line using OriginPro's instrumental weighted fitting method, where the weight for each data point i is given

Table 4.1: Concentrations of geraniol solutions in dichloromethane and the corresponding abundance values detected by GC-MS.

Concentration / mM	Peak area	Peak area	Peak area
0.005	2672854	2640110	2528491
0.010	6634433	7117830	4579953
0.020	12377298	14255922	16213725
0.026	20743067	22380335	22812331
0.033	30496219	29628305	31217954
0.046	38981370	40710755	41401104
0.060	58151295	58337089	53740087
0.076	71939355	71499604	70903037
0.115	107935885	103037510	100979011
0.172	141550099	145309673	143864142
0.310	248342115	253794192	255713747
0.466	324887446	309628754	321083076
0.645	374894072	369493542	365055344
0.967	467354728	461573998	454551196
1.243	533192709	525005727	520441675
1.865	636597467	624790716	630837609
2.582	738220927	651010718	641987312
3.874	756192532	735415379	754285047
5.364	882685018	873263973	880057471
8.045	1047578682	1057917454	1089608299
12.068	1092027626	1052954062	1114736495
15.516	1342614704	1398958429	1461833682
19.949	1572796931	1702518604	1713728670
25.649	1802126643	1899501286	1944168676
32.978	2099384669	2111324152	2191865536
39.573	2038007069	2558976588	2460124858
47.488	2209183604	2554861564	2689718974
56.985	2744306854	2808361661	2875226852

by $w_i = \frac{1}{{\sigma_i}^2}$ with σ_i the standard deviation for the corresponding data point [188]. A linear equation relating the concentration of geraniol to the corresponding area of chromatogram peak was determined with a coefficient of determination value of 0.99772. The limit of detection was defined as the concentration of geraniol that produces a signal that is three times the standard deviation higher than the baseline signal. It was calculated as 2.6 μM, using three blank (dichloromethane) measurements prior to starting the GC-MS runs as well as two blank measurements within the set of concentrations used for the linear fit.

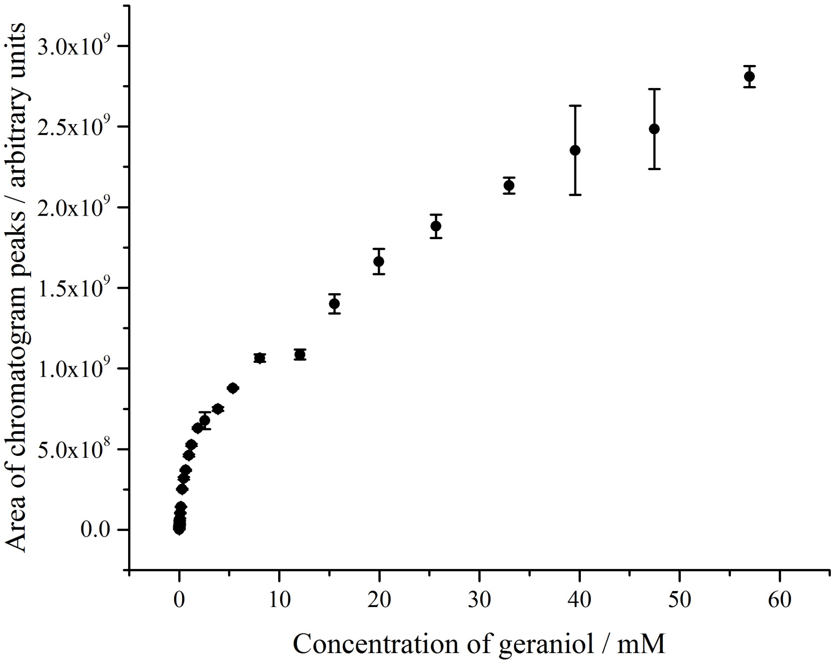

Figure 4.4: Abundance of geraniol detected by GC-MS for various concentrations of geraniol in dichloromethane. Abundance was given by the area under the geraniol peak in the total ion chromatogram. Error bars represent one standard deviation.

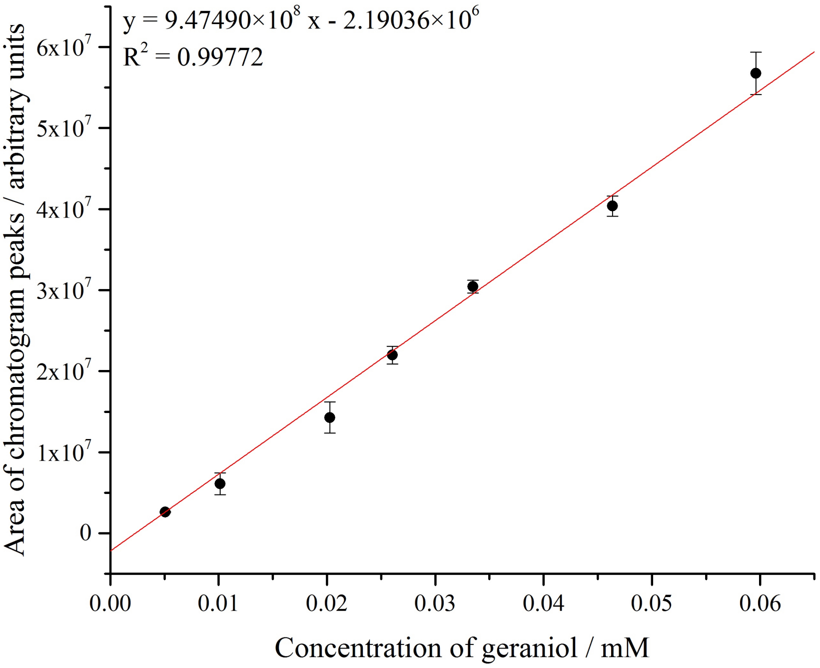

Figure 4.5: Concentration series for lower concentrations of geraniol solutions used, fit to a straight line. Error bars represent one standard deviation.

4.4 Liquid Extract Analyses

Since geraniol was not detected in the headspace analyses of GM *Nicotiana benthamiana* leaves, *Rosa*, 'English Princess' petals, or *Pelargonium* 'Attar of Roses' leaves, liquid extracts from these plant tissues were analysed with GC-MS for their geraniol content. 0.5 g of mature leaves or petals were frozen in liquid nitrogen immediately after collection, powdered, and extracted with dichloromethane. The method described by Dong et al. [67] was used or modified as specified below. For each sample, 1 μL of extract was injected into an Agilent 5975C GC/MSD instrument equipped with a Varian EZ GC–MS column. The oven temperature was held at 45 °C for 1 min, increased to 300 °C at a 10 °C min^{-1} rate, and held at 300 °C for 5 min.

4.4.1 Genetically modified *Nicotiana benthamiana* Leaves

Dong et al. reported that geraniol could not be detected in the liquid extracts of GM *Nicotiana benthamiana* leaves without a glycosidase treatment to release glycosylated geraniol [67]. A significant number of terpenoids have been reported to form glycosides, i.e. link to sugars through their active groups [189], [190]. Glycosylation often modifies the biological activities and pharmacokinetic properties of terpenoids [191]. We repeated the 'no glycosidase' measurements and were able to confirm that, even though several peaks were observed in the chromatogram in Figure 4.6, geraniol was not detected. These measurements suggest that a significant proportion of geraniol in GM *Nicotiana benthamiana* leaves might be in glycosylated form and undergo deglycosylation prior to emission into the atmosphere.

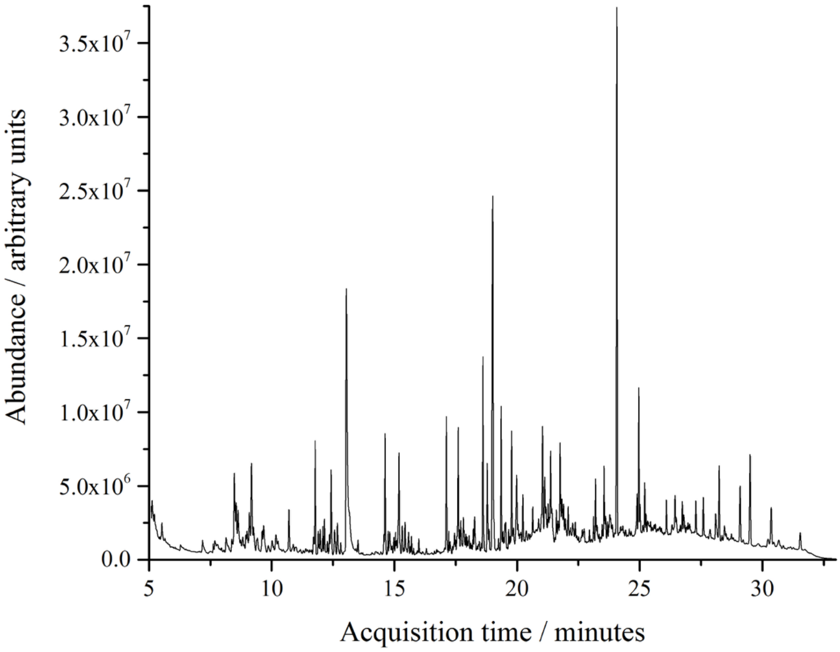

Figure 4.6: Total ion chromatogram of GM *Nicotiana benthamiana* leaf extracts. No geraniol was detected.

4.4.2 *Rosa* ‘English Princess’ Petals

To test whether the *Rosa* ‘English Princess’ petals contained geraniol, compounds from the petals were solvent-extracted and analysed by GC-MS. No geraniol was detected, so the method was modified to involve a single 3 mL extraction step and a sonication step prior to separating the liquid extracts from the crushed petals. The GC-MS measurements were repeated but no geraniol was detected with the modified extraction process. Citronellol and nerol which are widely known as among the main constituents of rose oil [192] were also not detected, even though neryl acetate, the acetate ester of nerol, was detected at 29.013 min. Detection of neryl acetate can be important in acid lime *Citrus aurantifolia* plants, since these plants show reduced neryl acetate content when infected by *Candidatus* Phytoplasma aurantifolia, a major cause of decline in the production of acid lime [193]. The lack of citronellol and geraniol peaks in the rose petal extract chromatogram might be due to variations in the volatile composition of *Rosa* ‘English Princess’ in comparison

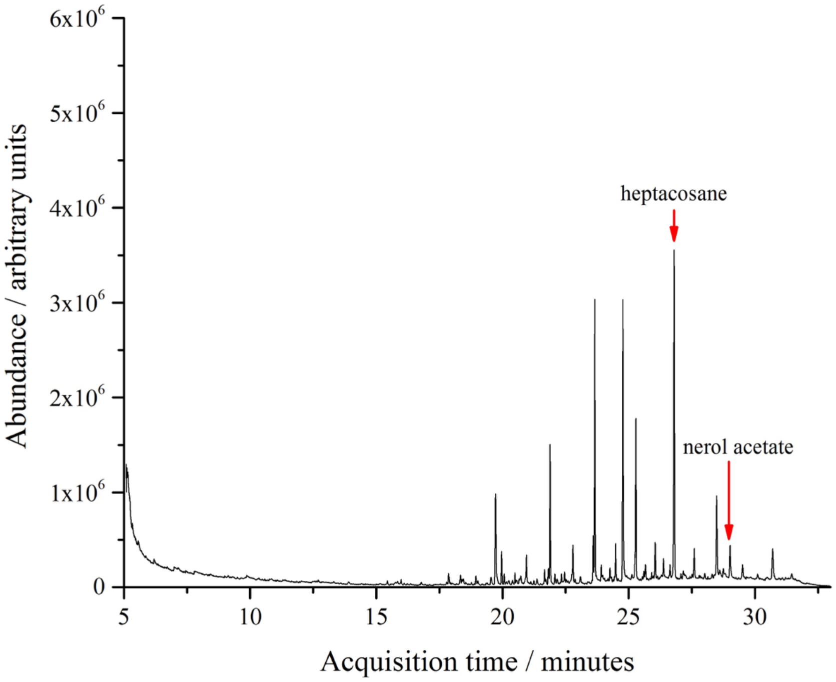

Figure 4.7: Total ion chromatogram of *Rosa* 'English Princess' petal extracts.

to other rose varieties, or the domination of extracted compounds by a high number and volume of long-chain hydrocarbons.

The major components of the extracts were determined to be long-chain hydrocarbons that are known to be present in *Rosa damascena Mill.* oil, including eicosane, heneicosane, tricosane [194], tetracosane, pentacosane, hexacosane, octacosane [195], heptacosane, heptadecane [196], and octadecane [195], [196]. Each of these compounds eluted at several different retention times, most likely because of the wide range of possible intermolecular and intramolecular interactions as well as the interactions with the column stationary phase. The presence of these abundant and widely distributed peaks could make it difficult to reliably detect smaller quantities of terpenoids such as geraniol. Long chain hydrocarbons are known to be found in the surface wax layer of leaves [197]. Hexacosane, pentacosane, tricosane, heneicosane, tetracosane have been shown to attract certain parasitoids [198], so monitoring the levels of these chemicals could be useful in biological pest control.

4.4.3 *Pelargonium* 'Attar of Roses' Leaves

The modified extraction method described in Section 4.4.2 was employed with a single 2 mL extraction. Geraniol was detected in *Pelargonium* 'Attar of Roses' leaf extracts at 12.837 min after injection. Using the equation in Figure 4.5, the concentration of geraniol was calculated as 8.2 μM. The pelargonium extract chromatogram is shown in Figure 4.8, and the associated mass spectrum in Figure 4.9. The estimated concentration can be seen together with the linear fit from the calibration in Figure 4.10.

Other compounds detected in the leaf extracts include l-menthone at 11.042 min, citronellol at 11.861 min, citronellyl formate at 12.449 min, and caryophyllene at 14.726 min, all of which are known to be found in *Pelargonium* 'Attar of Roses' [178]. Aristolene, which was detected in the headspace of the pelargonium leaf samples in Section 4.1.3, was also detected in the extracts, at 14.933 min. Compounds that were not previously reported in *Pelargonium* 'Attar of Roses', but were reported in other *Pelargonium* species and cultivars were also detected. τ-cadinol, reported in *Pelargonium graveolens* [184], [185] and *Pelargonium* cv. 'Bourbon' [199], was detected at 17.560 min. β-bourbonene, reported in both of these plants [185], [199] as well as in *Pelargonium crispum* [200], was detected at 14.213 min. Germacrene D, which was reported in *Pelargonium graveolens* [184], *Pelargonium filicifolium* [178], and *Pelargonium crispum* [200], was detected at 10.823 min, and carveol, which was reported in *Pelargonium capitatum*, *Pelargonium* cv. 'Rose' and *Pelargonium tomentosum*, was detected at 10.823 min. The only cosane detected in *Pelargonium* 'Attar of Roses' was heptacosane at 26.799 min.

Even though this thesis focuses on geraniol, all of the above compounds have roles in plant defence and response to stress, and their detection in plant tissues may have practical importance. For instance, grafting stress induces 3-carene in ponderosa pine (*Pinus ponderosa*) scions, which then declines over time [201]. Day-time emissions of β-bourbonene in silver birch (*Betula pendula*) and European aspen (*Populus tremula*) plants increase with elevated night-time temperatures [202]. European maize varieties attacked by Western corn rootworm (*Diabrotica virgifera virgifera*)

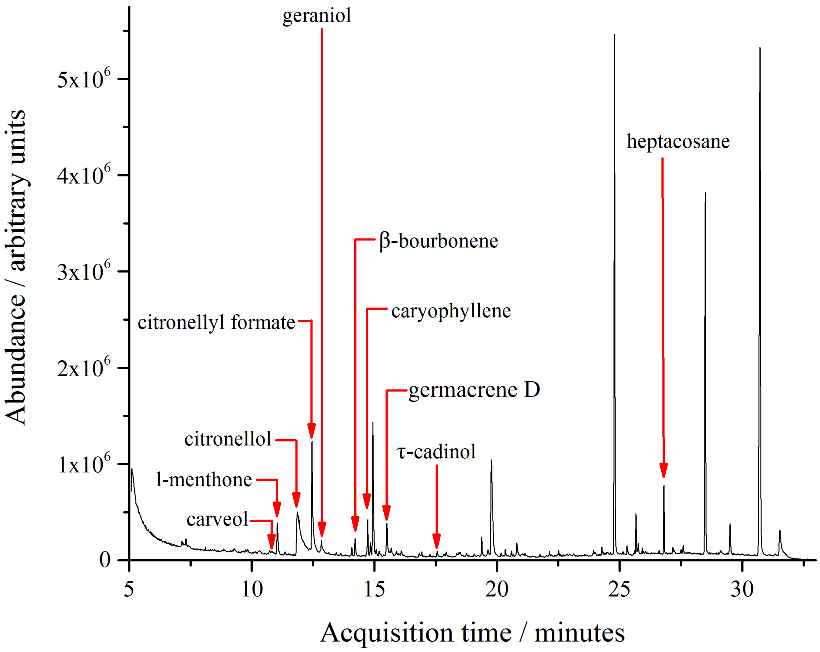

Figure 4.8: Total ion chromatogram of *Pelargonium* 'Attar of Roses' leaf extracts. Geraniol was detected at 12.837 min.

release caryophyllene which is attractive to entomopathogenic nematodes [203]. Weevil feeding on strawberry plants increases caryophyllene and germacrene D emissions [204]. Reduced irrigation of sweet basil (*Ocimum basilicum* L. 'Genovese') plants leads to higher levels of τ-cadinol [205]. High levels of sodium in the soil lower the concentration of citronellyl formate and increases that of geraniol in *Pelargonium graveolens* cv. 'Cimpawan' [206]. Elevated ultraviolet B radiation induces aristolene and caryophyllene in *Acorus calamus* L. [207], and increases heptacosane in the cuticular wax of cucumber plants [208]. In apple mint plants (*Mentha suaveolens*), salt stress increases the germacrene D content and reduces the l-menthone content [209]. Geraniol and citronellol can regulate defence-related gene expression in rough lemon [65]. Carveol, citronellol and geraniol exhibit activity against root-knot nematodes which cause significant losses in crop yield [210]. In spearmint, carveol is oxidised to carvone [211], the concentration of which increases significantly under water stress [212].

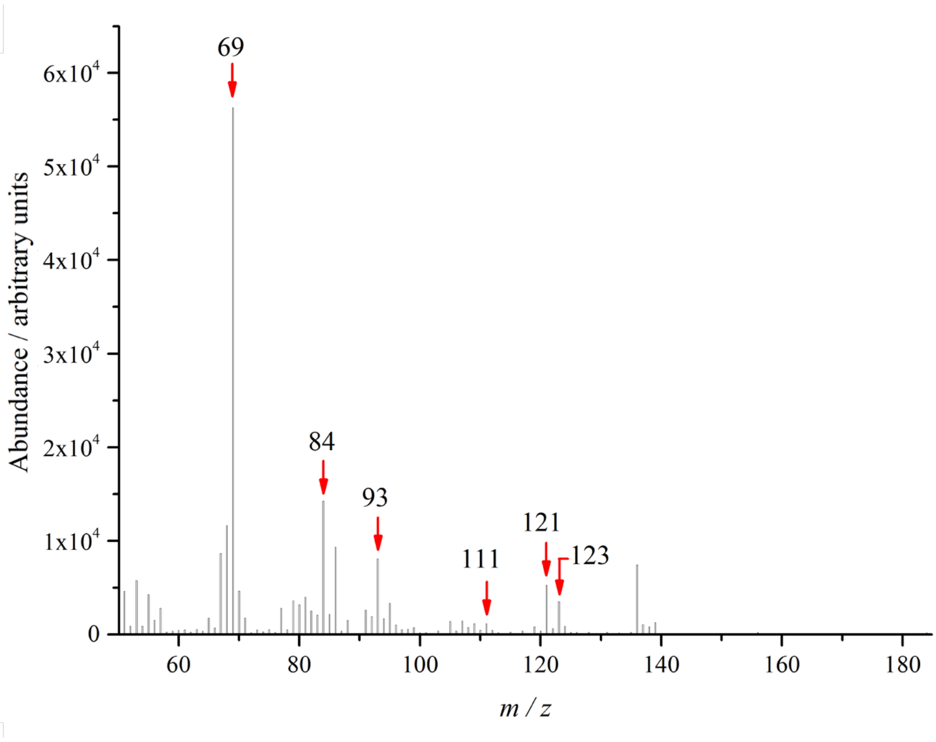

Figure 4.9: Extracted mass spectrum for geraniol detected in *Pelargonium* 'Attar of Roses' leaf extracts. Main fragment ions for geraniol have *m/z* of 69, 84, 93, 111, 121, and 123.

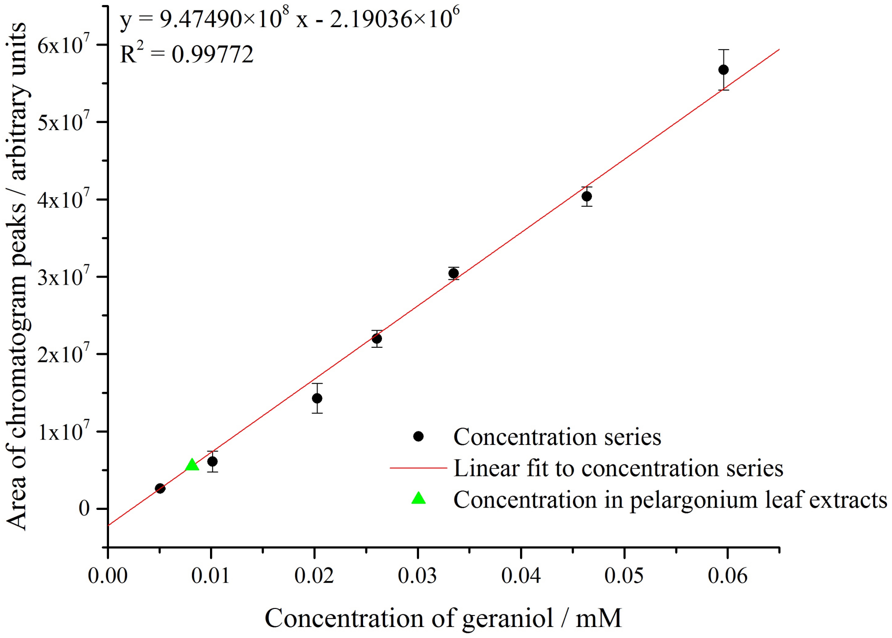

Figure 4.10: Concentration of geraniol in *Pelargonium* 'Attar of Roses' leaf extracts compared to the concentration series.

4.5 Estimations of Geraniol Gas in Plant Tissue Headspace

In order to assess the feasibility of using OF-CEAS to detect geraniol gas in the headspace of plants, estimated values of the expected geraniol concentration are needed. Below, these values are approximated for tobacco and pelargonium leaf tissues, employing a number of assumptions. A headspace volume of 20 mL, equal to the volume in which headspace GC-MS measurements were performed, is considered.

4.5.1 Genetically modified *Nicotiana benthamiana* Leaves

The concentration of geraniol gas in the headspace of the GM tobacco leaves could be estimated from the amount of geraniol detected by Dong et al. [67]. Since different leaves were shown to emit levels of geraniol varying between 5 and 55 ng g^{-1} h^{-1}, we could consider an average value of 30 ng g^{-1} h^{-1}. For 0.5 g of leaf, the emission rate would be 15 ng h^{-1}. Since geraniol has a molar mass of 154.25 g mol^{-1} [64], this rate is equivalent to 9.72×10^{-11} mol h^{-1}. According to Equation 2.1, the total number of gas molecules in a 20 mL vial used for the GC-MS experiments is 8.33×10^{-4} mol. Therefore, in a closed 20 mL of headspace with 0.5 g of leaf, the concentration of geraniol would increase by $\frac{9.72 \times 10^{-11} \quad \text{mol} \quad \text{h}^{-1}}{8.33 \times 10^{-4} \quad \text{mol}} \times 10^9 = 117$ ppb h^{-1} until the headspace reaches saturation or the geraniol stored in the leaf becomes depleted.

4.5.2 *Pelargonium* ‘Attar of Roses’ Leaves

The concentration of gaseous geraniol around plant tissue can be estimated from the concentration of geraniol detected in the plant tissue extracts, through some assumptions. Here, we assume gaseous geraniol in pelargonium headspace that is in equilibrium with dissolved geraniol. We employ Henry’s Law from Section 2.5 and model the pelargonium leaf tissue as liquid water, ignoring membranes and all other organic and inorganic constituents. The Henry’s law constant for geraniol is 5.89×10^{-5} atm m^3 mol^{-1} at 25 °C. The concentration of 8.2 μM of geraniol measured in 0.5 g pelargonium tissue is equivalent to a total of 1.64×10^{-8} moles. Water has a density of approximately 1 g mL^{-1}, so 0.5 g of water has a volume of 0.5 mL. Using Equation 2.62, the partial pressure of geraniol gas around the pelargonium tissue would be approximately 1930 ppb.

We could also consider pure geraniol, without water as a solvent. At equilibrium, the headspace would be saturated with geraniol, so the partial pressure of geraniol would be equal to its vapour pressure, which is 3.0×10^{-2} mm Hg at 25 °C [64]. From Equation 2.2, the molar density of geraniol in the headspace is 0.028 μM, which is equivalent to 670 ppb.

The estimations of geraniol in the headspace of *Pelargonium* ‘Attar of Roses’ leaves involve substantial approximations and provide only an upper limit to this value. The significance of the assumptions employed in these calculations is discussed in the next chapter.

5

Conclusions

We have examined the potential of OF-CEAS to detect VOCs as indicators of plant stress, coupling OF-CEAS measurements on pure geraniol samples with GC-MS measurements on plant samples for a case study on naturally occurring levels of geraniol. In Chapter 4, we analysed the geraniol content of genetically modified *Nicotiana benthamiana* leaves, *Rosa* ‘English Princess’ petals, and *Pelargonium* ‘Attar of Roses’ leaves. As a future step, it would be beneficial to repeat these measurements with a different liner or with slower rates and smaller volumes of injection to test whether these changes influence the detection of geraniol in the headspaces. We measured the concentration of geraniol in liquid extracts of *Pelargonium* ‘Attar of Roses’ leaves, and used this concentration to approximate the concentration of geraniol that may be found in the headspace of these leaves.

For a number of reasons, the calculated values of 670 ppb and 1930 ppb are overestimates for the concentration of geraniol in the headspace of 0.5 g of pelargonium leaf tissue. Around a plant, geraniol gas will not usually be in equilibrium with the geraniol in the leaf, as the gas will quickly disperse into the surroundings. In addition, a leaf has physical barriers and mechanisms that control VOC emission. Under natural circumstances, VOCs are released from plant leaves via two paths: exit through the stomata or diffusion through the leaf cuticle [213]. The cuticle acts as an efficient barrier for plant volatiles [214], so diffusion through the cuticle is often neglected [213]. It is hypothesised that the level of stomatal control on the emission of a VOC is related to its Henry’s Law constant, k. Gases of highly volatile compounds with high k values (10^3 Pa m^3 mol^{-1}) build up quickly in the leaf and overcome stomatal resistance. Compounds with lower k values

(10^{-1}–10^{2} Pa m^{3} mol^{-1}) have lower partial pressures in the leaf and are under stronger stomatal control, with the degree of control varying with k [214]. With a k of 5.96 Pa m^{3} mol^{-1}, geraniol would be under intermediate stomatal control.

While the calculated values of 670 ppb and 1930 ppb are upper limits for the concentration of geraniol in the headspace of the pelargonium leaves, they are respectively 4.6 and 13.1 times 147 ppb, the achieved limit of detection of geraniol with OF-CEAS established in Chapter 3. They are 26.2 and 75.7 times 25.5 ppb, the theoretically possible limit of detection calculated also in the same chapter. For GM tobacco plants synthesising geraniol, we calculated a 117 ppb h^{-1} increase in the concentration of geraniol emitted by 0.5 g of detached leaf tissue enclosed in a 20 mL headspace. Even though no geraniol was detected by direct headspace measurements on such samples after between 30 and 90 minutes of enclosure in a vial, a 25.5 ppb limit of detection by OF-CEAS suggests that geraniol could be detected from these samples after only 15 minutes of enclosure. Therefore, we speculate that OF-CEAS is likely to be sensitive enough to detect geraniol in the headspaces of *Pelargonium* 'Attar of Roses' and GM *Nicotiana benthamiana* leaves. Future directions should include the verification of these predictions with OF-CEAS measurements on the headspaces of these plant tissues, which we were not able to do due to time constraints and limited access to the OF-CEAS set up. Once geraniol or another VOC suitable for plant stress diagnosis has been sensitively detected in the headspace of these tissues using the relevant optical method, steps should be taken to modify the sensing technique to match the requirements in the field. In such an environment, complex mixtures of VOCs and high levels of humidity are expected. If a single diagnostic absorption line cannot be used for a given VOC, broadband spectroscopy could be used, but this approach would be expensive and difficult to achieve in a field setting. It would be more practical to measure absorption at several distinct wavelengths to quantify the level of the VOC. If these wavelengths overlap with the absorption features of water, mechanisms should be employed to remove humidity from the sample prior to measurements.

During this work, we have also explored a variety of additional questions. In Chapter 4, we investigated the chemical composition of GM *Nicotiana benthamiana* leaves, *Rosa* ‘English Princess’ petals, and *Pelargonium* ‘Attar of Roses’ leaves through headspace and liquid extract GC-MS measurements. We detected no VOCs in the headspaces of the tobacco leaves and the rose petals, and we detected only a few VOCs in the headspace of pelargonium leaves, suggesting that headspace trapping or analyte pre-concentration may be necessary to detect these compounds by GC-MS. In liquid extracts of these tissues, we detected a number of compounds the monitoring of which, by GC-MS or any other analytical technique, may have practical importance for the detection of stress in various plants. We established a detection limit of about 2.6 μM for geraniol in dichloromethane solution. For future concentration calibrations, internal standards should be used for more accurate GC-MS analyses. Internal standards of methyl trans-cinnamate [215], linalool [216], diphenyl-methane, butyl benzoate, eugenol, n-dodecanol [217], and [$^2H_7$]-geraniol, geraniol containing seven deuterium atoms [218], have been successfully used in geraniol quantification. If the quantification is to be performed on plant material rather than geraniol solutions, extra care must be taken to ensure that the internal standard is not naturally found in the plant and has no overlapping chromatographic peaks with the sample. Inclusion of more solutions in the lower concentration range in the calibration would also increase the quality of the analysis.

To conclude, optical methods appear promising for the sensitive detection and quantification of plant volatiles. These methods merit further investigation given their potential to non-destructively detect plant stress in field settings and on a real-time basis, improving crop yields and agricultural sustainability.

References

[1] F. M. Afendi, T. Okada, M. Yamazaki, A. Hirai-Morita, Y. Nakamura, K. Nakamura, S. Ikeda, H. Takahashi, M. Altaf-Ul-Amin, L. K. Darusman, K. Saito, and S. Kanaya. “KNApSAcK Family Databases: Integrated Metabolite–Plant Species Databases for Multifaceted Plant Research”. In: *Plant and Cell Physiology* 53.2 (2012), pp. 1–12.

[2] R. A. Dixon. “Natural products and plant disease resistance”. In: *Nature* 411.6839 (2001), pp. 843–847.

[3] M. Dicke and F. Loreto. “Induced plant volatiles: from genes to climate change”. In: *Trends in Plant Science* 15.3 (2010), pp. 115–117.

[4] J. T. Knudsen, R. Eriksson, J. Gershenzon, and B. Ståhl. “Diversity and distribution of floral scent”. In: *The Botanical Review* 72.1 (2006), pp. 1–120.

[5] D. Materić, D. Bruhn, C. Turner, G. Morgan, N. Mason, and V. Gauci. “Methods in plant foliar volatile organic compounds research”. In: *Applications in Plant Sciences* 3.12 (2015), p. 1500044.

[6] M. E. Maffei. “Sites of synthesis, biochemistry and functional role of plant volatiles”. In: *South African Journal of Botany* 76.4 (2010), pp. 612–631.

[7] J. Allen. *Chemistry in the Sunlight.* 2002. URL: `http://earthobservatory.nasa.gov/Features/ChemistrySunlight/`.

[8] M. O. Omolo, D. Okinyo, I. O. Ndiege, W. Lwande, and A. Hassanali. “Repellency of essential oils of some Kenyan plants against Anopheles gambiae”. In: *Phytochemistry* 65.20 (2004), pp. 2797–2802.

[9] G. C. Müller, A. Junnila, J. Butler, V. D. Kravchenko, E. E. Revay, R. W. Weiss, and Y. Schlein. “Efficacy of the botanical repellents geraniol, linalool, and citronella against mosquitoes.” In: *Journal of Vector Ecology* 34.1 (2009), pp. 2–8.

[10] R. Boch and D. A. Shearer. “Identification of Geraniol as the Active Component in the Nassanoff Pheromone of the Honey Bee”. In: *Nature* 194.4829 (1962), pp. 704–706.

[11] Food and Agriculture Organization of the United Nations. *The State of Food Insecurity in the World 2001.* 2001. URL: `http://www.fao.org/docrep/003/y1500e/y1500e00.htm`.

[12] Food and Agriculture Organization of the United Nations. *Global agriculture towards 2050.* URL: `http://www.fao.org/fileadmin/templates/wsfs/docs/Issues_papers/HLEF2050_Global_Agriculture.pdf`.

[13] J. Schmidhuber and F. N. Tubiello. “Global food security under climate change.” In: *Proceedings of the National Academy of Sciences of the United States of America* 104.50 (2007), pp. 19703–8.

[14] D. B. Lobell, W. Schlenker, and J. Costa-Roberts. “Climate Trends and Global Crop Production Since 1980”. In: *Science* 333.6042 (2011), pp. 616–620.

[15] Intergovernmental Panel on Climate Change. *Managing the Risks of Extreme Events and Disasters to Advance Climate Change Adaptation.* 2012. URL: `https://www.ipcc.ch/pdf/special-reports/srex/SREX_Full_Report.pdf`.

[16] R. Chaplin-Kramer, R. P. Sharp, L. Mandle, S. Sim, J. Johnson, I. Butnar, L. Milà i Canals, B. A. Eichelberger, I. Ramler, C. Mueller, N. McLachlan, A. Yousefi, H. King, and P. M. Kareiva. "Spatial patterns of agricultural expansion determine impacts on biodiversity and carbon storage". In: *Proceedings of the National Academy of Sciences* 112.24 (2015), pp. 7402–7407.

[17] V. Smil. "Phosphorus in the environment: Natural flows and human interferences". In: *Annual Review of Energy and the Environment* 25 (2000), pp. 53–88.

[18] International Fertilizer Industry Association, United Nations Environment Programme. *The Fertilizer Industry, World Food Supplies and the Environment.* 1998.

[19] S. J. VanKauwenbergh. *Cadmium and Other Minor Elements in World Resources of Phosphate Rock.* Proceedings. International Fertiliser Society, 1997.

[20] M. W. Aktar, D. Sengupta, and A. Chowdhury. "Impact of pesticides use in agriculture: their benefits and hazards". In: *Interdisciplinary Toxicology* 2.1 (2009), pp. 1–12.

[21] J. Jeyaratnam. "Acute pesticide poisoning: a major global health problem". In: *World Health Statistics Quarterly* 43.3 (1990), pp. 139–144.

[22] PAN International. *Over 100 International Health Experts and Toxicologists Call for an End to the Use of Highly Hazardous Pesticides.* URL: `http://pan-international.org/release/over-100-international-health-experts-and-toxicologists-call-for-an-end-to-the-use-of-highly-hazardous-pesticides/`.

[23] International Water Management Institute. *A Comprehensive Assessment of Water Management in Agriculture.* 2007. URL: `http://www.iwmi.cgiar.org/assessment/files_new/synthesis/Summary_SynthesisBook.pdf`.

[24] Food and Agriculture Organization of the United Nations. *Coping with water scarcity - Challenge of the twenty-first century.* 2007. URL: `http://www.fao.org/3/a-aq444e.pdf`.

[25] Food and Agriculture Organization of the United Nations. *AQUASTAT website.* 2016. URL: `http://www.fao.org/nr/water/aquastat/water_use/index.stm`.

[26] UNESCO. *WWDR4 – Background Information Brief: Global water resources under increasing pressure from rapidly growing demands and climate change, according to new UN World Water Development Report.* URL: `http://www.unesco.org/new/fileadmin/MULTIMEDIA/HQ/SC/pdf/WWDR4%20Background%20Briefing%20Note_ENG.pdf`.

[27] European Parliament, Council of the European Union. *Document 32004L0042: Directive 2004/42/CE of the European Parliament and of the Council of 21 April 2004 on the limitation of emissions of volatile organic compounds due to the use of organic solvents in certain paints and varnishes and vehicle refinishing products and amending Directive 1999/13/EC.* 2004. URL: `http://eur-lex.europa.eu/legal-content/EN/TXT/?uri=CELEX:32004L0042`.

[28] A. Herrmann. *The Chemistry and Biology of Volatiles*. Wiley, 2011.

[29] A. B. Guenther, X. Jiang, C. L. Heald, T. Sakulyanontvittaya, T. Duhl, L. K. Emmons, and X. Wang. “The Model of Emissions of Gases and Aerosols from Nature version 2.1 (MEGAN2.1): an extended and updated framework for modeling biogenic emissions”. In: *Geoscientific Model Development* 5.6 (2012), pp. 1471–1492.

[30] R. Grote, R. K. Monson, and Ü. Niinemets. “Leaf-Level Models of Constitutive and Stress-Driven Volatile Organic Compound Emissions”. In: *Biology, Controls and Models of Tree Volatile Organic Compound Emissions*. Dordrecht: Springer Netherlands, 2013, pp. 315–355.

[31] H. B. Jakobsen and C. E. Olsen. “Influence of climatic factors on emission of flower volatiles in situ”. In: *Planta* 192.3 (1994), pp. 365–371.

[32] P. W. Pare and J. H. Tumlinson. “Induced synthesis of plant volatiles”. In: *Nature* 385.6611 (1997), pp. 30–31.

[33] L. Copolovici, A. Kännaste, L. Pazouki, and Ü. Niinemets. “Emissions of green leaf volatiles and terpenoids from Solanum lycopersicum are quantitatively related to the severity of cold and heat shock treatments”. In: *Journal of Plant Physiology* 169.7 (2012), pp. 664–672.

[34] C. E. M. Van Den Boom, T. A. Van Beek, M. A. Posthumus, A. De Groot, and M. Dicke. “Qualitative and Quantitative Variation Among Volatile Profiles Induced by *Tetranychus urticae* Feeding on Plants from Various Families”. In: *Journal of Chemical Ecology* 30.1 (2004), pp. 69–89.

[35] I. T. Baldwin. “Plant volatiles”. In: *Current Biology* 20.9 (2010), R392–R397.

[36] M. Wink. *Biochemistry of Plant Secondary Metabolism*. Annual Plant Reviews. Wiley, 2011.

[37] M. Heil and J. C. Silva Bueno. “Within-plant signaling by volatiles leads to induction and priming of an indirect plant defense in nature.” In: *Proceedings of the National Academy of Sciences of the United States of America* 104.13 (2007), pp. 5467–5472.

[38] Y. Choh, S. Kugimiya, and J. Takabayashi. “Induced production of extrafloral nectar in intact lima bean plants in response to volatiles from spider mite-infested conspecific plants as a possible indirect defense against spider mites”. In: *Oecologia* 147.3 (2006), pp. 455–460.

[39] R. Karban, I. T. Baldwin, K. J. Baxter, G. Laue, and G. W. Felton. “Communication between plants: induced resistance in wild tobacco plants following clipping of neighboring sagebrush”. In: *Oecologia* 125.1 (2000), pp. 66–71.

[40] F. Spinelli, A. Cellini, C. Piovene, K. Nagesh, and L. Marchetti. *Emission and Function of Volatile Organic Compounds in Response to Abiotic Stress*. INTECH Open Access Publisher, 2011.

[41] A. Calogirou, B. R. Larsen, and D. Kotzias. “Gas-phase terpene oxidation products: A review”. In: *Atmospheric Environment* 33.9 (1999), pp. 1423–1439.

[42] C. Langebartels, K. Kerner, S. Leonardi, M. Schraudner, M. Trost, W. Heller, and H. Sandermann. “Biochemical Plant Responses to Ozone : I. Differential Induction of Polyamine and Ethylene Biosynthesis in Tobacco”. In: *Plant Physiology* 95.3 (1991), pp. 882–889.

[43] A. C. Heiden, T. Hoffmann, J. Kahl, D. Kley, D. Klockow, C. Langebartels, H. Mehlhorn, H. Sandermann, Jr., M. Schraudner, G. Schuh, and J. Wildt. “Emission of Volatile Organic Compounds From Ozone-Exposed Plants”. In: *Ecological Applications* 9.4 (1999), pp. 1160–1167.

[44] T. D. Sharkey and E. L. Singsaas. “Why plants emit isoprene”. In: *Nature* 374.6525 (1995), pp. 769–769.

[45] C. Jun-wen and C. Kun-fang. “Plant VOCs emission: a new strategy of thermotolerance”. In: *Journal of Forestry Research* 16.4 (2005), pp. 323–326.

[46] F. Loreto, C. Barta, F. Brilli, and I. Nogues. “On the induction of volatile organic compound emissions by plants as consequence of wounding or fluctuations of light and temperature”. In: *Plant, Cell & Environment* 29.9 (2006), pp. 1820–1828.

[47] V. Velikova and F. Loreto. “On the relationship between isoprene emission and thermotolerance in *Phragmites australis* leaves exposed to high temperatures and during the recovery from a heat stress”. In: *Plant Cell and Environment* 28.3 (2005), pp. 318–327.

[48] K. Sasaki, T. Saito, M. Lämsä, K. Oksman-Caldentey, M. Suzuki, K. Ohyama, T. Muranaka, K. Ohara, and K. Yazaki. “Plants Utilize Isoprene Emission as a Thermotolerance Mechanism”. In: *Plant and Cell Physiology* 48.9 (2007), pp. 1254–1262.

[49] B. Lugtenberg and F. Kamilova. “Plant-Growth-Promoting Rhizobacteria”. In: *Annual Review of Microbiology* 63.1 (2009), pp. 541–556.

[50] R. Marasco, E. Rolli, G. Vigani, S. Borin, C. Sorlini, H. Ouzari, G. Zocchi, and D. Daffonchio. “Are drought-resistance promoting bacteria cross-compatible with different plant models?” In: *Plant Signaling & Behavior* 8.10 (2013), e26741.

[51] S. Timmusk, I. A. Abd El-Daim, L. Copolovici, T. Tanilas, A. Kännaste, L. Behers, E. Nevo, G. Seisenbaeva, E. Stenström, and Ü. Niinemets. “Drought-Tolerance of Wheat Improved by Rhizosphere Bacteria from Harsh Environments: Enhanced Biomass Production and Reduced Emissions of Stress Volatiles”. In: *PLoS ONE* 9.5 (2014), e96086.

[52] M. Staudt and G. Seufert. “Light-dependent emission of monoterpenes by holm oak (*Quercus ilex* L.)” In: *Naturwissenschaften* 82.2 (1995), pp. 89–92.

[53] M. Staudt, S. Rambal, R. Joffre, and J. Kesselmeier. “Impact of drought on seasonal monoterpene emissions from *Quercus ilex* in southern France”. In: *Journal of Geophysical Research: Atmospheres* 107.21 (2002), pp. 1–9.

[54] G. Schuh, A. C. Heiden, T. Hoffmann, J. Kahl, P. Rockel, J. Rudolph, and J. Wildt. “Emissions of Volatile Organic Compounds from Sunflower and Beech: Dependence on Temperature and Light Intensity”. In: *Journal of Atmospheric Chemistry* 27.3 (1997), pp. 291–318.

[55] A. Vallat, H. Gu, and S. Dorn. “How rainfall, relative humidity and temperature influence volatile emissions from apple trees in situ”. In: *Phytochemistry* 66.13 (2005), pp. 1540–1550.

[56] C. Balconi, P. Stevanato, M. Motto, and E. Biancardi. “Breeding for Biotic Stress Resistance/Tolerance in Plants”. In: *Crop Production for Agricultural Improvement*. Springer Netherlands, 2012, pp. 57–114.

[57] P. M. Bleeker, P. J. Diergaarde, K. Ament, J. Guerra, M. Weidner, S. Schutz, M. T. De Both, M. A. Haring, and R. C. Schuurink. “The Role of Specific Tomato Volatiles in Tomato-Whitefly Interaction”. In: *Plant Physiology* 151.2 (2009), pp. 925–935.

[58] C. M. De Moraes, M. C. Mescher, and J. H. Tumlinson. “Caterpillar-induced nocturnal plant volatiles repel conspecific females.” In: *Nature* 410.6828 (2001), pp. 577–580.

[59] J. Pettersson, J. A. Pickett, B. J. Pye, A. Quiroz, L. E. Smart, L. J. Wadhams, and C. M. Woodcock. “Winter host component reduces colonization by bird-cherry-oat aphid, *Rhopalosiphum padi* (L.) (homoptera, aphididae), and other aphids in cereal fields”. In: *Journal of Chemical Ecology* 20.10 (1987), pp. 2565–2574.

[60] M. Dicke, T. A. Van Beek, M. A. Posthumus, N. Ben Dom, H. Van Bokhoven, and A. De Groot. “Isolation and identification of volatile kairomone that affects acarine predator-prey interactions”. In: *Journal of Chemical Ecology* 16.2 (1990), pp. 381–396.

[61] C. M. De Moraes, W. J. Lewis, P. W. Paré, H. T. Alborn, J. H. Tumlonson, and P. W. Pare. “Herbivore-infested plants selectively attract parasitoids”. In: *Nature* 393 (1998), pp. 570–573.

[62] M. Hilker and T. Meiners. “Early herbivore alert: Insect eggs induce plant defense”. In: *Journal of Chemical Ecology* 32.7 (2006), pp. 1379–1397.

[63] H. Surburg and J. Panten. *Common Fragrance and Flavor Materials*. Wiley-VCH, 2006, p. 28.

[64] ChemSpider, Royal Society of Chemistry. *CSID:13849989*. URL: `http://www.chemspider.com/Chemical-Structure.13849989.html`.

[65] Y. Yamasaki, H. Kunoh, H. Yamamoto, and K. Akimitsu. “Biological roles of monoterpene volatiles derived from rough lemon (*Citrus jambhiri* Lush) in citrus defense”. In: *Journal of General Plant Pathology* 73.3 (2007), pp. 168–179.

[66] Y. Ashida, M. Nishimoto, A. Matsushima, J. Watanabe, and T. Hirata. “Molecular Cloning and mRNA Expression of Geraniol-inducible Genes in Cultured Shoot Primordia of *Matricaria chamomilla*”. In: *Bioscience, Biotechnology, and Biochemistry* 66.11 (2002), pp. 2511–2514.

[67] L. Dong, K. Miettinen, M. Goedbloed, F. W. A. Verstappen, A. Voster, M. A. Jongsma, J. Memelink, S. Van Der Krol, and H. J. Bouwmeester. “Characterization of two geraniol synthases from *Valeriana officinalis* and *Lippia dulcis*: Similar activity but difference in subcellular localization”. In: *Metabolic Engineering* 20 (2013), pp. 198–211.

[68] M. F. Clark and A. N. Adams. “Characteristics of the Microplate Method of Enzyme-Linked Immunosorbent Assay for the Detection of Plant Viruses”. In: *Journal of General Virology* 34.3 (1977), pp. 475–483.

[69] K. Mullis, H. Erlich, N. Arnheim, G. Horn, R. Saiki, and S. Scharf. *Process for amplifying, detecting, and/or-cloning nucleic acid sequences.* US Patent 4,683,195. July 1987. URL: `http://www.google.co.uk/patents/US4683195`.

[70] N. A. L. Garibyan. “Research Techniques Made Simple : Polymerase Chain Reaction (PCR)”. In: *NIH Public Access* 133.3 (2014), pp. 1–8.

[71] N. W. Schaad and R. D. Frederick. “Real-time PCR and its application for rapid plant disease diagnostics”. In: *Canadian Journal of Plant Pathology* 24.3 (2002), pp. 250–258.

[72] J. Giraudat. “Imaging techniques and the early detection of plant stress”. In: *Trends in Plant Science* 5.11 (2000), pp. 495–501.

[73] E. Oerke and U. Steiner. “Potential of Digital Thermography for Disease Control”. In: *Precision Crop Protection - the Challenge and Use of Heterogeneity.* Springer Netherlands, 2010, pp. 167–182.

[74] H. Nilsson. “Remote Sensing and Image Analysis in Plant Pathology”. In: *Annual Review of Phytopathology* 15 (1995), pp. 489–527.

[75] H. G. Jones. “Use of infrared thermography for monitoring stomatal closure in the field: application to grapevine”. In: *Journal of Experimental Botany* 53.378 (2002), pp. 2249–2260.

[76] K. Bürling, M. Hunsche, and G. Noga. “Use of blue-green and chlorophyll fluorescence measurements for differentiation between nitrogen deficiency and pathogen infection in winter wheat”. In: *Journal of Plant Physiology* 168.14 (2011), pp. 1641–1648.

[77] S. Ciompi, E. Gentili, L. Guidi, and G. F. Soldatini. “The effect of nitrogen deficiency on leaf gas exchange and chlorophyll fluorescence parameters in sunflower”. In: *Plant Science* 118.2 (1996), pp. 177–184.

[78] J. Kuckenberg, I. Tartachnyk, and G. Noga. “Temporal and spatial changes of chlorophyll fluorescence as a basis for early and precise detection of leaf rust and powdery mildew infections in wheat leaves”. In: *Precision Agriculture* 10.1 (2009), pp. 34–44.

[79] L. Chaerle, S. Lenk, I. Leinonen, H. G. Jones, D. Van Der Straeten, and C. Buschmann. “Multi-sensor plant imaging: Towards the development of a stress-catalogue”. In: *Biotechnology Journal* 4.8 (2009), pp. 1152–1167.

[80] N. Chaffey. *Wood Formation in Trees: Cell and Molecular Biology Techniques.* CRC Press, 2003.

[81] A. D. Meigs, L. J. Otten, and T. Y. Cherezova. “Ultraspectral imaging: A new contribution to global virtual presence”. In: *IEEE Aerospace and Electronic Systems Magazine* 23.10 (2008), pp. 11–17.

[82] C. Zhang and J. M. Kovacs. “The application of small unmanned aerial systems for precision agriculture: A review”. In: *Precision Agriculture* 13.6 (2012), pp. 693–712.

[83] A. K. Mahlein, E. C. Oerke, U. Steiner, and H. W. Dehne. “Recent advances in sensing plant diseases for precision crop protection”. In: *European Journal of Plant Pathology* 133.1 (2012), pp. 197–209.

[84] P. J. Hardin and T. J. Hardin. “Small-Scale Remotely Piloted Vehicles in Environmental Research”. In: *Geography Compass* 4.9 (2010), pp. 1297–1311.

[85] J. S. West, C. Bravo, R. Oberti, D. Lemaire, D. Moshou, and H. A. McCartney. “The Potential of Optical Canopy Measurement for Targeted Control of Field Group Diseases”. In: *Annual Review of Phytopathology* 41.1 (2003), pp. 593–614.

[86] S. Sankaran, A. Mishra, R. Ehsani, and C. Davis. “A review of advanced techniques for detecting plant diseases”. In: *Computers and Electronics in Agriculture* 72.1 (2010), pp. 1–13.

[87] J. Laothawornkitkul, J. P. Moore, J. E. Taylor, M. Possell, T. D. Gibson, C. N. Hewitt, and N. D. Paul. “Discrimination of plant volatile signatures by an electronic nose: A potential technology for plant pest and disease monitoring”. In: *Environmental Science and Technology* 42.22 (2008), pp. 8433–8439.

[88] F. Spinelli, M. Noferini, and G. Costa. “Near Infrared Spectroscopy (NIRS): Perspective of Fire Blight Detection in Asymptomatic Plant Material”. In: *ISHS Acta Horticulturae 704: X International Workshop on Fire Blight*. 2006.

[89] M. Markom, A. M. Shakaff, A. Adom, M. Ahmad, W. Hidayat, A. Abdullah, and N. A. Fikri. “Intelligent electronic nose system for basal stem rot disease detection”. In: *Computers and Electronics in Agriculture* 66.2 (2009), pp. 140–146.

[90] F. Rock, N. Barsan, and U. Weimar. “Electronic nose: Current status and future trends”. In: *Chemical Reviews* 108.2 (2008), pp. 705–725.

[91] J. Gardner and P. Bartlett. *Electronic Noses: Principles and Applications*. Oxford University Press, 1999.

[92] I. Gaillard, S. Rouquier, and D. Giorgi. “Olfactory receptors”. In: *Cellular and Molecular Life Sciences* 61.4 (2004), pp. 456–469.

[93] A. D. Wilson. “Diverse Applications of Electronic-Nose Technologies in Agriculture and Forestry”. In: *Sensors* 13.2 (2013), pp. 2295–2348.

[94] A. Wilson and M. Baietto. “Applications and Advances in Electronic-Nose Technologies.” In: *Sensors* 9.7 (2009), pp. 5099–5148.

[95] K. Arshak, E. Moore, G. Lyons, J. Harris, and S. Clifford. “A Review of Gas Sensors Employed in Electronic Nose Applications”. In: *Sensor Review* 24.2 (2004), pp. 181–198.

[96] D. Tholl, W. Boland, A. Hansel, F. Loreto, U. S. R. Röse, and J. P. Schnitzler. “Practical approaches to plant volatile analysis”. In: *Plant Journal* 45.4 (2006), pp. 540–560.

[97] M. Poliak, A. Gordin, and A. Amirav. “Open Probe: A Device for Ultra Fast Electron Ionization Mass Spectrometry Analysis”. In: 82.13 (2010), pp. 7826–7831.

[98] A. Amirav, U. Keshet, T. Alon, and A. B. Fialkov. “Open Probe fast GC-MS–Real time analysis with separation”. In: *International Journal of Mass Spectrometry* 371 (2014), pp. 47–53.

[99] PerkinElmer, Inc. *Torion T-9 GC/MS*. URL: `http://torion.com/fileadmin/media/documents/brochures/TorionT-9_GCMS_Product_Note.pdf`.

[100] Bruker. *E2M*. URL: `https://www.bruker.com/fileadmin/user_upload/8-PDF-Docs/CBRNE_Detection/Literature/E2M_2012_eng_eBook.pdf`.

[101] FLIR Systems, Inc. *Griffin 460*. URL: `http://www.flir.com/threatdetection/display/?id=63281`.

[102] A. Ellis and C. Mayhew. *Proton Transfer Reaction Mass Spectrometry: Principles and Applications*. Wiley, 2013.

[103] S. Allmann and I. T. Baldwin. "Insects Betray Themselves in Nature to Predators by Rapid Isomerization of Green Leaf Volatiles". In: *Science* 329.5995 (2010), pp. 1075–1078.

[104] C. Warneke, C. V. D. Veen, S. Luxembourg, J. de Gouw, and A. Kok. "Measurements of benzene and toluene in ambient air using proton-transfer-reaction mass spectrometry: calibration, humidity dependence, and field intercomparison". In: *International Journal of Mass Spectrometry* 207.3 (2001), pp. 167–182.

[105] A. Tani, S. Hayward, A. Hansel, and C. N. Hewitt. "Effect of water vapour pressure on monoterpene measurements using proton transfer reaction-mass spectrometry (PTR-MS)". In: *International Journal of Mass Spectrometry* 239.2–3 (2004), pp. 161–169.

[106] S. Welzel, G. Lombardi, P. B. Davies, R. Engeln, D. C. Schram, and J. Röpcke. "Trace gas measurements using optically resonant cavities and quantum cascade lasers operating at room temperature". In: *Journal of Applied Physics* 104.9 (2008), p. 093115.

[107] J. H. Van Helden, N. Lang, U. Macherius, H. Zimmermann, and J. Röpcke. "Sensitive trace gas detection with cavity enhanced absorption spectroscopy using a continuous wave external-cavity quantum cascade laser". In: *Applied Physics Letters* 103.13 (2013), p. 131114.

[108] J. Wojtas, B. Rutecka, T. Stacewicz, J. Mikolajczyk, and Z. Bielecki. "N_2O detection with the CEAS method". In: *WIT Transactions on Modelling and Simulation* 51 (2011), pp. 461–472.

[109] M. R. McCurdy, Y. A. Bakhirkin, and F. K. Tittel. "Quantum cascade laser-based integrated cavity output spectroscopy of exhaled nitric oxide". In: *Applied Physics B: Lasers and Optics* 85.2-3 (2006), pp. 445–452.

[110] T. H. Risby and F. K. Tittel. "Current status of mid-infrared quantum and interband cascade lasers for clinical breath analysis". In: *Optical Engineering* 49.11 (2010), p. 111123.

[111] J. Wojtas. "Application of Cavity Enhanced Absorption Spectroscopy to the Detection of Nitric Oxide, Carbonyl Sulphide, and Ethane–Breath Biomarkers of Serious Diseases." In: *Sensors* 15.6 (2015), pp. 14356–69.

[112] Los Gatos Research, Inc. *Ultraportable Greenhouse Gas Analyzer*. URL: `http://www.lgrinc.com/analyzers/ultraportable-greenhouse-gas-analyzer/`.

[113] Picarro, Inc. *GasScouter.* URL: `http://www.picarro.com/products_solutions/trace_gas_analyzers/mobile_co2_ch4`.

[114] M. Clugston and R. Flemming. *Advanced Chemistry.* Oxford University Press, 2000.

[115] K. Rajagopal. *Textbook Of Engineering Physics, Part 1.* Prentice-Hall Of India Pvt. Ltd., 2008.

[116] N. Polfer and P. Dugourd. *Laser Photodissociation and Spectroscopy of Mass-separated Biomolecular Ions.* Springer International Publishing, 2013.

[117] P. Bernath. *Spectra of Atoms and Molecules.* Oxford University Press, 2015.

[118] L. Yadav. *Organic Spectroscopy.* Springer Netherlands, 2004.

[119] J. Hollas. *Modern Spectroscopy.* Wiley, 1987.

[120] F. Rouessac and A. Rouessac. *Chemical Analysis: Modern Instrumentation Methods and Techniques.* Wiley, 2013.

[121] S. Welzel, R. Engeln, and J. Röpcke. "Quantum Cascade Laser Based Chemical Sensing Using Optically Resonant Cavities". In: *Cavity-Enhanced Spectroscopy and Sensing.* Springer Berlin Heidelberg, 2014, pp. 93–142.

[122] A. O'Keefe. "Integrated cavity output analysis of ultra-weak absorption". In: *Chemical Physics Letters* 293 (1998), pp. 331–336.

[123] E. Schubert. *Light-Emitting Diodes.* Cambridge University Press, 2006.

[124] D. Romanini, I. Ventrillard, G. Méjean, J. Morville, and E. Kerstel. "Introduction to Cavity Enhanced Absorption Spectroscopy". In: *Cavity-Enhanced Spectroscopy and Sensing.* 2014, pp. 1–60.

[125] J. Morville, D. Romanini, and E. Kerstel. "Cavity Enhanced Absorption Spectroscopy with Feedback". In: *Cavity-Enhanced Spectroscopy and Sensing.* Springer Berlin Heidelberg, 2014, pp. 163–209.

[126] A. Yariv. *Quantum Electronics.* Wiley, 1975.

[127] W. Koechner. *Solid-State Laser Engineering.* Springer, 2013.

[128] A. O'Keefe, J. J. Scherer, and J. B. Paul. "cw Integrated cavity output spectroscopy". In: *Chemical Physics Letters* 307 (1999), pp. 343–349.

[129] M. Mazurenka, A. J. Orr-Ewing, R. Peverall, and G. A. D. Ritchie. "Cavity ring-down and cavity enhanced spectroscopy using diode lasers". In: *Annual Reports Section C: Physical Chemistry* 101 (2005), pp. 100–142.

[130] G. Berden and R. Engeln. *Cavity Ring-Down Spectroscopy: Techniques and Applications.* Wiley, 2009.

[131] S. Fiedler. "Incoherent broad-band cavity-enhanced absorption spectroscopy". In: *Chemical Physics Letters* 371.3-4 (2003), pp. 284–294.

[132] K. M. Manfred, L. Ciaffoni, and G. A. D. Ritchie. "Optical-feedback cavity-enhanced absorption spectroscopy in a linear cavity: model and experiments". In: *Applied Physics B: Lasers and Optics* 120.2 (2015), pp. 329–339.

[133] K. M. Manfred, G. A. D. Ritchie, N. Lang, J. Röpcke, and J. H. Van Helden. "Optical feedback cavity-enhanced absorption spectroscopy with a 3.24 μm interband cascade laser". In: *Applied Physics Letters* 106.22 (2015), pp. 1–5.

[134] P. Laurent, A. Clairon, and C. Breant. “Frequency Noise Analysis of Optically Self-Locked Diode Lasers”. In: *IEEE Journal of Quantum Electronics* 25.6 (1989), pp. 1131–1142.

[135] J. Morville, S. Kassi, M. Chenevier, and D. Romanini. “Fast, low-noise, mode-by-mode, cavity-enhanced absorption spectroscopy by diode-laser self-locking”. In: *Applied Physics B: Lasers and Optics* 80.8 (2005), pp. 1027–1038.

[136] D. J. Hamilton and A. J. Orr-Ewing. “A quantum cascade laser-based optical feedback cavity-enhanced absorption spectrometer for the simultaneous measurement of CH_4 and N_2O in air”. In: *Applied Physics B: Lasers and Optics* 102.4 (2011), pp. 879–890.

[137] I. Langmuir. “The Adsorption of Gases on Plane Surfaces of Glass, Mica and Platinum”. In: *Journal of the American Chemical Society* 40.9 (1918), pp. 1361–1403.

[138] SGE Analytical Science. *Agilent Technologies Liners.* URL: `http://www.sge.com/products/gc-lc-supplies/gc-supplies/gc-inlet-liners/agilent-technologies3`.

[139] Thermo Scientific. *Thermo Scientific™ Injection Port Liners for Agilent instruments.* URL: `https://www.fishersci.fi/shop/products/injection-port-liners-agilent-instruments/10100993`.

[140] R. Dandeneau and E. Zerenner. “An investigation of glasses for capillary chromatography”. In: *Journal of High Resolution Chromatography & Chromatography Communications* 2.6 (1979), pp. 351–356.

[141] T. A. Michalske and S. W. Freiman. “A molecular interpretation of stress corrosion in silica”. In: *Nature* 295 (1982), pp. 511–512.

[142] K. Robards, P. Haddad, and P. Jackson. “3 – Gas Chromatography”. In: *Principles and Practice of Modern Chromatographic Methods.* Academic Press, 2004, pp. 75–177.

[143] E. Prichard and B. Stuart. *Gas Chromatography.* Royal Society of Chemistry, 2003.

[144] W. Jennings. *Analytical Gas Chromatography.* Elsevier Science, 2012.

[145] Agilent Technologies. *Agilent J&W GC Column Selection Guide.* 2012. URL: `www.agilent.com/chem/myGCcolumns`.

[146] SGE. *Sol-Gel Technology for Gas Chromatographic Columns.* URL: `http://www.sge.com/uploads/5a/7f/5a7f0af3ea97c74ebe57bbc524f4346b/TA-0147-C.pdf`.

[147] Y. Guo and L. A. Colón. “A stationary phase for open tubular liquid chromatography and electrochromatography using Sol-Gel technology”. In: *Analytical Chemistry* 67.15 (1995), pp. 2511–2516.

[148] J. D. Hayes, A. Malik, C. Shende, A. Kabir, E. Townsend, D. Wang, S. L. Chong, L. Fang, S. Kulkarni, K. Alhooshani, S. Florida, and E. F. Avenue. “Sol–Gel Column Technology for Single-Step Deactivation, Coating, and Stationary-Phase Immobilization in High-Resolution Capillary Gas Chromatography”. In: *Analytical chemistry* 69 (1997), pp. 4566–4576.

[149] Agilent Technologies. *7200 Accurate-Mass Time-of-Flight GC/MS System Concepts Guide.* URL: `https://www.agilent.com/cs/library/usermanuals/Public/G3850-90003.pdf`.

[150] I. V. Chernushevich, A. V. Loboda, and B. A. Thomson. “An introduction to quadrupole-time-of-flight mass spectrometry”. In: *Journal of Mass Spectrometry* 36.8 (2001), pp. 849–865.

[151] J. T. Watson and O. D. Sparkman. *Introduction to Mass Spectrometry: Instrumentation, Applications, and Strategies for Data Interpretation.* Wiley, 2009, p. 819.

[152] Agilent Technologies. *Agilent 5977 Series MSD System - Concepts Guide.* URL: `https://www.agilent.com/cs/library/usermanuals/public/G3870-90104.pdf`.

[153] W. Henry. “Experiments on the Quantity of Gases Absorbed by Water, at Different Temperatures, and under Different Pressures”. In: *Philosophical Transactions of the Royal Society of London* 93.1 (1803), pp. 29–274.

[154] R. G. Mortimer. “7 – Multicomponent Systems”. In: *Physical Chemistry.* Second Edition. Burlington: Academic Press, 2000, pp. 199–254.

[155] I. Newton, D. Bernoulli, C. MacLaurin, and L. Euler. *Philosophiæ naturalis principia mathematica.* Georgius Brookman, T. T. and J. Tegg, R. Griffin, and Soc. Glasguæ, 1833.

[156] F. Jensen. *Introduction to Computational Chemistry.* Wiley, 2007, p. 624.

[157] E. Schrödinger. “Quantisierung als Eigenwertproblem”. In: *Annalen der Physik* 384.4 (1926), pp. 489–527.

[158] M. Born and J. R. Oppenheimer. “Zur Quantentheorie der Molekeln”. In: *Annalen der Physik* 84 (1927), pp. 457–484.

[159] C. J. Cramer. *Essentials of Computational Chemistry Theories and Models.* Wiley, 2004, pp. 334–342.

[160] J. Poater, M. Solà, M. Duran, and X. Fradera. “The calculation of electron localization and delocalization indices at the Hartree-Fock, density functional and post-Hartree-Fock levels of theory”. In: *Theoretical Chemistry Accounts* 107.6 (2002), pp. 362–371.

[161] J. A. Pople, M. Head-Gordon, D. J. Fox, K. Raghavachari, and L. A. Curtiss. “Gaussian-1 theory: A general procedure for prediction of molecular energies”. In: *The Journal of Chemical Physics* 90.10 (1989), p. 5622.

[162] J. A. Pople, A. P. Scott, M. W. Wong, and L. Radom. “Scaling Factors for Obtaining Fundamental Vibrational Frequencies and Zero-Point Energies from HF/6–31G* and MP2/6–31G* Harmonic Frequencies”. In: *Israel Journal of Chemistry* 33 (1993), pp. 345–350.

[163] M. Schwartz, P. Marshall, R. J. Berry, C. J. Ehlers, and G. A. Petersson. “Computational Study of the Kinetics of Hydrogen Abstraction from Fluoromethanes by the Hydroxyl Radical”. In: *The Journal of Physical Chemistry A* 102.49 (1998), pp. 10074–10081.

[164] M. D. Halls, J. Velkovski, and H. B. Schlegel. "Harmonic frequency scaling factors for Hartree-Fock, S-VWN, B-LYP, B3-LYP, B3-PW91 and MP2 with the Sadlej pVTZ electric property basis set". In: *Theoretical Chemistry Accounts* 105.6 (2001), pp. 413–421.

[165] N. Goldberg, M. J. Almond, J. Steven Ogden, J. Pat Cannady, R. Walsh, and R. Becerra. "The gas-phase reactions of $SiCl_4$ and Si_2Cl_6 with CH_3OH and C_2H_5OH: An investigation by mass spectrometry and matrix-isolation infrared spectroscopy". In: *Physical Chemistry Chemical Physics* 6.13 (2004), pp. 3264–3270.

[166] V. N. Maiorov and G. M. Crippen. "Significance of Root-Mean-Square Deviation in Comparing Three-dimensional Structures of Globular Proteins". In: *Journal of Molecular Biology* 235.2 (1994), pp. 625–634.

[167] M. J. Frisch, G. W. Trucks, H. B. Schlegel, G. E. Scuseria, M. A. Robb, J. R. Cheeseman, G. Scalmani, V. Barone, G. A. Petersson, H. Nakatsuji, X. Li, M. Caricato, A. Marenich, J. Bloino, B. G. Janesko, R. Gomperts, B. Mennucci, H. P. Hratchian, J. V. Ortiz, A. F. Izmaylov, J. L. Sonnenberg, D. Williams-Young, F. Ding, F. Lipparini, F. Egidi, J. Goings, B. Peng, A. Petrone, T. Henderson, D. Ranasinghe, V. G. Zakrzewski, J. Gao, N. Rega, G. Zheng, W. Liang, M. Hada, M. Ehara, K. Toyota, R. Fukuda, J. Hasegawa, M. Ishida, T. Nakajima, Y. Honda, O. Kitao, H. Nakai, T. Vreven, K. Throssell, J. A. Montgomery, Jr., J. E. Peralta, F. Ogliaro, M. Bearpark, J. J. Heyd, E. Brothers, K. N. Kudin, V. N. Staroverov, T. Keith, R. Kobayashi, J. Normand, K. Raghavachari, A. Rendell, J. C. Burant, S. S. Iyengar, J. Tomasi, M. Cossi, J. M. Millam, M. Klene, C. Adamo, R. Cammi, J. W. Ochterski, R. L. Martin, K. Morokuma, O. Farkas, J. B. Foresman, and D. J. Fox, Gaussian, Inc., Wallingford CT, 2016. *Gaussian 09*. Version A.02. 2009.

[168] C. M. Western, University of Bristol. *PGOPHER*. Version 8.0. 2014.

[169] J. Howell, M. Menguc, and R. Siegel. *Thermal Radiation Heat Transfer*. CRC Press, 2015.

[170] D. Rousseau. *Optical Techniques in Biological Research*. Elsevier Science, 2012.

[171] PerkinElmer Inc. *Chem3D*. Version 15.1.0.144.

[172] National Center for Biotechnology Information. *PubChem Compound Database, CID=637566*. URL: `https://pubchem.ncbi.nlm.nih.gov/compound/637566`.

[173] Pacific Northwest National Laboratory. *Vapor phase infrared spectral library*. URL: `http://nwir.pnl.gov`.

[174] Harvard-Smithsonian Center for Astrophysics (CFA), V.E. Zuev Insitute of Atmosperic Optics (IAO), and National Research Tomsk State University (TSU). *HITRAN on the Web*. URL: `http://hitran.iao.ru/`.

[175] OriginLab, Northampton, MA, USA. *OriginPro 2015*. Version b9.2.272. 2015.

[176] OriginLab. *2.12.6 pkFind*. URL: `http://www.originlab.com/doc/X-Function/ref/pkFind#Local_Maximum_Method`.

[177] The Herb Society of America. *Roses: 2012 Herb of the Year*. 2011.

[178] M. Lis-Balchin. *Geranium and Pelargonium: History of Nomenclature, Usage and Cultivation*. CRC Press, 2003.

[179] S. Stein, Y. Mirokhin, D. Tcheckovskoi, and G. Mallard, National Institute of Standards and Technology. *The NIST Mass Spectral Search Program for the NIST/EPA/NIH Mass Spectral Library.* Version 2.0f. 2011.

[180] M. H. Boskabady, M. N. Shafei, Z. Saberi, and S. Amini. "Pharmacological effects of *Rosa damascena*". In: *Iranian Journal of Basic Medical Sciences* 14.4 (2011), pp. 295–307.

[181] M. Mahboubi. "*Rosa damascena* as holy ancient herb with novel applications". In: *Journal of Traditional and Complementary Medicine* 6.1 (2016), pp. 10–16.

[182] A. Dobreva. "Dynamics of the Headspace Chemical Components of *Rosa damascena* Mill. Flowers". In: *Journal of Essential Oil Bearing Plants* 16.3 (2013), pp. 404–411.

[183] A. Spietelun, M. M. Pilarczyk, A. Kloskowski, J. Namiesnik, J. Namieśnik, and J. Namiesnik. "Current trends in solid-phase microextraction (SPME) fibre coatings". In: *Chemical Society Reviews* 39.11 (2010), pp. 4524–4537.

[184] A. Ben Hsouna and N. Hamdi. "Phytochemical composition and antimicrobial activities of the essential oils and organic extracts from Pelargonium graveolens growing in Tunisia." In: *Lipids in health and disease* 11.1 (2012), p. 167.

[185] Z. N. Juárez, H. Bach, E. Sánchez-Arreola, H. Bach, and L. R. Hernández. "Protective antifungal activity of essential oils extracted from *Buddleja perfoliata* and *Pelargonium graveolens* against fungi isolated from stored grains". In: *Journal of Applied Microbiology* 1927 (2016).

[186] S. Bouchonnet. *Introduction to GC-MS Coupling.* Taylor & Francis, 2013.

[187] Agilent Technologies. *Enhanced ChemStation.* Version E.02.00.493. 2008.

[188] OriginLab. *15.5.7.5 Fitting with Errors and Weighting.* URL: `http://www.originlab.com/doc/Origin-Help/FIt-with-Err-Weight`.

[189] J. Brandle and P. Telmer. "Steviol glycoside biosynthesis". In: *Phytochemistry* 68.14 (2007), pp. 1855–1863.

[190] V. M. Dembitsky. "Astonishing diversity of natural surfactants: 7. Biologically active hemi- and monoterpenoid glycosides". In: *Lipids* 41.1 (2006), pp. 1–27.

[191] F. Rivas, A. Parra, A. Martinez, and A. Garcia-Granados. "Enzymatic glycosylation of terpenoids". In: *Phytochemistry Reviews* 12.2 (2013), pp. 327–339.

[192] A. Mannschreck and E. Von Angerer. "The scent of roses and beyond: Molecular structures, analysis, and practical applications of odorants". In: *Journal of Chemical Education* 88.11 (2011), pp. 1501–1506.

[193] R. Al-Yahyai, A. Al-Subhi, J. Al-Sabahi, and F. Al-Said. "Chemical composition of acid lime leaves infected with *Candidatus* Phytoplasma aurantifolia". In: 5.1 (2014), pp. 66–70.

[194] H. Baydar, H. Schulz, H. Krüger, S. Erbas, and S. Kineci. "Influences of Fermentation Time, Hydro-distillation Time and Fractions on Essential Oil Composition of Damask Rose (*Rosa damascena* Mill.)" In: *Journal of Essential Oil Bearing Plants* 11.3 (2008), pp. 224–232.

[195] K. J. Naquvl, S. H. Ansarl, M. Ali, and A. K. Najml. “Volatile Oil Composition of *Rosa Damascena* Mill (Rosaceae)”. In: *Journal of Pharmacognosy and Phytochemistry* 2.5 (2014), pp. 177–181.

[196] H. Panda. *Cultivation and Utilization of Aromatic Plants.* NIIR Project Consultancy Services, 2005.

[197] E. A. Baker. “Chemistry and morphology of plant epicuticular waxes”. In: *The Cuticle.* 1982, pp. 139–163.

[198] A. V. N. Paul, S. Singh, and A. K. Singh. “Kairomonal effect of some saturated hydrocarbons on the egg parasitoids, *Trichogramma brasiliensis* (Ashmead) and *Trichogramma exiguum*, Pinto, Platner and Oatman (Hym., Trichogrammatidae)”. In: *Journal of Applied Entomology* 126.7-8 (2002), pp. 409–416.

[199] N. Jain, K. K. Aggarwal, K. V. Syamasundar, S. K. Srivastava, and S. Kumar. “Essential oil composition of geranium (*Pelargonium* sp.) from the plains of Northern India”. In: *Flavour and Fragrance Journal* 16.1 (2001), pp. 44–46.

[200] T. DeBaggio and A. Tucker. *The Encyclopedia of Herbs: A Comprehensive Reference to Herbs of Flavor and Fragrance.* Timber Press, 2009.

[201] R. H. Smith. “Xylem monoterpenes of pines: distribution, variation, genetics, function”. In: *General Technical Report, Pacific Southwest Research Station, Forest Service, U.S. Department of Agriculture* (2000).

[202] M. A. Ibrahim, M. Mäenpää, V. Hassinen, S. Kontunen-Soppela, L. Malec, M. Rousi, L. Pietikäinen, A. Tervahauta, S. Kärenlampi, J. K. Holopainen, and E. J. Oksanen. “Elevation of night-time temperature increases terpenoid emissions from *Betula pendula* and *Populus tremula*”. In: *Journal of Experimental Botany* 61.6 (2010), pp. 1583–1595.

[203] S. Rasmann, T. G. Köllner, J. Degenhardt, I. Hiltpold, S. Toepfer, U. Kuhlmann, J. Gershenzon, and T. C. Turlings. “Recruitment of entomopathogenic nematodes by insect-damaged maize roots”. In: *Nature* 434.7034 (2005), pp. 732–737.

[204] H. Bichão, A. K. Borg-Karlson, J. Araújo, and H. Mustaparta. “Five types of olfactory receptor neurons in the strawberry blossom Weevil *Anthonomus rubi* selective responses to inducible host-plant volatiles”. In: *Chemical Senses* 30.2 (2005), pp. 153–170.

[205] R. Péter, I. Katali, R. Péter, S. Szilvia, and Z. N. Éva. In: *Effect of two irrigation regimes on the production and secondary metabolites of sweet basil (Ocimum basilicum L. ’Genovese’).* Proceedings of the Seventh Conference on Medicinal and Aromatic Plants of Southeast European Countries. (May 27–31, 2012). Subotica, Republic of Serbia: Institute for Medicinal Plant Research “Dr Josif Pancic”, Belgrade, Association for Medicinal, and Aromatic Plants of Southeast European Countries, 2012, pp. 267–272.

[206] A. Prasad, A. Chattopadhyay, S. Chand, A. A. Naqvi, and A. Yadav. “Effect of Soil Sodicity on Growth, Yield, Essential Oil Composition, and Cation Accumulation in Rose-Scented Geranium”. In: *Communications in Soil Science and Plant Analysis* 37 (2006), pp. 1805–1817.

[207] H. N. Matsuura, F. de Costa, A. C. A. Yendo, and A. G. Fett-Neto. “Photoelicitation of Bioactive Secondary Metabolites by Ultraviolet Radiation: Mechanisms, Strategies, and Applications”. In: *Biotechnology for Medicinal Plants: Micropropagation and Improvement.* Springer Berlin Heidelberg, 2013, pp. 171–190.

[208] D. Steinmüller and M. Tevini. “Action of ultraviolet radiation (UV-B) upon cuticular waxes in some crop plants”. In: *Planta* 164.4 (1985), pp. 557–564.

[209] E. E. Aziz, H. Al-Amier, and L. E. Craker. “Influence of salt stress on growth and essential oil production in peppermint, pennyroyal, and apple mint”. In: *Journal of Herbs, Spices and Medicinal Plants* 14.1-2 (2008), pp. 77–87.

[210] S. Echeverrigaray, J. Zacaria, and R. Beltrão. “Nematicidal activity of monoterpenoids against the root-knot nematode *Meloidogyne incognita*”. In: *Phytopathology* 100.2 (2010), pp. 199–203.

[211] K. L. Ringer. “Monoterpene Metabolism. Cloning, Expression, and Characterization of (-)-Isopiperitenol/(-)-Carveol Dehydrogenase of Peppermint and Spearmint”. In: *Plant Physiology* 137.3 (2005), pp. 863–872.

[212] S. Delfine, F. Loreto, P. Pinelli, R. Tognetti, and A. Alvino. “Isoprenoids content and photosynthetic limitations in rosemary and spearmint plants under water stress”. In: *Agriculture, Ecosystems and Environment* 106.2-3 (2005), pp. 243–252.

[213] R. Koppmann. *Volatile Organic Compounds in the Atmosphere.* Wiley, 2008.

[214] Ü. Niinemets and M. Reichstein. “Controls on the emission of plant volatiles through stomata: Differential sensitivity of emission rates to stomatal closure explained”. In: *Journal of Geophysical Research: Atmospheres* 108.D7 (2003), p. 4208.

[215] T. Yuan, Q. Chen, P. Zhao, Y. Zeng, X. Liu, and S. Lu. “Identification of enzymes responsible for the reduction of geraniol to citronellol”. In: *Natural Products and Bioprospecting* 1.3 (2011), pp. 108–111.

[216] Y. Iijima, D. R. Gang, E. Fridman, E. Lewinsohn, and E. Pichersky. “Characterization of geraniol synthase from the peltate glands of sweet basil.” In: *Plant Physiology* 134.1 (2004), pp. 370–379.

[217] Analytical Methods Committee. “Application of gas-liquid chromatography to the analysis of essential oils. Part III. The determination of geraniol in oils of citronella”. In: *Analyst* 98.1172 (1973), pp. 823–829.

[218] D. S. Pedersen, D. L. Capone, G. K. Skouroumounis, A. P. Pollnitz, and M. A. Sefton. “Quantitative analysis of geraniol, nerol, linalool, and α-terpineol in wine”. In: *Analytical and Bioanalytical Chemistry* 375.4 (2003), pp. 517–522.